TEMPORARY SATELLITE CAPTURE OF SHORT-PERIOD JUPITER FAMILY COMETS FROM THE PERSPECTIVE OF DYNAMICAL SYSTEMS

A Thesis

Submitted to the Faculty

of

Purdue University

by

Belinda Marchand

In Partial Fulfillment of the

Requirements for the Degree

of

Master of Science in Aeronautics and Astronautics

December 2000

Para mami.

ACKNOWLEDGMENTS

"When you come to the edge of all the light you know, and are about to step off into the darkness of the unknown, faith is knowing one of two things will happen: There will be something solid to stand on, or you will be taught how to fly." *Barbara J. Winter*

First and foremost, I thank God for giving me the strength to finish my degree in spite of the adversity of the last few years. I must also thank my mother. Her love allowed me to soar to great heights both in dreams and in life. Her strength, courage, and determination will always be a source of inspiration. I'd also like to thank my sister, Brenda Marchand, for helping me get my dreams off the ground and for being there every step of the way. Aside from my family, I'd like to thank Professor Howell. Through my daily interaction with her as a student, a teaching assistant, and a researcher, I've learned a lot about patience and about teaching. In particular, that good teaching is more about asking the right questions than giving the right answers. A lesson that I also value as a researcher. I hold the utmost respect and admiration for her both as a professional and a human being. Furthermore, I'd like to thank Brian Barden, whose words of encouragement and advice over the last few years inspired me to further my graduate education. I also extend my gratitude and love to my good friends, Linda Flack, Anne Gick, Eric Campbell, Jose Guzman, Greg Roth, Sergio Hasebe, and Mike Burke for being there through thick and thin.

Finally, I wish to thank those institutions that have provided funding for my graduate studies. Over the last three years I have been partially funded by the Purdue University Department of Aeronautics and Astronautics, the Indiana Space Grant Consortium, as well as the National Aeronautics and Space Administration through the Jet Propulsion Laboratory, California Institute of Technology, under contract No. 1211514.

TABLE OF CONTENTS

Page

LIST OF FIGURES

Figure Page

Figure Page

ABSTRACT

Marchand, Belinda, M.S.A.A., Purdue University, December, 2000. Temporary Satellite Capture of Short-Period Jupiter Family Comets from the Perspective of Dynamical Systems. Major Professor: Kathleen C. Howell.

The Temporary Satellite Capture (TSC) of short-period comets, such as Oterma and Helin-Roman-Crockett, by Jupiter has intrigued astronomers for many years. A widely accepted approach to study TSC is to numerically integrate the equations of motion for the n-body problem using a wide range of initial conditions obtained from the heliocentric two-body problem; then, a search ensues for instances when the Joviocentric energy becomes negative. More recently, a preliminary analysis involving the application of dynamical systems theory to the Sun-Jupiter-comet three-body problem has provided significant insight into the motion in the Sun-Jupiter system and offered a simple model to account for the TSC phenomena observed in Jupiter family short-period comets. The accuracy of this model can be immediately verified since ephemeris data is available for comet trajectories.

In this work, the TSC path of two Jupiter family comets, Oterma and Helin-Roman-Crockett, is compared to trajectory arcs along the stable and unstable manifolds associated with three-dimensional periodic and quasi-periodic orbits near the libration points L_1 and L_2 in the Sun-Jupiter system. The initial analysis is based on the circular restricted three-body model of the Sun-Jupiter-comet system. In particular, the stable and unstable manifolds associated with three-dimensional families of periodic halo orbits are considered. The inherent symmetry properties associated with the circular restricted three-body problem, combined with numerical studies on the evolution of the stable and unstable manifolds, simplify the process of identifying trajectory arcs, in configuration space, that resemble the path of a particular comet during capture. The goal of this investigation is to identify a "match" to

the *six*-dimensional state of the comet during capture. Once the position elements are successfully matched in the circular restricted model, it is necessary to establish whether the corresponding velocity elements also match those of the comet. Analysis of the available empirical data reveals that, in the circular restricted three-body problem, the discrepancy in the velocity elements can be significant. Thus, to improve the accuracy of the *six*-dimensional match, the solution is transferred into the ephemeris model. In this model, the equations of motion are numerically integrated using actual ephemeris information for the planets. The concepts from dynamical systems theory that are employed in the circular restricted three-body problem are successfully extended to the ephemeris model. In the ephemeris model, periodic solutions in the vicinity of the libration points do not exist. Thus, quasi-periodic Lissajous trajectories near L_1 and L_2 are considered. Although the symmetry properties are lost mathematically in the ephemeris model, in practice the general features of the solution are well preserved. For the comets considered in this study, this loss of symmetry introduces changes in both the position and velocity states. These changes actually improve significantly the match relative to the solution that was initially identified in the circular restricted three-body problem. This methodology is successfully applied to two short-period Jupiter family comets: Oterma and Helin-Roman-Crockett.

1. Introduction

In July 1943, L.E. Cunningham and R.N. Thomas [1] published data that revealed, among other things, that the recently discovered comet 39P/Oterma had passed close to Jupiter in 1938. Astronomers subsequently noted that the orbit of the comet was "not particularly stable" due to multiple close approaches of Jupiter. It is a generally accepted practice in astronomy to explain the erratic behavior of short-period comets such as Oterma in the context of a heliocentric *two*-body problem where perturbations from the outer planets result in significant changes to the orbital parameters corresponding to a given comet. However, evaluating this issue from the perspective of dynamical systems theory has offered new insight into the erratic dynamical behavior of this and other comets.

1.1 Previous Work

Comets like 39P/Oterma (OTR) and 111P/Helin-Roman-Crockett (HRC) are classified as Jupiter family short-period comets. These comets share at least one significant orbital characteristic: at some time during their dynamical evolution, each experiences a low-velocity close encounter with Jupiter such that the Joviocentric energy becomes negative. This event is denoted as Temporary Satellite Capture (TSC). Kazimirchak-Polonskaya [2] studied TSC in the early 1970's by numerically integrating the orbits of a group of minor bodies, with a wide range of heliocentric orbital elements as initial conditions. She used an n-body integrator to propagate the initial conditions and searched for instances when the bodies crossed the sphere of influence of Jupiter, Saturn, Uranus, or Neptune. This effort was an attempt to create the dynamical circumstances required for a TSC to occur and thus establish a criterion for capture. Carusi [3, 4, 5, 6, 7, 8, 9, 10] in collaboration with Pozzi [3], Valsecchi

[4, 5, 6, 7, 8, 9, 10], Kresák [7, 9], and Perozzi [8] employed a similar approach to study the capture phenomena.

Investigations of this problem have subsequently continued. In the mid-1970's, Horedt [11], Heppenheimer [12, 13], and Porco [13] considered the problem of TSC in the context of the *planar* circular restricted three-body problem (CR3BP). These authors attributed the strange behavior of some Jupiter family comets to the separatrices associated with the libration point L_1 in the Sun-Jupiter system. Though not explicitly stated, this may be the first study linking the behavior of short-period Jupiter family comets to the dynamical structure associated with the collinear libration points in the Sun-Jupiter system. This basic concept represents the framework of several studies in subsequent years. In the late 1980's, Murison [14]-[15] compared the more general aspects of TSC to the fractal nature of the dynamics in the planar CR3BP. In a more recent effort, a similar idea is implemented by Lo and Ross [16] in modeling the capture motion of some Jupiter family short-period comets, such as Oterma, Gehrels 3, and Helin-Roman-Crockett. In particular, the in-plane motion of these comets is compared to the stable and unstable manifolds associated with the collinear libration points L_1 and L_2 in the Sun-Jupiter three-body system. For OTR and HRC, this approach successfully reveals many of the significant features of the comet's motion. Consistent with previous work, Lo and Ross focus on the planar motion, that is, the comet motion is approximated as planar and compared to in-plane manifolds associated with the libration points L_1 and L_2. It is also noted, however, that certain comet behavior is even more completely reflected in the evolution of stable and unstable manifolds corresponding to *three*-dimensional periodic orbits in the vicinity of L_1 and L_2, rather than just the manifolds associated specifically with the libration points. Koon, Lo, Marsden, and Ross [17] consider this issue in the context of the *planar* restricted three-body problem and present some theoretical results as well. But, to allow for a more thorough investigation of the critical features in the context of periodic orbits and quasi-periodic trajectories in the *three*-dimensional three-body problem (3BP), the complexities involved with the out-of-plane compo-

nent of the motion are required; such analysis is the focus of the current effort (K.C. Howell, B.G. Marchand, and M.W. Lo [18]).

1.2 Scope of Present Work

In this investigation, the motion of OTR and HRC are considered within the framework of the *three*-dimensional, restricted *three*-body problem. This formulation allows for consideration of the impact of the stable and unstable manifolds, associated with both three-dimensional halo orbits and Lissajous trajectories, on the evolution of the comet trajectories. In particular, the problem is posed as a search for trajectory arcs along the stable and/or unstable manifolds that reflect the comet orbit. Initially, the comet trajectories are viewed in the context of the circular (but three-dimensional) restricted problem. The inherent symmetries in this model simplify the task of locating a trajectory arc that closely matches a segment along the path of OTR and HRC, particularly during TSC. Such a trajectory arc is defined as a "match." Once a match is identified, the solution is transferred to the ephemeris model. In this model, actual ephemeris data for the motion of the primary bodies is used during the numerical integration of the relative equations of motion. The purpose of this last step is to improve the accuracy of the match. Of course, the final arc that is computed is evaluated against the actual comet path that is also available from ephemeris information.

This study is organized as follows:

- Chapter 2: In this chapter the equations of motion for the circular restricted *three*-body problem are developed. To gain insight into the geometry of the solution space, the natural symmetry of solutions inherent to the mathematical model is observed. Furthermore, the regions of space where the comet can dynamically evolve, in a CR3BP model, are defined via the *three*-dimensional regions of exclusion corresponding to a particular energy level. Once the expected symmetry of solutions and the dynamical regions of exclusion are defined, it is necessary to examine the stability characteristics of particular solutions in this model. Variational equations and stability analyses of both continuous

and discrete time systems are considered. The stability of continuous time systems is discussed introduce some basic concepts from invariant manifold theory. Then, to facilitate the study of periodic orbits and their stability, the discretized approach is discussed to support the application of the basic concepts and theorems of invariant manifold theory to discrete time systems.

- Chapter 3: Further insight into the geometry of solutions is developed through numerical analysis. This chapter presents the results of extensive numerical investigations that reveal similarities among the stable and unstable manifolds, across families of periodic halo orbits. First, the necessary notation for this numerical parametric study is introduced. Then, the evolution of the stable and unstable eigenvector directions along a family of halo orbits is discussed. Each state ("point of origin") along an unstable orbit can be used to compute a *six*-dimensional stable and unstable eigenvector. Observations about the features of particular trajectory arcs in the vicinity of Jupiter are presented both as a function of these eigenvector directions and as a function of the relative location of the "point of origin" along the periodic orbit. To successfully exploit both the analytical symmetries and the numerical near-symmetries corresponding to this solution space, the definition of temporary satellite capture is modified. The TSC mechanism is very complex and each capture exhibits its own unique characteristics. The capture path of Oterma is very different than that of Helin-Roman-Crockett. Hence, ephemeris information for these comets is used to categorize the possible types of capture. A focused search of the solution space is then initiated for a trajectory arc that matches the comet's path. Once a match is identified in the CR3BP, the solution is transferred to a less restrictive ephemeris model to improve the accuracy of the match. The methodology detailed in this chapter is applied to identify particular solutions that resemble the capture paths of Oterma and Helin-Roman-Crockett.

- Chapter 4: Concluding remarks and suggestions for future work and applications.

2. Background

2.1 Circular Restricted Three-Body Problem

Cometary motion is typically considered in the context of an n-body model, specifically, one that incorporates all planetary perturbations. However, for some comets the most significant gravitational influences originate from the Sun and Jupiter. Thus, the motion of these comets is most accurately approximated within the context of the three-body problem (3BP) as defined by the Sun-Jupiter-comet system. In this investigation, the path of a comet in a 3BP is compared to actual cometary ephemeris information. The goal is the identification and isolation of a particular trajectory, propagated in the three-body model, that closely resembles the "true" path of the comet (as defined by the ephemerides), particularly during instances when the comet is temporarily captured by Jupiter. The success of this process is based on an understanding of the geometry of the solution space that is available. The general 3BP possesses a phase space of dimension 18. Thus, 18 integrals are required to obtain a closed form solution to the equations of motion. To date, only ten integrals are known in the general n-body problem. Thus, an exact analytical solution does not currently exist for $n \geq 3$. However, given the general 3BP, some additional assumptions offer a simplified model that can be exploited for a better understanding of the types of motion to be expected in the Sun-Jupiter-comet system.

In the simplified Sun-Jupiter-comet system, it is assumed that the mass of the comet is both constant and negligible, relative to the masses of the Sun and Jupiter. The two larger bodies, in this case the Sun and Jupiter, are defined as the primaries. The primaries are assumed to be spherically symmetric and, hence, are modeled as point masses. For notational purposes, the larger primary is defined as P_1, the smaller

primary as P_2, and the comet as P_3, where $M_3 << M_2 < M_1$. The term "restricted" denotes the assumption of infinitesimal mass for M_3. It is also assumed that the motion of the primaries about their common barycenter (center of mass) is circular. Geometrically, this model suggests some analytical and numerical symmetries. Knowledge of these symmetries is a key component in identifying particular trajectory arcs that exhibit characteristics similar to those of a captured comet. Thus, this section is devoted to developing the equations of motion for the circular restricted three-body problem (CR3BP), and analyzing the types of motion that can be expected, based on the symmetry properties inherent to this model.

2.1.1 Definitions of Appropriate Coordinate Frames

The development of any mathematical model usually requires the specification of generalized coordinates. For example, the spatial location of each particle can be described in terms of a set of cartesian coordinates relative to an inertially fixed reference frame (I), defined by a dextral set of orthogonal unit vectors $\hat{X}$-$\hat{Y}$-$\hat{Z}$. (Note that carets indicate vectors of unit magnitude.) In the CR3BP, the inertial XY-plane is defined as the plane of motion of the primaries. The inertial Z-axis coincides with the direction of orbital angular momentum. The origin of the inertial coordinate frame is defined as the barycenter of the three-body system, B.

An alternative representation corresponds to a set of spatial coordinates measured relative to the synodic rotating frame (R), defined by the dextral orthonormal triad $\hat{x}$-$\hat{y}$-$\hat{z}$. In the synodic frame, the x-axis is directed from P_1 to P_2, the z-axis is aligned with the direction of orbital angular momentum corresponding to the primary motion, and the y-axis completes the right handed triad. The relative orientation of the synodic frame with respect to the inertial frame is measured by the angle θ. These two coordinate frames are illustrated in Figure 2.1.

2.1.2 Characteristic Quantities

To preserve the generality of the mathematical model, it is useful to introduce some parameters that are characteristic of a particular three-body system. This set of parameters is used to nondimensionalize the equations of motion (EOMS). To com-

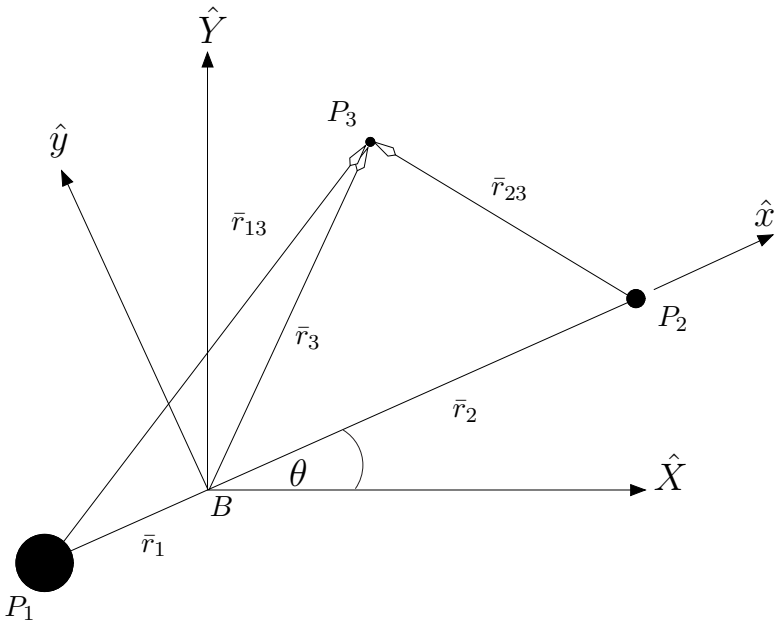

Figure 2.1. Coordinate Frame Definitions

pletely nondimensionalize the EOMS, it is necessary to define the three fundamental dimensions (mass, length, and time) in terms of the system parameters. The reference length is defined as the distance between the primaries, L_{ref}. The combined mass of the primaries $M_{ref} = M_1 + M_2$ is then denoted as the reference mass. Then, the characteristic time, t_{ref}, is defined as $1/n$ where

$$n = \sqrt{\frac{GM_{ref}}{{L_{ref}}^3}}, \tag{2.1}$$

is the mean motion of the primaries.

In nondimensional units, the mass of P_2 is evaluated as M_2/M_{ref}, and is defined as the system mass parameter μ. Consequently, the mass of P_1 is expressed as $1-\mu$. Since the characteristic length is the constant distance between the primaries, the nondimensional distance between P_1 and P_2 is always equal to one. Hence, from the definition of the center of mass, the position vector locating P_1 relative to the barycenter can be expressed in the form $\bar{r}_1 = -\mu\hat{x}$ in nondimensional units, where overbars denote vector quantities. Similarly, the position vector locating P_2 with respect to the barycenter can be represented in the nondimensional form $\bar{r}_2 = (1-\mu)\hat{x}$.

2.1.3 Equations of Motion

The derivation of the EOMS is based on a Newtonian approach. Let the nondimensional position of P_3, as observed in the rotating frame, be written as

$$\bar{r}_3 = x\hat{x} + y\hat{y} + z\hat{z} \ . \tag{2.2}$$

The angular velocity of the synodic rotating frame (R) relative to the inertial frame (I) is expressed in vector form as ${}^I\bar{\omega}^R = \dot{\theta}\hat{z}$. Since the motion of the primaries is assumed to remain planar and circular, $\dot{\theta}$ is constant and equal to one in nondimensional units. Thus, the vector kinematical expression for the inertial velocity of P_3 is evaluated as follows,

$$\begin{aligned} {}^I\dot{\bar{r}}_3 &= {}^R\dot{\bar{r}}_3 + {}^I\bar{\omega}^R \times \bar{r}_3 \ , \\ &= (\dot{x} - \dot{\theta}x)\hat{x} + (\dot{y} + \dot{\theta}x)\hat{y} + \dot{z}\hat{z} \ , \end{aligned} \tag{2.3}$$

where dots indicate derivatives with respect to nondimensional time. Subsequently, from kinematics, the inertial acceleration of P_3 is expressed as

$$\begin{aligned} {}^I\ddot{\bar{r}}_3 &= {}^R\ddot{\bar{r}}_3 + {}^I\bar{\omega}^R \times {}^R\dot{\bar{r}}_3 \ , \\ &= (\ddot{x} - 2\dot{\theta}\dot{y} - \dot{\theta}^2 x)\hat{x} + (\ddot{y} + 2\dot{\theta}\dot{x} - \dot{\theta}^2 y)\hat{y} + \ddot{z}\hat{z} \ . \end{aligned} \tag{2.4}$$

The two significant gravitational fields in this model are represented by two forces applied to P_3. Consistent with the inverse-square gravitational force model, the resultant force acting on P_3 can be expressed, nondimensionally, in the form

$$\bar{F} = -\frac{(1-\mu)}{r_{13}^3}\bar{r}_{13} - \frac{\mu}{r_{23}^3}\bar{r}_{23} \ . \tag{2.5}$$

Substitution of equations (2.4) and (2.5) into Newton's Law of Motion results in three scalar equations of motion,

$$\ddot{x} - 2\dot{\theta}\dot{y} = \dot{\theta}^2 x - \frac{(1-\mu)(x+\mu)}{r_{13}^3} - \frac{\mu(x-1+\mu)}{r_{23}^3} \ , \tag{2.6}$$

$$\ddot{y} + 2\dot{\theta}\dot{x} = \dot{\theta}^2 y - \Big\{\frac{1-\mu}{r_{13}^3} + \frac{\mu}{r_{23}^3}\Big\}y \ , \tag{2.7}$$

$$\ddot{z} = -\Big\{\frac{1-\mu}{r_{13}^3} + \frac{\mu}{r_{23}^3}\Big\}z \ . \tag{2.8}$$

The right side of equations (2.6)-(2.8) can be rewritten in terms of the following pseudo-potential function (U),

$$U = \frac{1}{2}\dot{\theta}^2(x^2 + y^2) + \frac{1-\mu}{r_{13}} + \frac{\mu}{r_{23}} \ . \tag{2.9}$$

Since the nondimensional value of $\dot{\theta}$ is one, the equations of motion are reduced to the following form,

$$\ddot{x} = \frac{\partial U}{\partial x} + 2\dot{y} \ , \tag{2.10}$$

$$\ddot{y} = \frac{\partial U}{\partial y} - 2\dot{x} \ , \tag{2.11}$$

$$\ddot{z} = \frac{\partial U}{\partial z} \ . \tag{2.12}$$

Although the EOMs can be expressed in terms of a pseudo-potential function (U), total mechanical energy is not actually conserved in the R3BP due to the infinitesimal mass assumption for P_3. In fact, Poincaré [19] proved that, unlike the general three-body problem where 10 integrals exist (six for the center of mass, three for angular momentum, and one for total mechanical energy), no integrals of the motion exist in the restricted three-body problem apart from the Jacobian or Jacobi constant (C). The algebraic expression for the Jacobian is derived from equations (2.10)-(2.12), and appears in the following form,

$$C = 2U - (\dot{x}^2 + \dot{y}^2 + \dot{z}^2) \ . \tag{2.13}$$

The Jacobi constant is a source of significant insight into the types of motion that can exist in the CR3BP. By evaluating equation (2.13) under conditions of zero relative velocity it is possible to identify contours of C that bound the regions of configuration space within which the third particle (comet) dynamically evolves. The significance of these zero-velocity contours in the TSC problem will later be apparent.

2.1.4 State Transition Matrix

Since no closed-form analytical solution exists for equations (2.10)-(2.12), the identification of a time history for motion in the CR3BP is ultimately based on numerical

analysis. One of the techniques used here is a differential corrections process. This approach relies on knowledge of both the Jacobian matrix and the state transition matrix (STM). Let the six-dimensional vector $\bar{x}_{ref} = [x(t)\ y(t)\ z(t)\ \dot{x}(t)\ \dot{y}(t)\ \dot{z}(t)]^T$ represent the vector time history corresponding to a known solution to the nonlinear EOMS, equations (2.10)-(2.12). (Superscript T denotes transpose.) The vector variation $\bar{y}(t) = [\delta x(t)\ \delta y(t)\ \delta z(t)\ \delta\dot{x}(t)\ \delta\dot{y}(t)\ \delta\dot{z}(t)]^T$, relative to $\bar{x}_{ref}$, can be approximated via a Taylor series expansion about $\bar{x}_{ref}$. A first order approximation results in variational equations of the form

$$\dot{\bar{y}}(t) = A(t)\bar{y}(t)\ , \tag{2.14}$$

where $A(t)$ is the 6×6 Jacobian matrix, with time-varying elements that appear in the following form,

$$A(t) = \begin{bmatrix} I_3 & 0_3 \\ U_{ij} & 2\Omega_3 \end{bmatrix}\ . \tag{2.15}$$

The submatrices I_k and 0_k, correspond to the $k \times k$ identity matrix and null matrix, respectively; thus, in equation (2.15) both submatrices are 3×3. The elements of the submatrix U_{ij} correspond to the second partial derivatives of the pseudo-potential function with respect to the position states, $(x,\ y,\ z)$. Thus, U_{ij} takes on the following form,

$$U_{ij} = \begin{bmatrix} U_{xx} & U_{xy} & U_{xz} \\ U_{yx} & U_{yy} & U_{yz} \\ U_{zx} & U_{zy} & U_{zz} \end{bmatrix}\ . \tag{2.16}$$

The 3×3 submatrix Ω_3 is evaluated as

$$\Omega_3 = \begin{bmatrix} 0 & 1 & 0 \\ -1 & 0 & 0 \\ 0 & 0 & 0 \end{bmatrix}\ . \tag{2.17}$$

As is well known [20]-[21], the solution to equation (2.14) is written in the form

$$\bar{y}(t) = \Phi(t, t_0)\bar{y}_0\ , \tag{2.18}$$

where the vector $\bar{y}_0 = \bar{y}(t_0)$ is the initial variation relative to $\bar{x}_{ref}$, and $\Phi(t, t_0)$ is the state transition matrix. Clearly, at $t = t_0$, $\Phi(t_0, t_0) = I_6$. Substitution of equation (2.18) into equation (2.14) results in a set of 36 scalar differential equations that govern the elements of the 6×6 state transition matrix, $\Phi(t, t_0)$. These equations can be represented in matrix form as follows,

$$\dot{\Phi}(t, t_0) = A(t)\Phi(t, t_0) \ . \tag{2.19}$$

The matrix equation (2.19), combined with the first order form of the EOMS, equations (2.10)-(2.12), comprise a set of 42 scalar, nonlinear, ordinary differential equations that must be solved simultaneously via a numerical integration scheme.

2.2 Particular Solutions

As stated earlier, in the six-dimensional phase space of the CR3BP, there exist an infinite number of solutions that satisfy the equations of motion. To simplify the process of numerically identifying six-dimensional arcs along particular solutions in the CR3BP that resemble cometary motion during TSC, knowledge of the types of motion that can be expected is valuable. This understanding is developed by considering known particular solutions to the equations of motion: equilibrium solutions and periodic orbits. Also, further insight is developed by considering three-dimensional representations of pseudo-energy levels along a family of particular solutions.

2.2.1 Libration Points

The most familiar particular solution to equations (2.10)-(2.12) is the equilibrium solution. In the CR3BP, five equilibrium locations exist. In 1772, Leonhard Euler and Joseph-Louis Lagrange [22] shared the award from the Académie des Sciences of Paris for the discovery of these five equilibrium points. The relative configuration of these points (L_i, $i = 1, \ldots 5$) for the Sun-Jupiter system appears in Figure 2.2. Note that the mass ratio in the Sun-Jupiter system is $\mu = 9.5388 \times 10^{-4}$. This indicates that the Sun and the barycenter are in close proximity ($\approx 742 \times 10^3$ km), consistent with Figure 2.2. Also apparent in this figure, three of the equilibrium (or libration) points lie on the line joining the primaries (x-axis). These points are termed the

collinear libration points. For notational purposes, L_1 is defined as the collinear point that lies between the primaries, L_2 is located beyond the smaller primary (P_2) along the positive x-axis, and L_3 is positioned on the opposite side of P_1 at a distance approximately equal to L_{ref}, along the negative x-axis. The remaining two points, also labeled Lagrange points, are in the xy-plane and lie at the vertices of equilateral triangles with the primaries.

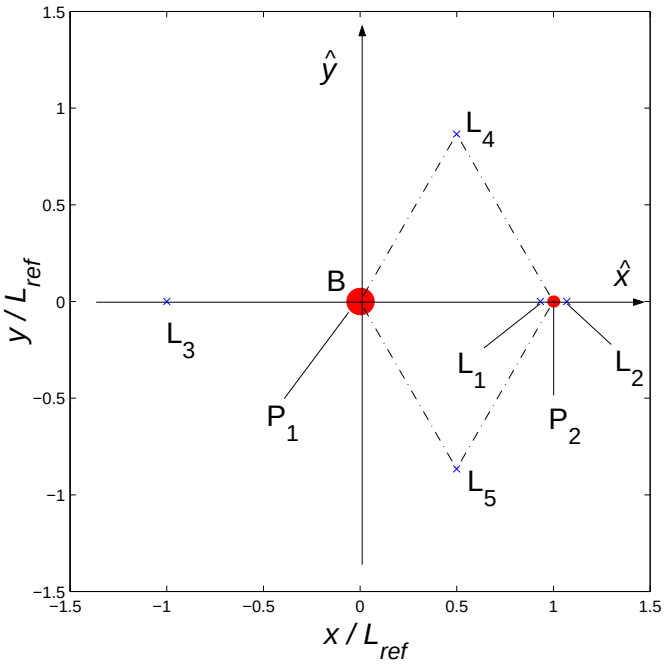

Figure 2.2. CR3BP Libration Points in the Sun-Jupiter System

2.2.2 Periodic Orbits

As previously stated, no closed-form analytical solution exists to the equations of motion in the CR3BP. However, linear analysis of equations (2.10)-(2.12) suggests the existence of periodic and quasi-periodic solutions in the vicinity of the libration points. Consequently, several researchers (including R. Farquhar and A. Kamel [23], D. Richardson [24] and N. Cary [25], C. Marchal [26], as well as G. Gómez, A. Jorba, J. Masdemont and C. Simó [27]) have developed higher order analytical approximations to represent this type of motion. For example, Richardson [24] develops a third order approximation for periodic motion near L_1 and L_2 in the Sun-Earth system.

Such approximations are based on expansions relative to the libration points. Thus, although these approximations provide great insight into the motion *near* the libration points, the range of validity is limited. Consequently, to more fully explore the solution space, these approximations must ultimately be combined with numerical techniques to more accurately identify a periodic solution. Of course, any periodic orbit can be represented simply by a set of initial conditions. Hence, a search for a periodic orbit reduces to a search for an accurate initial state vector. For instance, as an initial guess, the equations of motion are numerically integrated using a set of initial conditions based on an analytical approximation. Then, a differential corrections process is implemented to adjust the initial states until, numerically, the periodicity of the solution is established. The available analytical approximations are typically based on parameters in the Sun-Earth or Sun-Earth-Moon system ($\mu \approx 3 \times 10^{-6}$); the comet analysis here corresponds to the Sun-Jupiter system ($\mu \approx 9 \times 10^{-4}$). Rather than derive new approximations for a system with a higher μ value, a combination of numerical μ-continuation and differential corrections is used here to successfully map a set of initial conditions to the Sun-Jupiter system.

Naturally, there are an infinite number of periodic solutions that satisfy the equations of motion in the CR3BP. Halo orbits, in the vicinity of the collinear libration points, are among these solutions. Halo orbits (and, consequently, halo families) are three-dimensional and result from the bifurcation of a family of planar periodic orbits (Lyapunov orbits) that exist in the xy-plane (M. Hénon [28], M. Michalodimitrakis [29] and S.S. Ichtiaroglou [30], I.A. Robin and V.V. Markellos [31], K.C. Howell and B.T. Barden [32]). Halo orbits associated with a specific collinear libration point are defined along a halo family, one such that each member corresponds to a different energy level (Jacobi Constant). For notational purposes, let SJL1 denote the Sun-Jupiter L_1 halo family and SJL2 denote the Sun-Jupiter L_2 halo family. These continuous, three-dimensional families are represented in Figure 2.3, in terms of projections on the xz-plane of a limited number of periodic trajectories that are members of these families. Note that the maximum out-of-plane components along these families, as

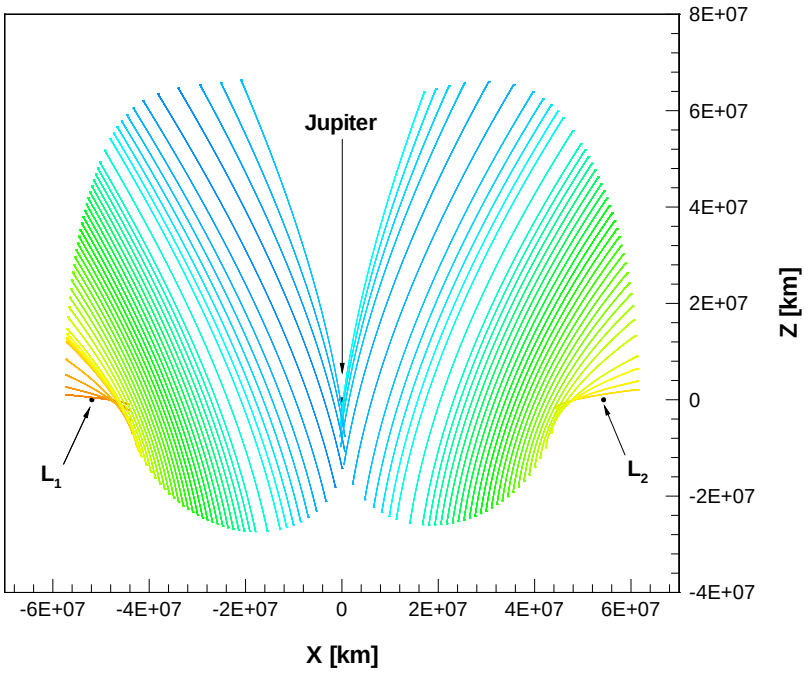

Figure 2.3. Sun-Jupiter L_1 and L_2 Halo Families

illustrated in Figure 2.3, are in the $+z$ direction. Particular halo orbits along a family, whose maximum out-of-plane component (A_z) is in the $+z$ direction are termed northern solutions. As will become apparent in the following section, it is simple to verify that for any single solution to the differential equations, there exists a second solution with out-of-plane component (z) that is simply of opposite sign. Hence, it follows that there exists a second set of halo orbits, similar to those illustrated in Figure 2.3, but mirrored across the rotating xy-plane. Halo orbits along these families, whose maximum out-of-plane excursion is in the $-z$ direction, are termed southern solutions. As an example, an L_1 northern halo orbit and a southern L_2 halo orbit, with similar out-of-plane amplitudes, are illustrated in Figure 2.4. In general, when projected onto the xy-plane, motion along both southern and northern L_1 and L_2 halo orbits appears to flow clockwise. However, projections onto the yz-plane might indicate otherwise. For example, while the direction of motion along the northern L_1 and southern L_2 halo orbits, illustrated in Figure 2.4, appears clockwise in both the

xy and yz planar projections, the same relation does not apply to a southern L_1 and northern L_2 halo orbits where motion seems to flow counterclockwise in the yz plane projection. As discussed later in greater detail, knowledge of the existence of the

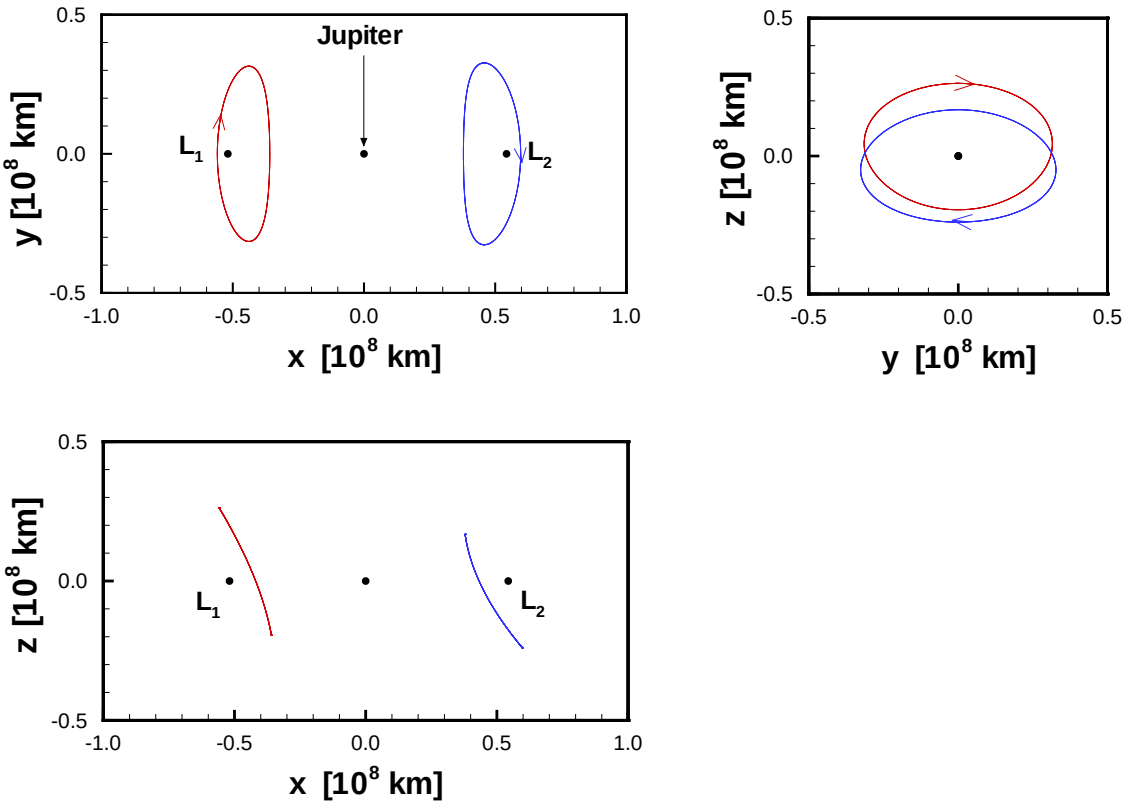

Figure 2.4. Northern L_1 and Southern L_2 Halo Orbits

northern and southern families is essential in identifying a solution whose dynamical characteristics are similar to those of a comet during TSC.

2.2.3 Analytical Symmetries

The form of the mathematical model for the CR3BP lends itself to various types of symmetries. The more obvious one is, of course, the xy-plane symmetry. That is, if $[x\ y\ z\ \dot{x}\ \dot{y}\ \dot{z}]^T$ satisfies the equations of motion, then so does $[x\ y\ -z\ \dot{x}\ \dot{y}\ -\dot{z}]^T$ as illustrated in Figure 2.5. This property leads to the existence of the northern and southern families of periodic halo orbits once the halo families bifurcate out of the xy-plane, as discussed in the previous section. The two halo families represented in

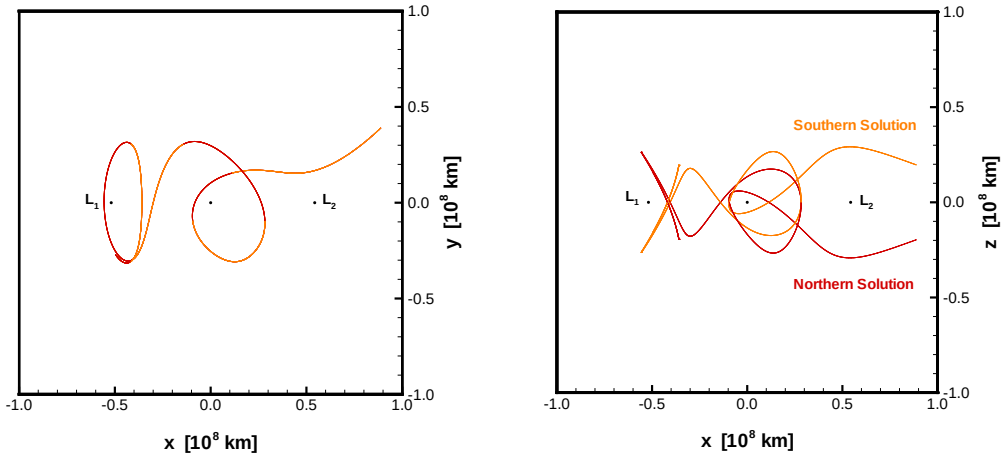

Figure 2.5. Northern/Southern Symmetry of Solutions

Figure 2.3 are both northern families of solutions. The northern/southern symmetry of solutions is defined here as symmetry property 1 (SP1).

The structure of the equations of motion also suggests time-invariance properties. That is, if the independent variable, time (t), is transformed to $\tau = -t$ it is clear that, if $[x\ y\ z\ \dot{x}\ \dot{y}\ \dot{z}]^T$ satisfies the EOMS for $\Delta t > 0$, then $[x\ \ -y\ z\ \ -\dot{x}\ \dot{y}\ \ -\dot{z}]^T$ satisfies the EOMS for $\Delta t < 0$. The symmetry due to time-invariance is defined here as symmetry property 2 (SP2) and is illustrated in Figure 2.6.

2.2.4 Regions of Exclusion

Recall the form of the expression for the Jacobi constant (C) in equation (2.13). Consider the conditions when $\dot{x} = \dot{y} = \dot{z} = 0$ for a given value of the pseudo-energy (C). That is, at a given energy level, the velocity of the comet is zero as observed in the rotating frame. For the sake of simplicity, suppose $z = z_0$, where z_0 is some prescribed out-of-plane component. The values of x and y that then satisfy equation (2.13) form a two-dimensional curve as observed in the rotating frame. This zero-velocity curve defines the region of configuration space, in the $z = z_0$ plane, that is available as the particle subsequently dynamically evolves. To cross a zero-velocity boundary requires an imaginary velocity; thus, these curves serve as an effective barrier along the path of a natural body such as a comet. Hence, these curves determine the two-

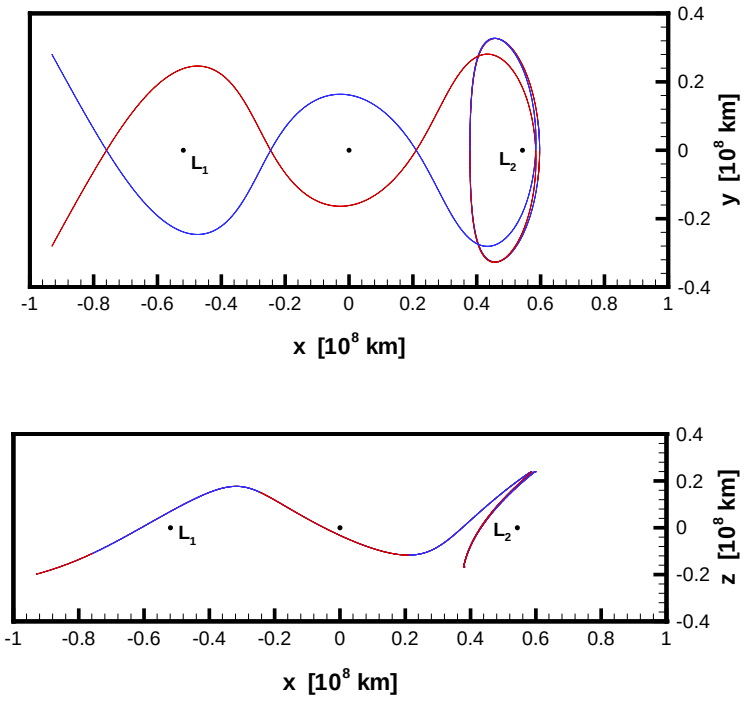

Figure 2.6. Symmetry of Solutions due to Time-Invariance

dimensional dynamical regions of exclusion as observed in the rotating frame. Any solution characterized by this value of C is bounded by this curve.

As an example, consider the case when $z_0 = 0$. A collection of zero-velocity curves are plotted in Figure 2.7 for C values ranging between $C_4 < C \leq C_1$ where C_j denotes the value of the Jacobi constant at the j^{th} libration point, $C_1 = 3.0388$, and $C_4 = C_5 = 2.9990$. Note, from Figure 2.7, that, for $C = C_1$, the regions of exclusion are determined by three closed contours, a large exterior curve that envelopes both P_1 and P_2, and two smaller contours, the largest surrounds P_1 and the smallest isolates P_2. As determined by these regions, a particle, P_3, can exist, dynamically, inside the two smaller contours near P_1 or P_2, or in the region exterior to the larger contour. However, since each contour is closed for $C = C_1$, it is not possible for P_3 to evolve across regions. A small decrease in C, $C = C_2$, allows the two interior curves to merge into a single contour that bridges the two interior regions. However, transitions to or from the region exterior to the orbit of P_2 are still not attainable. These transitions

require $C < C_2$ such that the interior and exterior zero-velocity curves merge into a single "C"-shaped contour. For $C < C_3$, the left end of this "C"-shaped curve collapses onto L_3 and, in the xy-plane but off the x-axis, two separate curves emerge that eventually collapse to the Lagrange points L_4 and L_5 as $C \to C_4$.

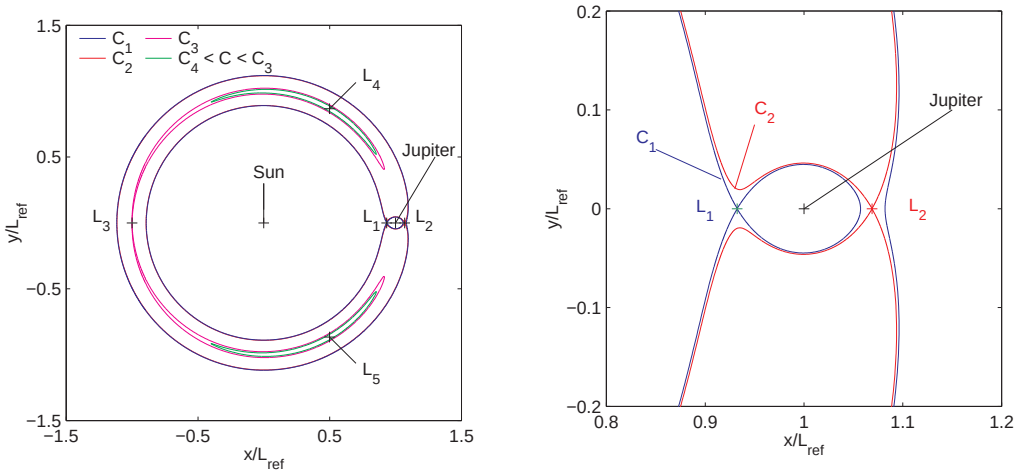

Figure 2.7. Two-Dimensional Regions of Exclusion for Various C Levels

Now, consider a fixed value of C and a range of values for z_0. In essence, the collection of two-dimensional curves (one for each value of z_0, where the curve for $z_0 = 0$ appears in Figure 2.7 forms a three-dimensional zero-velocity surface. Any three-dimensional solution characterized by this value of C is bounded by this surface in configuration space. Hence, this zero-velocity surface bounds the three-dimensional region of configuration space where the particle can dynamically evolve. For the Sun-Jupiter system, Figure 2.8 depicts a three-dimensional contour for $C = 3.0058$.

The Sun-Jupiter L_1 and L_2 halo families, depicted in Figure 2.3, correspond to a specific range of C. The associated zero-velocity surfaces are similar to that illustrated in Figure 2.8. In fact, $C = 3.0058$ reflects the pseudo-energy constant that corresponds to the largest member of the L_2 halo family that is represented in Figure 2.3. In essence, these surfaces apportion the configuration space into three regions: the interior region, the exterior region, and the capture region near Jupiter. As observed in Figure 2.8, the interior region reflects motion within the center spheroid;

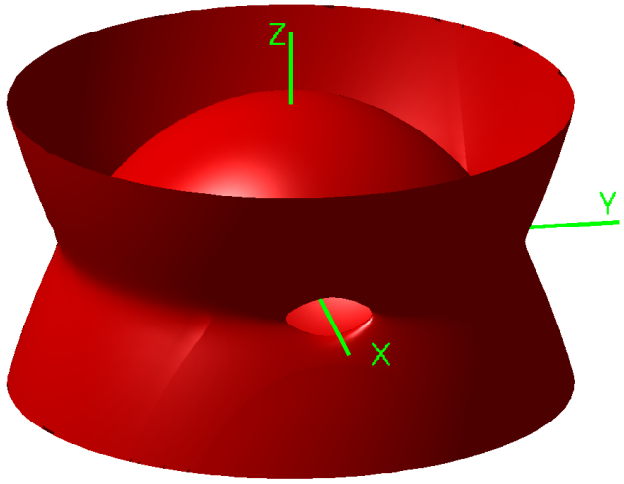

Figure 2.8. Three-Dimensional Region of Exclusion for $C = 3.0058$

the exterior region is defined as the space beyond the "pinched" cylindrical structure that surrounds the system; and, the capture region is seen as the relatively small opening that connects the available regions of motion. A comet on or near the Sun-Jupiter line (x-axis), and in the vicinity of the opening of the zero-velocity surface, can move across regions through this opening. Note that the interior region is closed except for the single connection to the capture region. Thus, in the CR3BP, the out-of-plane motion of a comet in the interior region remains bounded. The opening of the zero-velocity surface narrows as the Jacobi constant increases towards the value associated with the libration point L_2. At the same time, the out-of-plane dimension of the bounded interior region decreases with increasing C. Across the range of orbits in the SJL2 halo family that appears in Figure 2.3, this increase in C is equivalent to a decrease in the A_z amplitude of the orbit. Hence, for some prescribed value of C, the out-of-plane amplitude of the motion in the interior region is closely related to the A_z amplitude of a halo orbit with the same pseudo-energy level.

In the ephemeris model, a comet moving within the "interior region" is in an orbit contained within the heliocentric orbit of Jupiter. A comet moving in the "exterior region" is in an orbit that extends beyond the heliocentric orbit of Jupiter. A comet that shifts into the "capture region" is temporarily captured by Jupiter

and, thus, remains in the vicinity of the planet until it escapes and crosses into either the interior or exterior region. For the comets considered in this investigation, ephemeris information reveals that the out-of-plane motion of the comet, both inside the heliocentric orbit of Jupiter and in the vicinity of the planet, is bounded. Thus, by measuring the out-of-plane excursion along the actual (ephemeris) path of the comet in either the interior or capture regions, a value of the Jacobi constant, one that is associated with a solution in the CR3BP that is most likely to best resemble the overall features of the comet's path, can be estimated.

2.3 Invariant Manifold Theory

The process of identifying particular solutions, in the R3BP, that possess characteristics resembling the dynamical features along the path of a small natural body, temporarily captured by a planet, requires a thorough understanding of the geometry of the phase space [32]. The geometrical theory of dynamical systems (from Poincaré) is based on the phase portrait of a dynamical system as discussed in various mathematical sources including Wiggins [21], Guckenheimer and Holmes [33], Nayfeh and Mook [34], Perko [35], Hale [36], Nayfeh and Balachandran [37], Khalil [38], and Parker and Chua [20]. Equilibrium points and periodic solutions are two examples of the fundamental models available for the phase space, that is, invariant manifolds. Some of the concepts from invariant manifold theory have roots in linear stability analysis. Hence, some of the basic concepts of linear systems are reviewed. The background information presented here follows directly from the discussion in Parker and Chua [20], Guckenheimer and Holmes [33], and Perko [35] on continuous and discrete time autonomous systems.

2.3.1 Continuous Time Systems

Consider a general, autonomous, nonlinear vector field

$$\dot{\bar{x}} = \bar{f}(\bar{x}) \ , \tag{2.20}$$

where $\bar{x}(t) \in \mathbb{R}^n$ is the state vector at time t, $\dot{\bar{x}}$ represents the time derivative of $\bar{x}$, and $\bar{f} : U \rightarrow \mathbb{R}^n$ is a smooth function defined on some subset $U \subseteq \mathbb{R}^n$. A collection

of trajectories that represent the solutions to equation (2.20), in the phase space, is defined as a phase portrait of the system. In general, a phase portrait contains information about both the transient and asymptotic behavior of the solutions. Trajectories originating from different initial conditions describe the flow, $\phi_t(U)$, under the given system of equations. To demonstrate the dependence on the initial conditions, a single trajectory, representing the flow for all time t from initial conditions defined by $\bar{x}(t_0) = \bar{x}_0$, is often expressed in the form $\phi_t(\bar{x}_0)$. Then, the flow, $\phi_t(U)$, represents a one-parameter family of mappings such that $\phi_t : U \rightarrow \mathbb{R}^n$. Here it is assumed that for any time t, ϕ_t is a diffeomorphism. That is, the map ϕ_t is both smooth and invertible.

From a dynamical systems perspective, the structure and geometry of the phase space are typically studied by considering particular solutions to the differential equations and the associated local flow. For most applications, the local behavior of the flow can be determined through linear stability analysis. As a simple example consider the flow in the vicinity of the libration point L_i, in the Sun-Jupiter-comet system. Let $\bar{x}_{eq}$, the six-dimensional equilibrium state at L_i, represent the reference solution, $\bar{x}_{ref} = \bar{x}_{eq}$. A phase portrait of the flow near L_i consists of trajectories with initial conditions in the immediate vicinity of $\bar{x}_{eq}$. Hence, let $\bar{y}$ denote a small perturbation relative to $\bar{x}_{eq}$ such that $\bar{x} = \bar{x}_{eq} + \bar{y}$. Assuming that $\bar{f}$ is at least $\mathcal{C}^2$, and expanding the vector field in a Taylor series about $\bar{x}_{eq}$ – retaining only the linear terms – leads to the variational equation,

$$\dot{\bar{y}}(t) = A\bar{y}(t) \ , \tag{2.21}$$

where A is the $n \times n$ matrix of first partial derivatives or Jacobian matrix. Note that, since $\bar{x}_{eq}$ is an equilibrium solution of equation (2.20), the elements of A are constant. (However, in general, if the reference solution, $\bar{x}_{ref}$, is time-varying, then $A = A(t)$). If the system matrix is constant, the solution of equation (2.21) can be written in the form

$$\bar{y}(t) = e^{(t-t_0)A}\bar{y}(t_0) \ , \tag{2.22}$$

where

$$e^{(t-t_0)A} = \sum_{j=1}^{\infty} \frac{(t-t_0)^j}{j!} A^j \ . \tag{2.23}$$

Furthermore, if the eigenvalues (η_j) of A are distinct, then there exists a matrix $S = [\bar{S}_1 \ \bar{S}_2 \ \ldots \ \bar{S}_n]$ such that $S^{-1}AS = \Lambda$, where Λ is a diagonal matrix with entries $\eta_1, \eta_2, \ldots, \eta_n$ and the j-th column of S, that is $\bar{S}_j$, corresponds to the eigenvector associated with η_j. If the eigenvalues are complex, the matrix S is also complex. Since the eigenvalues are distinct, the eigenvectors are linearly independent; thus, the matrix S is nonsingular. Hence, equation (2.22) can be simplified as follows

$$\bar{y}(t) = Se^{\Lambda(t-t_0)}S^{-1}\bar{y}(t_0) \ . \tag{2.24}$$

The matrix $e^{\Lambda(t-t_0)}$ is diagonal with entries $e^{\eta_j(t-t_0)}$. Hence, the eigenvalues of A are also known as the characteristic exponents of the local flow. The solution represented by equation (2.24) can now be written in a form that reveals the fundamental dynamical components of the motion,

$$\bar{y}(t) = \sum_{j=1}^{n} c_j e^{\eta_j(t-t_0)} \bar{S}_j \ . \tag{2.25}$$

In equation (2.25), the coefficients c_j are determined from the initial state, $\bar{y}(t_0)$.

2.3.2 Eigenspaces and Invariant Manifolds

For the system described by equation (2.21), let A possess n_s eigenvalues with positive real parts, n_u eigenvalues with negative real parts and n_c eigenvalues with zero real parts, such that $n = n_s + n_u + n_c$. Since the eigenvectors corresponding to these eigenvalues are linearly independent, they span $\mathbb{R}^n$. Thus, $\mathbb{R}^n$ can be represented as the sum of the three fundamental subspaces E^s, E^u, and E^c; note that E^s, E^u, and E^c are invariant subspaces of the corresponding linear system. That is, by appropriate choice of the initial conditions, a solution that is initially contained entirely within a given subspace remains in this subspace for all time. Thus, solutions initiated in E^s approach $\bar{y} = \bar{0}$ as $t \to +\infty$, solutions with initial conditions in E^u approach $\bar{y} = \bar{0}$ as $t \to -\infty$, and initial state vectors in E^c yield solutions that neither grow

nor decay in time relative to $\bar{y} = \bar{0}$. These facts lead to the following definitions. The local stable manifold (W^s_{loc}), associated with $\bar{x}_{eq}$, is the set of all initial conditions, in a neighborhood of $\bar{x}_{eq}$, such that the flow initiated at these states asymptotically approaches $\bar{x}_{eq}$ as $t \to +\infty$. Similarly, the local unstable manifold (W^u_{loc}) is the set of all initial conditions, near $\bar{x}_{eq}$, such that the flow initiated at these states asymptotically approaches $\bar{x}_{eq}$ as $t \to -\infty$. If all the eigenvalues of A have non-zero real parts, $\bar{x}_{eq}$ is defined as a hyperbolic equilibrium point. For an equilibrium point, the local stable and unstable manifolds are related to the invariant subspaces E^s and E^u of the linear system via the Stable Manifold Theorem (Guckenheimer and Holmes [33]):

Theorem 2.1 *(Stable Manifold Theorem for Flows). Suppose that $\dot{\bar{x}} = f(\bar{x})$ has a hyperbolic equilibrium point $\bar{x}_{eq}$. Then there exist local stable and unstable manifolds $W^s_{loc}(\bar{x}_{eq})$, $W^u_{loc}(\bar{x}_{eq})$, of the same dimensions n_s, n_u as those of the eigenspaces E^s and E^u of the linearized system (2.21), and tangent to E^s and E^u at $\bar{x}_{eq}$. $W^s_{loc}(\bar{x}_{eq})$, $W^u_{loc}(\bar{x}_{eq})$ are as smooth as the function $\bar{f}$.*

To better visualize the significance of Theorem 2.1, let $\bar{x}_{eq}$ be an equilibrium point of a two-dimensional first order system, with eigenvalues η_s and η_u, such that the eigenvectors, $\bar{v}_s$ and $\bar{v}_u$, span E^s and E^u, respectively. Hence, $\bar{v}_s$ and $\bar{v}_u$ form a vector basis for $\mathbb{R}^2$. The stable subspace, E^s, is then defined as the line segment that extends along $+\bar{v}_s$ and $-\bar{v}_s$. Similarly, E^u extends along $+\bar{v}_u$ and $-\bar{v}_u$. Since W^s_{loc} and W^u_{loc} are tangent to E^s and E^u at $\bar{x}_{eq}$, the corresponding local stable manifold, associated with $\bar{x}_{eq}$, is formed by the union of two half-manifolds, W^{s+}_{loc} and W^{s-}_{loc}, as represented in Figure 2.9. Similarly, the local unstable manifold is formed by the union of W^{u+}_{loc} and W^{u-}_{loc}.

For higher order systems, a one-dimensional invariant subspace is analogous to a line segment in $\mathbb{R}^2$, as illustrated in Figure 2.9. Similarly, a two-dimensional subspace in $\mathbb{R}^2$ is equivalent to a hyperplane in $\mathbb{R}^n$. Furthermore, the local invariant manifolds, W^s_{loc} and W^u_{loc}, have global analogs, W^s and W^u, obtained by propagating the flow

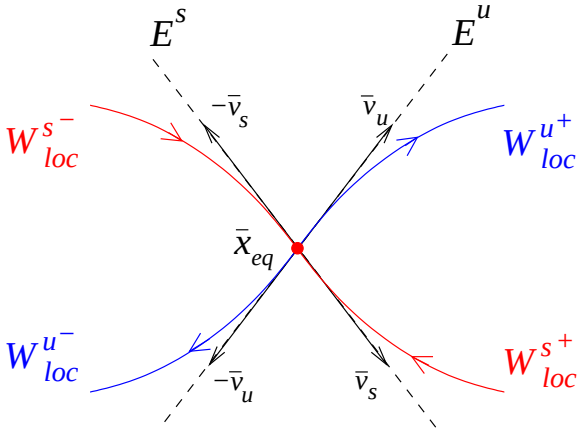

Figure 2.9. Stable Manifold Theorem

backwards in time along W^s_{loc} and forward in time along W^u_{loc}:

$$W^s(\bar{x}_{ref}) = \bigcup_{t\leq 0} \phi_t \left[W^s_{loc}(\bar{x}_{ref})\right] \ , \tag{2.26}$$

$$W^u(\bar{x}_{ref}) = \bigcup_{t\geq 0} \phi_t \left[W^u_{loc}(\bar{x}_{ref})\right] . \tag{2.27}$$

Note that equations (2.26)-(2.27) are expressed in terms of a general reference solution, $\bar{x}_{ref}$, to preserve the generality of the definition. For an equilibrium point, $\bar{x}_{ref} = \bar{x}_{eq}$.

Now, suppose $\bar{x}_{eq}$ is a non-hyperbolic equilibrium point. In particular, consider the case when n_s, n_u, and n_c are all non-zero. That is, $\Re(\eta_j) < 0$ for $j = 1 \ldots n_s$, $\Re(\eta_k) > 0$ for $k = 1 \ldots n_u$, and $\Re(\eta_i) = 0$ for $i = 1 \ldots n_c$. In this case, the structure of the local flow is determined by the Center Manifold Theorem (Guckenheimer and Holmes [33]). Note, in Theorem 2.2, the form of the system is such that $\bar{x}_{eq} = \bar{0}$ and $D\bar{f}(\bar{x}_{eq})$ denotes the Jacobian matrix, A, evaluated at $\bar{x}_{eq}$.

Theorem 2.2 *(Center Manifold Theorem for Flows). Let $\bar{f}$ be a $\mathcal{C}^r$ vector field on $\mathbb{R}^n$ vanishing at the origin ($\bar{f}(\bar{0}) = \bar{0}$) and let $A = D\bar{f}(\bar{0})$. Divide the spectrum of A into three parts, n_s, n_c, and n_u with*

$$\Re(\eta) \begin{cases} < 0 \ ; \ \eta \in n_s \\ = 0 \ ; \ \eta \in n_c \\ > 0 \ ; \ \eta \in n_u \end{cases} \tag{2.28}$$

Let the (generalized) eigenspaces of n_s, n_c, and n_u be E^s, E^c, and E^u, respectively. Then, there exist $\mathcal{C}^r$ stable and unstable invariant manifolds W^u and W^s tangent to E^u and E^s at $\bar{0}$ and a $\mathcal{C}^{r-1}$ center manifold W^c tangent to E^c at $\bar{0}$. The manifolds W^u, W^s, and W^c are all invariant for the flow $\bar{f}$. The stable and unstable manifolds are unique, but W^c need not be.

The existence of the center manifold suggests that the structure of the flow near an equilibrium point, possessing at least one zero eigenvalue, is more diverse than that of an equilibrium point with no center subspace. Recall that solutions initiated in the center manifold neither grow nor decay in time, relative to $\bar{x}_{eq}$. Periodic orbits and quasi-periodic trajectories are examples of the types of motion that might exist in the center manifold near $\bar{x}_{eq}$. In the CR3BP, the collinear libration points (L_i, $i = 1, \ldots, 3$) possess a four-dimensional center manifold, and one-dimensional stable and unstable manifolds. In-plane Lyapunov orbits and nearly vertical out-of-plane orbits are examples of periodic solutions that exist in the center manifold near L_i. Lyapunov orbits exist in the plane of motion of the primaries. Their amplitudes increase as the maximum excursion in the direction parallel to the y-axis, shifts further from $\bar{x}_{eq}$. At the critical amplitude, three-dimensional periodic halo orbits in the vicinity of L_i bifurcate from the two-dimensional Lyapunov orbits (M. Hénon [28], M. Michalodimitrakis [29] and S.S. Ichtiaroglou [30], I.A. Robin and V.V. Markellos [31], K.C. Howell and B.T. Barden [32]). These types of solutions represent only a small subset of the solutions that exist in the center manifold near L_i.

The focus of this study is the identification of segments along three-dimensional solutions, in the phase space of the R3BP, that exhibit dynamical features similar to those of a captured comet. The path of such comets is both three-dimensional and chaotic in nature and flows towards and away from the capture region. Hence, periodic orbits and quasi-periodic trajectories are not themselves representative of the capture mechanism. In fact, the *in-plane* features of temporary satellite capture are best described by the stable and unstable manifolds associated with the equilibrium/libration points, L_i. However, the out-of-plane component is not insignificant

for the comets considered in this study. Thus, it is necessary to consider the stable and unstable manifolds associated with **three-dimensional** periodic orbits and quasi-periodic trajectories. The Center Manifold Theorem, as presently stated, is only applicable to equilibrium points. To assess the stability of periodic and quasi-periodic solutions near L_i, it is necessary to consider an alternate representation of a dynamical system, that is, a discrete map.

2.3.3 Reduction to a Discrete Time Dynamical System

Any map $P : \mathbb{R}^n \rightarrow \mathbb{R}^n$ defines a discrete dynamical system through the state equation,

$$\bar{x}_{k+1} = P\bar{x}_k \tag{2.29}$$

where $\bar{x}_k \in \mathbb{R}^n$ is the state and P maps the state from $\bar{x}_k$ to $\bar{x}_{k+1}$. A useful technique to analyze dynamical systems is the classical approach that replaces the flow, $\phi_t(\bar{x}_0)$, of an n^{th}-order continuous-time system, with an $(n-1)^{th}$-order discrete-time system. This process results in the classical Poincaré map. Consider an n^{th}-order autonomous system with limit cycle Γ. A limit cycle is an attracting set to which orbits or trajectories converge, and upon which trajectories are periodic. Let Σ be an $(n-1)$-dimensional hyperplane transverse to Γ at $\bar{x}^*$. The periodic trajectory defined by $\bar{x}^*$ intersects Σ again at $\bar{x}^*$ within some minimum period T of the limit cycle. Thus, $\bar{x}^*$ is a fixed point of P. Since the flow, ϕ_t, of the nonlinear system is assumed to be smooth and continuous with respect to $\bar{x}^*$, trajectories starting on Σ in a sufficiently small neighborhood of $\bar{x}^*$ will, in approximately T time units, intersect Σ in the vicinity of $\bar{x}^*$. Hence ϕ_t, and thus, Σ, define a mapping P of some neighborhood $U \subset \Sigma$ of $\bar{x}^*$ onto another neighborhood $V \subset \Sigma$ of $\bar{x}^*$. The map P is defined as a Poincaré map of the autonomous system. A portrait of a Poincaré map, representative of a second order system, is illustrated in Figure 2.10. Note that the map P is defined only in the neighborhood of $\bar{x}^*$. Thus, there is no guarantee that a trajectory emanating from any point in Σ will subsequently return to Σ. Also, P is a diffeomorphism and is therefore invertible and differentiable. A proof of this statement is available in Parker and Chua [20].

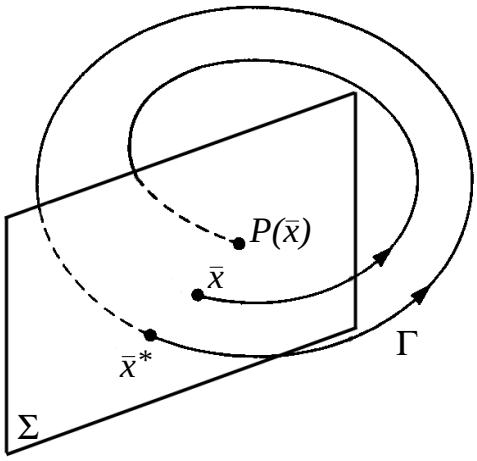

Figure 2.10. Poincaré Section - Adapted from Parker and Chua [20]

2.3.4 Periodic Solutions and Maps

In the CR3BP, solutions to the variational equation (2.14) can be expressed as a function of the initial conditions and the corresponding state transition matrix, as defined in equation (2.18). Consider a periodic orbit, $\Gamma = \Gamma(t)$, as the reference solution of interest, $\bar{x}_{ref}$. In its present form, the solution defined by equation (2.18) corresponds to a flow that reflects a continuous trajectory. This continuous arc can be envisioned as an infinite set of discrete states, sampled at Δt intervals for $\Delta t \to 0$. Among this infinite set, a single state, $\bar{x}^*$, completely represents a periodic orbit in a Poincaré map. Without loss of generality, let $\bar{x}^* = \bar{x}(t_0)$ for $t_0 = 0$. Since equation (2.18) governs the evolution of the perturbation $\bar{y}(0)$ in a neighborhood of $\bar{x}^*$, the state $\bar{x}(nT)$ can be estimated as

$$\begin{aligned} \bar{x}(nT) &= \bar{x}^* + \bar{y}(nT) \ , \\ &= \bar{x}^* + \Phi(nT, 0)\bar{y}(0) \ , \\ &= \bar{x}^* + \sum_{j=1}^{n} c_j \lambda_j^n \bar{v}^{(j)} \ , \end{aligned} \tag{2.30}$$

where c_j represent complex constants determined from the initial perturbation, $\bar{y}(0)$. The λ_j's are the eigenvalues of the monodromy matrix $\Phi(T, 0)$, that is, the state transition matrix (STM) evaluated after one period. To simplify the form of the solution in equation (2.30), the eigenvalues are assumed to be distinct. Then, $\bar{v}^{(j)}$ are

the corresponding eigenvectors. Note that, since $\Gamma = \Gamma(t)$ represents a solution in the nonlinear flow, $\Gamma(t)$ must satisfy equation (2.20). That is,

$$\dot{\Gamma}(t) = \bar{f}[\Gamma(t)] \ . \tag{2.31}$$

Differentiation of equation (2.31) with respect to time yields,

$$\begin{aligned} \ddot{\Gamma}(t) &= Df[\Gamma(t)]\dot{\Gamma}(t) \\ &= A[\Gamma(t)]\dot{\Gamma}(t) \ . \end{aligned} \tag{2.32}$$

Thus, $\dot{\Gamma}(t)$ must satisfy the variational equation (2.21). Since Γ denotes a periodic orbit, $\dot{\Gamma}(T) = \dot{\Gamma}(0) = \bar{f}(\bar{0})$. Furthermore, equation (2.19) must also be satisfied. This implies that $\bar{f}(\bar{0}) = \Phi(T, 0)\bar{f}(\bar{0})$. That is, for a periodic orbit to exist, the monodromy matrix must possess at least one eigenvalue at unity, with eigenvector $\bar{f}(\bar{0})$. The stability of the periodic orbit, defined by the fixed point $\bar{x}^*$, is then determined by the position of the remaining eigenvalues in the complex plane.

2.3.5 Stability of Periodic Orbits

The linearization of equation (2.20) relative to a periodic orbit (Γ) results in a nonautonomous system of equations defined in equation (2.14), where $A(t)$ is a T-periodic matrix ($A(t) = A(t + T)$). Consequently, the elements of $A(t)$ are functions of time and the stability results established for equilibrium points are not applicable. However, a nonautonomous linear system can be reduced to an autonomous system by appropriate choice of coordinates. Let $t_0 = 0$ and consider the following theorem (Perko [35]):

Theorem 2.3 *(Floquet's Theorem) If $A(t)$ is a continuous T-periodic matrix, then for all $t \in \mathbb{R}$ any fundamental matrix solution for (2.14) can be written in the form*

$$\Phi(t, 0) = Q(t, 0)e^{Bt} \tag{2.33}$$

where $Q(t, 0)$ is a nonsingular, differentiable, T-periodic matrix and B is a constant matrix. Furthermore, if $\Phi(0, 0) = I_n$ then $Q(0, 0) = I_n$.

Corollary 2.1 *Under the hypotheses of Theorem (2.3), the nonautonomous linear system (2.14), under the linear change of coordinates*

$$\bar{w}(t) = Q^{-1}(t,0)\bar{y}(t) \tag{2.34}$$

reduces to the autonomous linear system

$$\dot{\bar{w}}(t) = B\bar{w}(t) \tag{2.35}$$

A proof of Corollary (2.1) is detailed in Perko [35]. Note that, by Corollary (2.1), the stability properties of the nonautonomous linear system defined in equation (2.14), are equivalent to those of the autonomous linear system in equation (2.35). Consequently, since $Q(T,0) = Q(0,0) = I_6$ and $\Phi(T,0) = e^{BT}$, the eigenvalues of the monodromy matrix correspond to the eigenvalues of e^{BT}, that is, the characteristic multipliers (λ_j). Although the eigenvalues of $\Phi(T,0)$ are uniquely determined for a given periodic orbit, neither the matrix B nor its eigenvalues are uniquely determined for the system described in equation (2.21). For example, equation (2.33) can be replaced by $\Phi(t,0) = \tilde{Q}(t,0)e^{\tilde{B}t}$ where $\tilde{Q} = Q(t,0)e^{2\pi i t}$ and $\tilde{B} = B - 2\pi i I_n$. The eigenvalues of B are termed the characteristic exponents (β_j). For $\beta_j = a_j + ib_j$, the characteristic exponents are related to the characteristic multipliers, λ_j, through the following relation

$$\lambda_j = e^{\beta_j T}\ , \tag{2.36}$$

$$= e^{a_j}(\cos b_j + i \sin b_j)\ . \tag{2.37}$$

Based on equation (2.37), the following must be true

$$a_j > 0 \rightarrow \|\lambda_j\| > 1,$$
$$a_j < 0 \rightarrow \|\lambda_j\| < 1,$$
$$a_j = 0 \rightarrow \|\lambda_j\| = 1.$$

Thus, if k eigenvalues of B have negative real parts, then the monodromy matrix possesses k eigenvalues situated inside the unit circle in the complex plane. Similarly,

if j eigenvalues of B have positive real parts, then the corresponding j characteristic multipliers are located outside the unit circle. If, instead, the real part of an eigenvalue of B is zero, then the corresponding characteristic multiplier lies on the unit circle in the complex plane. The stability of a periodic orbit is thus determined by the real part of the characteristic exponents, or the modulus of the characteristic multipliers, as apparent in equation (2.30) and established by the following theorem (Perko [35]).

Theorem 2.4 *(The Stable Manifold Theorem for Periodic Orbits). Let* $\bar{f} \in \mathcal{C}^1(E)$ *where* E *is an open subset of* $\mathbb{R}^n$ *containing a periodic orbit*

$$\Gamma : \ \bar{x} = \gamma(t) \ ,$$

of (2.20) of period T*. Let* ϕ_t *be the flow of (2.20) and* $\gamma(t) = \phi_t(\bar{x}^*)$*. If* k *of the characteristic exponents of* $\gamma(t)$ *have negative real part where* $0 \leq k \leq n-1$ *and* $n-k-1$ *of them have positive real part then there is a* $\delta > 0$ *such that the stable manifold of* Γ*,*

$$S(\Gamma) = \{\bar{x} \in N_\delta(\Gamma) \mid d(\phi_t(\bar{x}), \Gamma) \to 0 \ as \ t \to \infty \ and \ \phi_t(\bar{x}) \in N_\delta(\Gamma) \ for \ t \geq 0\}$$

is a $(k+1)$*-dimensional, differentiable manifold which is positively invariant under the flow* ϕ_t *and the unstable manifold of* Γ*,*

$$U(\Gamma) = \{\bar{x} \in N_\delta(\Gamma) \mid d(\phi_t(\bar{x}), \Gamma) \to 0 \ as \ t \to -\infty \ and \ \phi_t(\bar{x}) \in N_\delta(\Gamma) \ for \ t \leq 0\}$$

is an $(n-k)$*-dimensional, differentiable manifold which is negatively invariant under the flow* ϕ_t*. Furthermore, the stable and unstable manifolds of* Γ *intersect transversally in* Γ*.*

Once more, the local stable and unstable manifolds of Γ, $S(\Gamma) = W^s_{loc}(\Gamma)$ and $U(\Gamma) = W^u_{loc}(\Gamma)$, in Theorem (2.4) can be utilized to define the global stable and unstable manifolds associated with Γ, that is, $W^s(\Gamma)$ and $W^u(\Gamma)$, by defining states along W^s_{loc} and propagating the flow backwards in time, and, then, states along W^u_{loc} forward in time. Note that $W^s(\Gamma)$ and $W^u(\Gamma)$ are unique, invariant, differentiable

manifolds of the same dimensions as $W^s_{loc}(\Gamma)$ and $W^u_{loc}(\Gamma)$, respectively. Also, $W^s(\Gamma)$ and $W^u(\Gamma)$ are tangent to the stable and unstable subspaces $E^s(\Gamma)$ and $E^u(\Gamma)$ of Γ at the point $\bar{x}^*$. The difference between $W^s(\Gamma)$ and $W^s(\bar{x}^*)$ is a significant issue. Recall that, by the definition of a Poincaré map, the fixed point $\bar{x}^*$ is an $(n-1)$-dimensional representation of Γ, a periodic orbit in $\mathbb{R}^n$. Suppose that the monodromy matrix associated with $\bar{x}^*$ possesses m eigenvalues of modulus one, j of modulus greater than one, and k eigenvalues of modulus less than one. The stable, unstable, and center subspaces associated with $\bar{x}^*$ are then defined with dimensions m, j, and k, respectively. However, as stated by Theorem (2.4), the stable manifold associated with Γ, $W^s(\Gamma)$, is of dimension $k+1$ and $W^u(\Gamma)$ is of dimension $j+1$. To illustrate the added dimension, consider a two-dimensional system ($n=2$), where the unstable subspace, E^u, associated with $\bar{x}^*$ is one-dimensional. Recall that Σ is the $(n-1)$-dimensional hyperplane transverse to Γ at $\bar{x}^*$. Let $\bar{y}(t_j)$ denote a state, perturbed from $\bar{x}^*$ along E^u. The unstable manifold associated with $\bar{x}^*$, $W^u(\bar{x}^*)$, is formed by a set of discrete points on Σ that asymptotically depart $\bar{x}^*$ with each successive iteration of the map P. Thus, $W^u(\bar{x}^*)$ is a one-dimensional manifold. However, since $\bar{x}^*$ is an $(n-1)$-dimensional representation of Γ, the unstable manifold associated with Γ, $W^u(\Gamma)$, is a two-dimensional surface in $\mathbb{R}^2$. This is illustrated in Figure 2.11. The dimensions of $W^s(\Gamma)$ and $W^u(\Gamma)$ are always one degree higher than the dimension of E^s and E^u, respectively. Note that Theorem (2.4) addresses only $n-1$ eigenvalues,

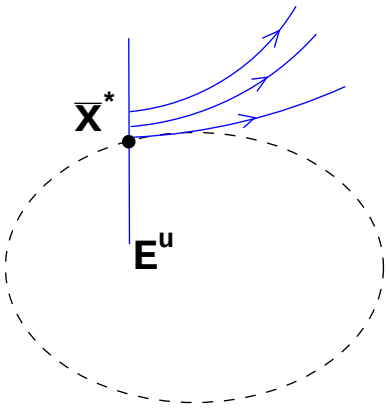

Figure 2.11. Dimension of the Unstable and Stable Manifolds

since, as previously stated, at least one of the characteristic multipliers must have a modulus of one for a periodic orbit to exist. If only one of the eigenvalues has modulus one, Γ is an isolated periodic orbit and Theorem (2.4) is applicable as stated. That is, all solutions in a neighborhood of Γ lie either on $W^s_{loc}(\Gamma)$ or $W^u_{loc}(\Gamma)$. Otherwise, the results of Theorem (2.4) must be extended to include the center manifold (Perko [35]).

Theorem 2.5 *(The Center Manifold Theorem for Periodic Orbits) Let* $\bar{f} \in \mathcal{C}^r(E)$ *with* $r \geq 1$ *where* E *is an open subset of* $\mathbb{R}^n$ *containing a periodic orbit*

$$\Gamma \ : \ \bar{x} = \gamma(t)$$

of (2.20) of Period T*. Let* ϕ_t *be the flow of (2.20) and let* $\gamma(t) = \phi_t(\bar{x}^*)$*. If* k *of the characteristic exponents have negative real part,* j *have positive real part and* $m = n - k - j$ *have zero real part, then there is an* m*-dimensional center manifold of* Γ*,* $W^c(\Gamma)$*, of class* $\mathcal{C}^r$ *which is invariant under the flow* ϕ_t*. Furthermore,* $W^s(\Gamma)$*,* $W^u(\Gamma)$ *and* $W^c(\Gamma)$ *intersect transversally in* Γ *and if the origin has been translated to the point* $\bar{x}^*$ *so that* $\gamma(t) = \phi_t(\bar{0})$*, then* $W^c(\Gamma)$ *is tangent to the center subspace of* Γ*,* E^c*, at the point* $\bar{0} \in \Gamma$*.*

Recall, state vectors initially in E^c neither grow nor decay relative to $\bar{x}^*$. For example, solutions with initial states in E^c can lead to nearby periodic or quasi-periodic solutions. Although, in the CR3BP, the center manifold represents a significant subset of the phase space, as discussed by Howell and Barden [32], the motion of interest in this study is more consistent with trajectories that lie on stable and unstable manifolds. Thus, the discussion in the following sections is focused on the relative geometry of the stable and unstable manifolds and the flows associated with a single periodic orbit.

2.3.6 Time-Invariance Properties of the STM

To understand the geometry of the flow along the stable and unstable manifolds that are associated with periodic orbits in the CR3BP, it is necessary to examine

some of the properties of the state transition matrix. In particular, one of the most useful properties of the STM is derived from the time-invariance of the linear system. To preserve the generality of the time-invariance properties, consider first the general form of the solution to equation (2.14), as expressed in equation (2.18). Define the following coordinate transformation

$$\bar{y}(t) = G\bar{\xi}(\tau) \ , \tag{2.38}$$

where the new independent time variable is defined as $\tau = -t$ and G is a constant nonsingular matrix. Substitution of equation (2.38) into equation (2.14) reveals that

$$A(t) = -GA(-t)G^{-1} \ . \tag{2.39}$$

Since equation (2.39) must hold true for all time t, then $A(-t) = -GA(t)G^{-1}$ is also true for all t. However, this relation leads to

$$A(t) = -G^{-1}A(-t)G \ . \tag{2.40}$$

For both equations (2.39) and (2.40) to be satisfied, $G = G^{-1}$ and thus $G^2 = I_n$ for $G \neq I_n$. Here, I_n is the $n \times n$ identity matrix. An example of a matrix G that satisfies $G^2 = I_n$ and $G \neq I_n$ is the diagonal matrix defined as follows,

$$G(i,i) = (-1)^{(i+1)} \ , \tag{2.41}$$

where i denotes the row and column of the corresponding diagonal entry. All the off-diagonal entries in G are zero.

The coordinate transformation defined in equation (2.38) must also satisfy the discretized form of the solution, equation (2.18). Substitution of equation (2.38) into equation (2.18) produces

$$\begin{aligned} \bar{y}(t) &= \Phi(t,t_0)\bar{y}_0 \ , \\ G\bar{\xi}(\tau) &= \Phi(t,t_0)G\bar{\xi}_0 \ , \\ \bar{\xi}(\tau) &= G^{-1}\Phi(t,t_0)G\bar{\xi}_0 \ . \end{aligned} \tag{2.42}$$

Consequently, equation (2.42) yields the following relation

$$\Phi(\tau, t_0) = G^{-1}\Phi(t, t_0)G \ , \tag{2.43}$$

denoted here as the time-invariance property of the state transition matrix. The relationship in equation (2.43) satisfies all the differential equations corresponding to the linear system. This is easily verified, after some matrix manipulation, by substituting equations (2.43) and (2.40) into the matrix differential equation (2.19). Note that, since $\Phi(t_0, t_0) = I_n$ and $\Phi(t_0, t)\Phi(t, t_0) = \Phi(t_0, t_0)$, the state transition matrix is related to its inverse by

$$\Phi(t, t_0) = \Phi(t_0, t)^{-1} \ . \tag{2.44}$$

Equations (2.43) and (2.44) are true in general for all t given any t_0. Since the system is time-invariant, consider the case $t_0 = 0$. Without loss of generality, let t correspond to one period of the motion, that is, $t = T$. Then, equation (2.43) states that

$$\Phi(-T, 0) = G^{-1}\Phi(T, 0)G \ . \tag{2.45}$$

Also note that, $\Phi(-T, 0) = \Phi(0, T)$ and hence, from equation (2.44), $\Phi(-T, 0) = \Phi(T, 0)^{-1}$. Thus, equation (2.45) can be rewritten as

$$\Phi(T, 0) = G\Phi(T, 0)^{-1}G^{-1} \ . \tag{2.46}$$

Since G is a constant nonsingular matrix, equation (2.46) suggests that $\Phi(T, 0)$ is similar to $\Phi(T, 0)^{-1}$. Thus, both matrices share the same eigenvalues. This suggests that the structure of the eigenvalues is not arbitrary, as established by the following theorem from Yakubovich and Starzhinskii [39].

Theorem 2.6 *(Lyapunov's Theorem) If λ is an eigenvalue of the monodromy matrix $\Phi(T, 0)$ of a t-invariant system, then λ^{-1} is also an eigenvalue, with the same structure of elementary divisors.*

The geometry of the stable and unstable subspaces is determined by the structure of the eigenvalues established in Theorem (2.6) and the time-invariance properties in equations (2.45)-(2.46). This fact will become apparent when the symmetry properties between the stable and unstable manifolds are discussed.

2.3.7 Eigenvalue Structure of the Monodromy Matrix

As established by Lyapunov's Theorem (2.6), the eigenvalues of the monodromy matrix corresponding to a time-invariant system must appear in reciprocal pairs. Also, since $\Phi(T,0)$ is a real matrix, the characteristic multipliers must either be real or appear in complex conjugate pairs. However, in general, complex conjugate pairs are not reciprocal pairs. This suggests that the eigenvalues of $\Phi(T,0)$ can only exist in predetermined configurations in the complex plane.

In general, for a periodic orbit to exist, at least one eigenvalue of $\Phi(T,0)$ must equal one. However, in the CR3BP, for a periodic orbit to exist a minimum of two eigenvalues must equal one, because of their reciprocal nature. This fact implies that isolated periodic orbits cannot exist in the CR3BP. Let the eigenvalues at one be denoted λ_1 and λ_2. Suppose λ_3 and λ_4 are both real while λ_5 and λ_6 are complex conjugates. From Lyapunov's Theorem (2.6), it is clear that $\lambda_3 = 1/\lambda_4$. Hence, if $\lambda_5 = a + bi$ then, for λ_5 and λ_6 to be both reciprocals and a complex conjugate pair, the modulus of the complex conjugate pair must be equal to one ($a^2 + b^2 = 1$). Thus, the complex conjugate pair lies on the unit circle as illustrated in Figure 2.12a.

Consider the case when λ_3, λ_4, λ_5, and λ_6 are complex, $\lambda_3 = \lambda_4^*$ and $\lambda_5 = \lambda_6^*$, where the superscript [*] denotes the complex conjugate. Recall, Lyapunov's Theorem stipulates that the characteristic multipliers exist in reciprocal pairs; it does not require that reciprocal pairs also be complex conjugate pairs. However, both of these conditions must still hold true for the remaining four eigenvalues. Clearly, both conditions are satisfied if all the eigenvalues lie on the unit circle. The only other possible structure is depicted in Figure 2.12c. Here, the eigenvalues split off the unit circle and are symmetrically arranged with respect to the real axis and the unit circle.

2.3.8 Stable/Unstable Manifolds and the Associated Symmetries

In a nonlinear system, only the instability of a periodic orbit can be determined from linear analysis. That is, if any of the characteristic multipliers have modulus greater than unity, the periodic solution, Γ, is unstable. In the Sun-Jupiter-comet system, halo orbits in the vicinity of L_1 and L_2, with $A_z < 30 \times 10^6$ km, are unstable

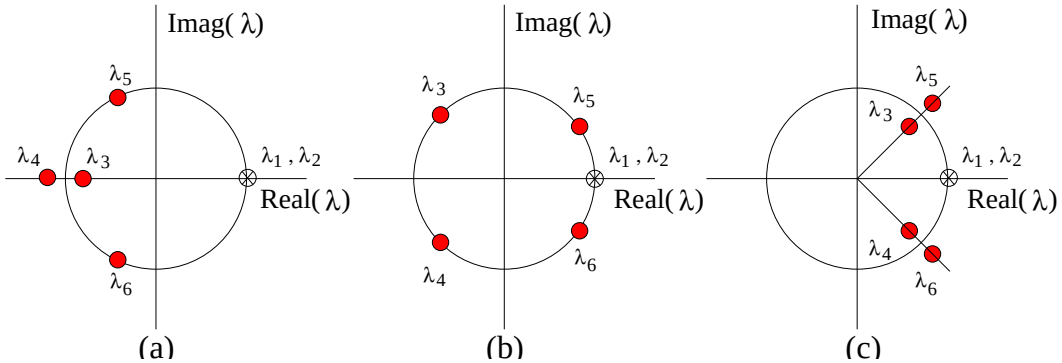

Figure 2.12. Eigenvalue Structure

with a four-dimensional center manifold and one-dimensional stable and unstable manifolds. Linear stability analysis can also provide further insight into the geometry of the stable and unstable manifolds associated with this subset in the SJL1 and SJL2 halo families. Let Γ denote a halo orbit of period T and note that any state, $\bar{x}(t)$, along Γ can represent the orbit as a fixed point, $\bar{x}^*$, in a Poincaré map.

As previously stated, the monodromy matrix associated with $\bar{x}^*$, $\Phi(T,0)$, has two real eigenvalues that do not equal unity, one stable, λ_s, and one unstable, λ_u, such that $\lambda_u = 1/\lambda_s$. Let $\bar{v}_s(\bar{x}^*)$ and $\bar{v}_u(\bar{x}^*)$ denote the corresponding stable and unstable eigenvectors. Then, the eigenvalue problem is stated as follows,

$$\Phi(T,0)\bar{v}_s(\bar{x}^*) = \lambda_s \bar{v}_s(\bar{x}^*) \ , \tag{2.47}$$

$$\Phi(T,0)\bar{v}_u(\bar{x}^*) = \lambda_u \bar{v}_u(\bar{x}^*) \ . \tag{2.48}$$

The six-dimensional vectors $\bar{v}_s(\bar{x}^*)$ and $\bar{v}_u(\bar{x}^*)$ satisfy equations (2.47)-(2.48) and span the stable and unstable subspaces of $\bar{x}^*$. Hence, the stable and unstable manifolds associated with $\bar{x}^*$ can be numerically determined by propagating initial states that are computed by perturbing the state at $\bar{x}^*$ along $\bar{v}_s(\bar{x}^*)$ and $\bar{v}_u(\bar{x}^*)$, respectively. The resulting trajectories lie on the stable and unstable manifolds of Γ but do not completely represent the motion on $W^s(\Gamma)$ and $W^u(\Gamma)$. A phase portrait of $W^s(\Gamma)$ is represented by a collection of trajectories that describe the flow along the stable manifold associated with Γ. For instance, consider a discrete set of N states, $\bar{x}_j^* = \bar{x}(j\Delta t)$, along Γ that are measured at equally spaced time intervals (Δt), where

$\Delta t = T/N$. The construction of a phase portrait for $W^s(\Gamma)$ is accomplished in one of two ways. One approach requires that the monodromy matrix associated with each $\bar{x}_j^*$ $(j = 0, \ldots, N-1)$ be determined numerically. Note that the N^{th} state is not included in the sample since $\bar{x}_0^* = \bar{x}_N^*$. Then, the stable and unstable eigenvectors associated with each fixed point $\bar{x}_j^*$, $\bar{v}_s(\bar{x}_j^*)$ and $\bar{v}_u(\bar{x}_j^*)$, are computed. Alternatively, a single integration is performed to obtain the monodromy matrix associated with $\bar{x}_0^*$, through equation (2.19), and the corresponding stable and unstable eigenvectors, $\bar{v}_s(\bar{x}_0^*) = \bar{Y}^{W_s}(0)$ and $\bar{v}_u(\bar{x}_0^*) = \bar{Y}^{W_u}(0)$, are computed. Then, the stable and unstable eigenvectors associated with all other sample states, $\bar{Y}^{W_s}(j\Delta t)$ and $\bar{Y}^{W_u}(j\Delta t)$, are determined by mapping $\bar{Y}^{W_s}(0)$ and $\bar{Y}^{W_u}(0)$ from $\bar{x}_0^*$ to $\bar{x}_j^*$ via the state transition matrix as follows

$$\bar{Y}^{W_s}(j\Delta t) = \Phi(j\Delta t, 0)\bar{Y}^{W_s}(0) \ , \tag{2.49}$$

$$\bar{Y}^{W_u}(j\Delta t) = \Phi(j\Delta t, 0)\bar{Y}^{W_u}(0) \ . \tag{2.50}$$

In either approach, the phase portrait corresponding to $W^s(\Gamma)$ is formed by numerically integrating, in negative time ($\Delta t < 0$), initial state vectors in the stable subspace, $E^s(\bar{x}_j^*)$, associated with each sample state, $\bar{x}_j^*$. For the unstable manifold, $W^u(\Gamma)$, the initial states in the unstable subspace $E^u(\bar{x}_j^*)$, are integrated forward, $\Delta t > 0$. The geometry of the flow is unaffected by the method that is selected to compute the stable and unstable eigenvector directions.

A comparison of the phase portrait of $W^s(\Gamma)$ to that of $W^u(\Gamma)$ reveals a natural symmetry between the flows along the stable and unstable manifolds. This symmetry is rooted in the time-invariance properties of the state transition matrix. Consider, the statement of the eigenvalue problem in equations (2.47)-(2.48) but for $\Delta t < 0$

$$\Phi(-T, 0)\bar{v}_s'(\bar{z}^*) = \lambda_s \bar{v}_s'(\bar{z}^*) \ , \tag{2.51}$$

$$\Phi(-T, 0)\bar{v}_u'(\bar{z}^*) = \lambda_u \bar{v}_u'(\bar{z}^*) \ . \tag{2.52}$$

where $\bar{v}_s'(\bar{z}^*)$ and $\bar{v}_u'(\bar{z}^*)$ are the stable and unstable eigenvectors associated with $\bar{z}^* = G\bar{x}^*$ and the prime notation indicates integration such that $\Delta t < 0$. Substitution

of equation (2.45) into (2.51) and (2.52) yields

$$\Phi(T,0)G\bar{v}_s'(\bar{z}^*) = \lambda_s G\bar{v}_s'(\bar{z}^*) \ , \tag{2.53}$$

$$\Phi(T,0)G\bar{v}_u'(\bar{z}^*) = \lambda_u G\bar{v}_u'(\bar{z}^*) \ . \tag{2.54}$$

Hence, the stable and unstable eigenvectors associated with $\bar{x}^*$ for $\Delta t > 0$, $\bar{v}_s(\bar{x}^*)$ and $\bar{v}_u(\bar{x}^*)$, are related to the eigenvectors associated with $\bar{z}^*$ corresponding to $\Delta t < 0$, $\bar{v}_s'(\bar{z}^*)$ and $\bar{v}_u'(\bar{z}^*)$, through the constant matrix G as follows

$$\bar{v}_s(\bar{x}^*) = G\bar{v}_s'(\bar{z}^*) \ , \tag{2.55}$$

$$\bar{v}_u(\bar{x}^*) = G\bar{v}_u'(\bar{z}^*) \ . \tag{2.56}$$

The results presented in equations (2.55)-(2.56) are applicable for any fixed point $\bar{x}_j^*$ along Γ. For the stable manifold, this is easily verified by direct application of equations (2.55) and (2.45) to the mapping in equation (2.49) where $\bar{Y}^{W_s}(0), = \bar{v}_s(\bar{x}_0^*)$.

$$\begin{aligned}
\bar{Y}^{W_s}(j\Delta t) &= \Phi(j\Delta t,0)\bar{v}_s(\bar{x}_0^*) \ , \\
&= \Phi(j\Delta t,0)G\bar{v}_s'(\bar{z}_0^*) \ , \\
&= G\left[G^{-1}\Phi(j\Delta t,0)G\bar{v}_s'(\bar{z}_0^*)\right] \ , \\
&= G\left[\Phi(-j\Delta t,0)\bar{v}_s'(\bar{z}_0^*)\right] \ , \\
&= G\bar{Y}^{W_s'}(-j\Delta t) \ .
\end{aligned}$$

A similar relationship exists for the unstable eigenvector, $\bar{Y}^{W_u}(j\Delta t)$, associated with $\bar{x}_j^*$ along the periodic orbit. The normalized set of equations in terms of unit eigenvectors is represented by

$$\begin{aligned}
\hat{Y}^{W_s}(j\Delta t) &= G\hat{Y}^{W_s'}(-j\Delta t) \ , \\
\hat{Y}^{W_u}(j\Delta t) &= G\hat{Y}^{W_u'}(-j\Delta t) \ .
\end{aligned} \tag{2.57}$$

Note that, $\bar{Y}^{W_s'}(j\Delta t)$ and $\bar{Y}^{W_u'}(j\Delta t)$ are associated with $\bar{z}_j^*$, not with $\bar{x}_j^*$. However, it is possible to identify an expression relating the stable eigenvector $\bar{v}_s(\bar{x}_j^*)$ to the

unstable eigenvector $\bar{v}'_u(\bar{x}^*_j)$ by inverting equations (2.47) and (2.48). For example,

$$\begin{aligned}
\Phi(T,0)\bar{v}_s(\bar{x}^*_j) &= \lambda_s\bar{v}_s(\bar{x}^*_j) \ , \\
\frac{1}{\lambda_s}\bar{v}_s(\bar{x}^*_j) &= \Phi^{-1}(T,0)\bar{v}_s(\bar{x}^*_j) \ , \\
\lambda_u\bar{v}_s(\bar{x}^*_j) &= \Phi(0,T)\bar{v}_s(\bar{x}^*_j) \ , \\
\lambda_u\bar{v}_s(\bar{x}^*_j) &= \Phi(-T,0)\bar{v}_s(\bar{x}^*_j) \ . \qquad (2.58)
\end{aligned}$$

Comparison of equation (2.58) to the statement of the eigenvalue problem, for $\Delta t < 0$, and associated with $\bar{x}^*_j$,

$$\lambda_u\bar{v}'_u(\bar{x}^*_j) = \Phi(-T,0)\bar{v}'_u(\bar{x}^*_j) \ , \qquad (2.59)$$

results in the following relationship between the stable and unstable eigenvector directions under time reversal

$$\begin{aligned}
\bar{v}^s(\bar{x}^*_j) &= \bar{v}'_u(\bar{x}^*_j) \ , \qquad (2.60) \\
\bar{v}^u(\bar{x}^*_j) &= \bar{v}'_s(\bar{x}^*_j) \ . \qquad (2.61)
\end{aligned}$$

That is, in negative time, a state on $E^{u'}(\bar{x}^*_j)$ asymptotically departs $\bar{x}^*_j$ with each iteration of the map, $\Phi(-T,0)$. However, in real time, $\Delta t > 0$ and, as a result, states on $E^{u'}(\bar{x}^*_j)$ asymptotically approach $\bar{x}^*_j$ for $\Delta t > 0$. In essence, the unstable eigenvector for $\Delta t < 0$ is also the stable eigenvector for $\Delta t > 0$. A similar statement is applicable to the stable eigenvector for $\Delta t < 0$. This results extends to $W^s(\Gamma)$ and $W^u(\Gamma)$. That is, $W^{s'}(\Gamma) = W^u(\Gamma)$ and $W^{u'}(\Gamma) = W^s(\Gamma)$. Since equations (2.60)-(2.61) are true for all $\bar{x}^*$, substitution into equations (2.55)-(2.56) results in

$$\begin{aligned}
\bar{v}_s(\bar{x}^*) &= G\bar{v}_u(\bar{z}^*) \ , \qquad (2.62) \\
\bar{v}_u(\bar{x}^*) &= G\bar{v}_s(\bar{z}^*) \ . \qquad (2.63)
\end{aligned}$$

The implications of equations (2.62)-(2.63) are easily visualized when applied to simply symmetric periodic solutions, such as halo orbits. In configuration space, a halo orbit is symmetric about the xz-plane. Thus, if G is the constant matrix defined in equation (2.41) and $\bar{x}^*_j = \bar{x}(j\Delta t) = [x \ y \ z \ \dot{x} \ \dot{y} \ \dot{z}]^T$ represents a state along the

halo orbit, then $\bar{z}_j^* = \bar{x}(T - j\Delta t) = [x \ -y \ z \ -\dot{x} \ \dot{y} \ -\dot{z}]^T$ also represents a state on the same orbit. Now, suppose that equations (2.10)-(2.12) as well as (2.19) are numerically integrated with $\Delta t < 0$ and initial conditions $\bar{x}_0^*$, corresponding to the maximum xz-plane crossing along the periodic solution Γ. The statement in equations (2.62)-(2.63) implies that the xz-plane symmetry also applies to the stable eigenvector associated with $\bar{x}(j\Delta t)$ and the unstable eigenvector corresponding to $\bar{x}(T-j\Delta t)$. Let $\bar{Y}^{W_s}(j\Delta t) = [\bar{v}_s^{(pos)}\bar{v}_s^{(vel)}]^T$ and $\bar{Y}^{W_u}(j\Delta t) = [\bar{v}_u^{(pos)}\bar{v}_u^{(vel)}]^T$ where $\bar{v}_s^{(pos)}$ and $\bar{v}_u^{(pos)}$ denote three-dimensional vectors whose components coincide with the position elements of $\bar{Y}^{W_s}(j\Delta t)$ and $\bar{Y}^{W_u}(j\Delta t)$, respectively. Similarly, the elements of $\bar{v}_s^{(vel)}$ and $\bar{v}_u^{(vel)}$ correspond to the velocity elements of the stable and unstable eigenvectors. Then, as stated in equations (2.62)-(2.63), given any two fixed points, $\bar{x}_1^*$ and $\bar{x}_2^*$, mirrored across the xz-plane on Γ, the position elements corresponding to the stable/unstable eigenvector associated with $\bar{x}_1^*$ are also the elements of the unstable/stable eigenvector corresponding to $\bar{x}_2^*$, but the y components are of opposite sign. Furthermore, the velocity components are also the same in magnitude, but the $\dot{x}$ and $\dot{z}$ velocity elements are of opposite sign. This is illustrated in Figure 2.13 for a state at the the maximum xz-plane crossing along an L_2 northern halo orbit, and in Figure 2.14 for two states mirrored about the xz-plane on the same orbit. Note that the data represented in Figures 2.13 and 2.14 is centered at L_2. If $\tau = -t$ and $\bar{z}(\tau) = G\bar{x}(t)$ is substituted into the nonlinear equations (2.10)-(2.12), it is apparent that the xz-plane symmetry extends to the global stable and unstable manifolds associated with $\bar{x}(j\Delta t)$ and $\bar{x}(T - j\Delta t)$. For the states, $\bar{x}_1^*$ and $\bar{x}_2^*$, in Figure 2.14, an arc along a trajectory that lies on the stable manifold, associated with $\bar{x}_1^*$, and an arc on the unstable manifold, corresponding to $\bar{x}_2^*$, are illustrated in Figure 2.15 in terms of Joviocentric rotating coordinates in the CR3BP.

2.3.9 Computation of the Global Stable/Unstable Manifold

Computation of the global stable and unstable manifolds associated with $\bar{x}^* = \bar{x}(t_i)$ relies on the availability of initial conditions that lie in the subspaces $E^s(\bar{x}^*)$ and $E^u(\bar{x}^*)$. An estimate of these conditions is determined through a perturbation

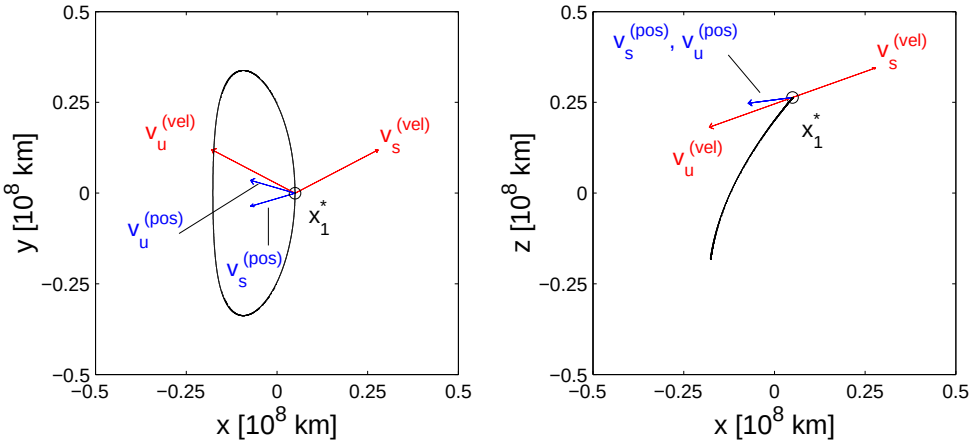

Figure 2.13. Stable/Unstable Eigenvector Symmetry at Maximum xz-Plane Crossing

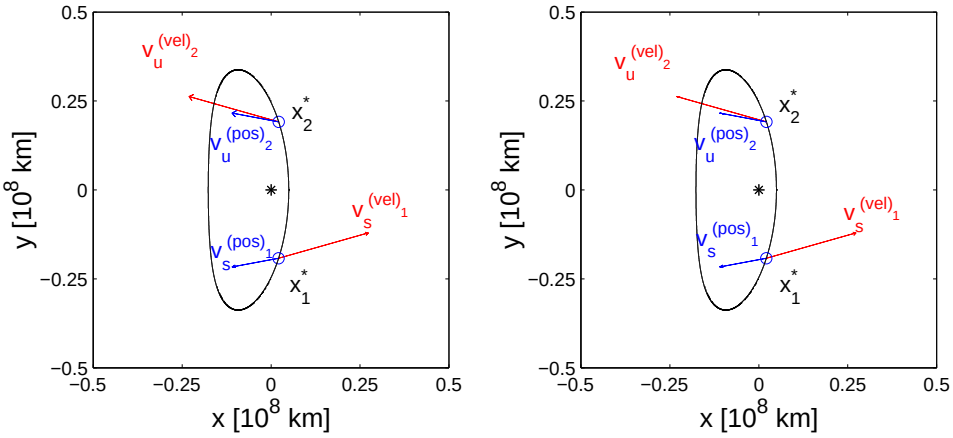

Figure 2.14. Stable/Unstable Eigenvector Symmetry for States Mirrored Across the xz-Plane

to the state at any fixed point, $\bar{x}^* = \bar{x}(t_i)$, along the periodic orbit, by some small scale factor (d), along the stable or unstable directions associated with $\bar{x}^*$. Suppose $\hat{Y}^{W_s}(t_i) = [x_s \; y_s \; z_s \; \dot{x}_s \; \dot{y}_s \; \dot{z}_s]^T$ and $\hat{Y}^{W_u}(t_i) = [x_u \; y_u \; z_u \; \dot{x}_u \; \dot{y}_u \; \dot{z}_u]^T$. Let $\bar{V}^{W_s}(t_i)$ and $\bar{V}^{W_u}(t_i)$ be defined as

$$\bar{V}^{W_s}(t_i) = \frac{\hat{Y}^{W_s}(t_i)}{\sqrt{x_s^2 + y_s^2 + z_s^2}} \; , \tag{2.64}$$

$$\bar{V}^{W_u}(t_i) = \frac{\hat{Y}^{W_u}(t_i)}{\sqrt{x_u^2 + y_u^2 + z_u^2}} \; , \tag{2.65}$$

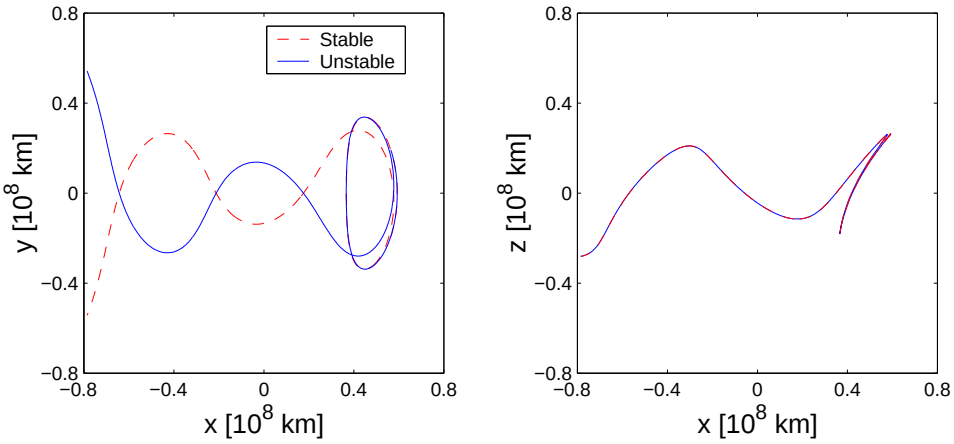

Figure 2.15. Stable/Unstable Manifold Symmetry
for States Mirrored Across the xz-Plane

and

$$\bar{X}_s = \bar{x}(t_i) + d \cdot \bar{V}^{W_s}(t_i) \ , \tag{2.66}$$

$$\bar{X}_u = \bar{x}(t_i) + d \cdot \bar{V}^{W_u}(t_i) \ . \tag{2.67}$$

The global stable manifold (W^s) is approximated by numerically integrating $\bar{X}_s$ for $\Delta t \leq 0$, where $\bar{X}_s$ is defined by equation (2.66). Similarly, the global unstable manifold (W^u) is estimated by numerically integrating $\bar{X}_u$ for $\Delta t \geq 0$, where $\bar{X}_u$ is defined in equation (2.67).

For application to the Sun-Jupiter system, a value of $d = 1000$ km is appropriate. This value is small enough to preserve the accuracy of the linear estimate, yet it allows for reasonable integration times. For instance, recall that trajectories on the stable manifold asymptotically approach the halo orbit as $t \to \infty$. The magnitude of d determines the length of time required for trajectories on $W^s(\Gamma)$ to leave the immediate vicinity of the orbit as $t \to -\infty$. If d is too small, the integration time required for trajectories to encounter Jupiter increases; consequently, the accuracy of the solution degrades. Other values within a reasonable range of $d = 1000$ km are acceptable as well. Given the limits of a numerical procedure, the "linear" range of d is defined such that, when propagated with $\Delta t > 0$, initial states along $E^s(\bar{x}^*)$ result in trajectories that resemble the associated halo orbit and complete at least

two revolutions. Naturally, the stable and unstable manifolds are theoretical surfaces in $\mathbb{R}^n$ and, in practice, solutions initiated in the stable subspace with $\Delta t > 0$, or in E^u with $\Delta t < 0$, eventually diverge from the periodic solution due to integration errors.

Recall, from the discussion on equilibrium points, that the local stable and unstable manifolds are formed by the union of two half-manifolds. A similar definition is applicable for the stable and unstable manifolds associated with the fixed points of a map. The local stable manifold, $W^s_{loc}(\bar{x}^*)$, is formed by the union of $W^{s+}_{loc}(\bar{x}^*)$ and $W^{s-}_{loc}(\bar{x}^*)$. In this study, the symbol $W^{s+}_{loc}(\bar{x}^*)$ is defined such that solutions in $W^{s+}_{loc}(\bar{x}^*)$, for some state $\bar{x}^*$ along Γ, depart the periodic orbit and evolve towards the vicinity of Jupiter, that is, the capture region. For an L_1 halo orbit, trajectories in $W^{s-}_{loc}(\bar{x}^*)$ shift towards the interior region of the corresponding zero-velocity surface. Conversely, for an L_2 halo orbit, trajectory arcs along $W^{s-}_{loc}(\bar{x}^*)$ immediately depart the vicinity of Jupiter and approach the exterior region of the associated zero-velocity surface. Thus, given initial conditions from equations (2.66) and (2.67), a numerically integrated path evolves along $W^{s/u+}_{loc}(\bar{x}^*)$ or $W^{s/u-}_{loc}(\bar{x}^*)$; the sign of d is selected to specify one of these particular segments along $W^{s/u}_{loc}$. The trajectories that appear in Figure 2.15 represent the stable and unstable manifolds and correspond to $d = 1000$ km.

2.3.10 Heteroclinic and Homoclinic Trajectories

The intersection of the stable and unstable manifolds corresponding to an unstable fixed point ($\bar{x}^*$) in phase space, is the union of all the trajectories that approach the fixed point $\bar{x}^*$ both in positive time ($\Delta t \geq 0$) and negative time ($\Delta t \leq 0$). A trajectory Γ that lies on $W^s(\bar{x}^*) \cap W^u(\bar{x}^*)$ is called a homoclinic trajectory. An example of a homoclinic trajectory for a second order system is illustrated in Figure 2.16a. Now, let $\bar{x}^*_1$ and $\bar{x}^*_2$ be two distinct non-stable fixed points. A trajectory Γ_1 that lies on $W^u(\bar{x}^*_1) \cap W^s(\bar{x}^*_2)$ or a trajectory Γ_2 that lies in $W^s(\bar{x}^*_1) \cap W^u(\bar{x}^*_2)$ is called a heteroclinic trajectory. Figure 2.16b depicts a sample heteroclinic trajectory for a second order system. As discussed in the following chapter, the concept of homoclinic

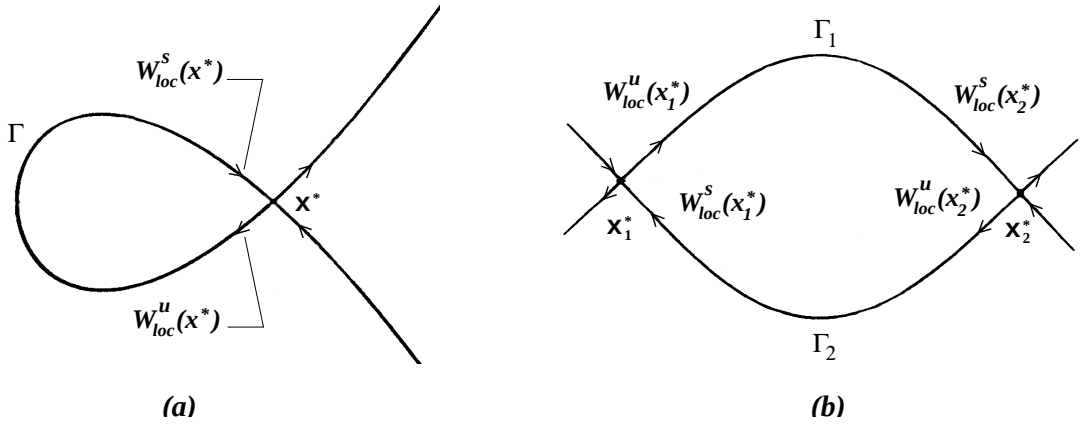

Figure 2.16. Homoclinic and Heteroclinic Trajectories – Adapted from Perko [32]

and heteroclinic trajectories has important applications in the mathematical modeling of TSC in the CR3BP.

2.3.11 Transition of the Solutions to the Ephemeris Model

In configuration space, the paths of Oterma and Helin-Roman-Crockett, that are available from ephemeris information, exhibit features that are geometrically similar to those representing the path of a particle evolving along the stable or unstable manifolds associated with members of the SJL1 and SJL2 halo families. A "position match" is defined as a segment of a trajectory arc that lies on either the stable or unstable manifold, resembles the capture geometry in the vicinity of Jupiter, and flows in the same direction as the known path of the comet. The goal of this study is the identification of a match in both position and velocity for Oterma and Helin-Roman-Crockett. Although the circular restricted model yields solutions that resemble the path of the comet in configuration space, numerical analysis suggests that the assumption of circular primary motion is too restrictive when a match of the velocity states is sought as well. To improve the accuracy of an existing match, the solution identified in the CR3BP is transitioned to the ephemeris model.

In the "ephemeris" model, as defined here, primary motion is specified from planetary state information available from the Jet Propulsion Laboratory DE405 ephemeris. The comet trajectories are also generated from the DE405 ephemeris. The mathematical model is consistent with the equations of relative motion (A.E.

Roy [40]), where the comet is the particle of interest, the Sun represents the central body for integration, and Jupiter is defined as the perturbing gravitational field. All measure numbers in the equations of motion are associated with the inertial reference frame. For this analysis, the inertial XY-plane is defined as the plane of the Earth Mean Equator and the X-axis is directed along the vernal equinox (J2000) direction. Although the equations of motion are expressed in terms of measure numbers associated with the inertial reference frame, the comparison between the numerically integrated trajectory and the available cometary ephemeris is performed in the rotating frame to better assess the impact of the model. Since no assumptions about the motion of the primaries is enforced, the transformation from inertial to rotating coordinates is based on the instantaneous position of the primaries, as determined from the available ephemeris information. That is, although the definition of the rotating frame remains unchanged, the unit vectors $\hat{x}$, $\hat{y}$, and $\hat{z}$ are re-evaluated at each epoch. The details of this coordinate transformation are outlined in Wilson [41].

In the CR3BP, a position match corresponds to an arc along a trajectory that represents a solution on a stable or unstable manifold that is associated with a particular reference solution, $\bar{x}_{ref}$. The reference solutions of interest here are periodic halo orbits. Since the stable and unstable manifolds are, by definition, associated with a reference solution, the transition to the ephemeris model requires a new reference solution and recomputation of the stable/unstable manifolds for the region of interest. Ultimately, the goal is an arc that preserves the overall geometry of the existing match (identified in the CR3BP) and minimizes the difference between the ephemeris state associated with the comet and the state determined from the numerically integrated solution. To preserve the geometrical features of the existing match, it is possible to identify a reference solution, in the ephemeris model, that resembles the halo orbit in the CR3BP. The simplest approach, one that ensures preservation of the essential features, is the use of the reference solution from the CR3BP as the initial guess to a differential corrections process. A two-level differential corrector, developed by Howell and Pernicka [42], is implemented to compute a Lissajous tra-

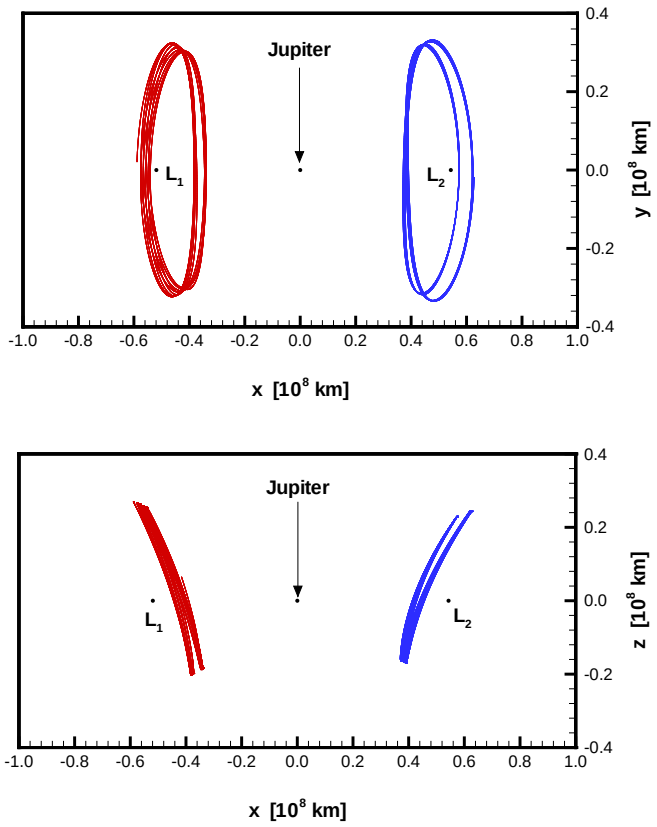

Figure 2.17. Lissajous Trajectories

jectory in the ephemeris model that resembles, in this case, the original halo orbit, as illustrated in Figure 2.17. Alternatively, the Richardson and Cary [25] approximation is also available for the computation of quasi-periodic trajectories. However, as is true for any approximation, the range of validity is limited. As previously discussed, the halo orbits of interest possess an out-of-plane amplitude near 30×10^6 km. Although it is still possible to obtain an initial guess for the differential corrector, based on the Richardson and Cary approximation, the parameters that typically result in a "halo-type" orbit do not yield a Lissajous trajectory that resembles a halo. This approximation is better suited for A_z amplitudes under $200,000$ km.

Quasi-periodic motion is, essentially, a mixture of different, incommensurate, fundamental frequencies. Thus, a Lissajous trajectory, though not periodic, is bounded and exists on an n-D torus. Of course, as defined, stable and unstable manifolds

are associated with periodic orbits; the advantages of periodicity no longer exist for quasi-periodic solutions. However, numerically, it is possible to identify solutions that exhibit the features characteristic of stable and unstable manifold flow. Furthermore, although the classical method for globalizing the stable and unstable manifolds for periodic orbits does not explicitly extend to quasi-periodic motion, in practice, some of the numerical concepts can be successfully adapted to produce results (Gómez, et al. [27], Howell and Barden [32]) to an acceptable degree of accuracy. Ultimately, computation of trajectories that represent motion on the "stable" or "unstable" manifold associated with a quasi-periodic orbit still requires an approximation of the initial state.

For periodic orbits, the initial conditions to globalize the manifolds are approximated by perturbing a six-dimensional state on the periodic orbit and shifting it into the corresponding stable or unstable subspace. The stable and unstable eigenvectors of the monodromy matrix span these linear subspaces. Hence, initial states are straightforward to generate and the stable and unstable manifolds for periodic orbits are relatively simple to globalize, unlike their quasi-periodic counterparts. Quasi-periodic solutions have, in essence, an infinite period. However, since the orbit is not periodic, within reasonable time intervals, the stability analysis based on Floquet theory is not applicable. Even if the orbit is assumed to be nearly periodic with period $\tilde{T}$, the corresponding monodromy matrix is ill-conditioned; the columns of the STM become unbounded in magnitude as time increases. Hence, conventional methods for the solution of the eigenvalue/eigenvector problem are rendered useless for large $\tilde{T}$. However, numerical analysis [32] suggests that, in the ephemeris model, a periodicity assumption is still a viable option, assuming that $\tilde{T}$ is not excessively large and that the initial and final states are sufficiently close. Howell and Barden [32] successfully approximate the stable and unstable "eigenvectors" associated with quasi-periodic solutions through this approach. The goal is a relatively short pseudo-period $\tilde{T}$, and minimization of the difference between the initial and final states. According to Howell and Barden, the periodicity assumption in the methodology produces the best

results when a "period" encompasses two revolutions on the orbit. That is, if $\bar{x}_0$ denotes the initial state and $\bar{x}_f$ denotes the state at the end of the second revolution, then $\tilde{T} = t_f - t_0$. The robustness of this assumption is rooted in the relative location of the bodies every $\tilde{T}$ time units. Specifically, in the time it takes P_3 to complete two revolutions along the orbit, P_2 completes roughly one revolution around P_1. This particular configuration minimizes the error between the initial and final states used to define a period along the Lissajous trajectory. The stable and unstable eigenvectors associated with the corresponding monodromy matrix are then utilized to approximate the eigenvectors at other locations along the orbit via the state transition matrix.

It is necessary to note that the accuracy of the eigenvector propagation decays towards the end of the first revolution because the orbit is not truly periodic. Also, for the purpose of estimating $\tilde{T}$, the determination of the end of the second revolution is somewhat arbitrary; therefore, the computation of the stable and unstable directions is affected by the definition of the period. To accurately compute the eigenvectors along the second revolution, the period is redefined to consider the desired revolution as the first of a sequence of two revolutions. The disadvantage of this method is a small discontinuity that exists at the shift point between revolutions since the definition of the period changes accordingly. This discontinuity can be avoided by considering an alternative approach, that is the power method (Gomez et al. [27]).

The power method takes advantage of the properties of the STM to compute the stable and unstable eigendirections along the trajectory. An additional advantage of the power method over the standard approach is the lack of any dependence on a "period" so it is not necessary to explicitly define one. To discuss the basis of this approach consider, once again, a periodic orbit. As previously stated, the stability of a periodic orbit is determined by the modulus of the characteristic multipliers, λ_j. That is, the eigenvalues of the monodromy matrix associated with the fixed point, $\bar{x}^*$, that represents the orbit in a Poincaré map. The growth of any initial perturbation,

$\bar{y}(0)$, over an integer multiple of the period, is governed by

$$\begin{aligned} \bar{y}(nT) &= \Phi(nT,0)\bar{y}(0) \\ &= \sum_{j=1}^{6} c_j \lambda_j^{(n)} \bar{v}^{(j)} \ , \end{aligned} \tag{2.68}$$

where $\bar{v}^{(j)}$ represents the eigenvector corresponding to λ_j. If at least one eigenvalue $\|\lambda_j\| > 1$, then, with every revolution, nearly every perturbation lies in the unstable subspace. That is, the columns of the state transition matrix align with the unstable subspace as $t \to \infty$. For the halo orbits of interest, $\|\lambda_j\| \gg 1$. Hence, this alignment occurs within the first revolution along the orbit. The power method exploits this natural alignment to compute vectors along the stable and unstable subspaces of the orbit.

A Lissajous orbit appears as an invariant curve on a Poincaré map, not a fixed point. However, for the purpose of estimating the stable and unstable directions, consider $\bar{x}^*$ as the state that defines the end of the desired number of revolutions along the Lissajous trajectory. Let the initial state along the orbit be defined by the position and velocity vectors $\bar{r}_0$ and $\bar{v}_0$, respectively. Define the crossing plane $\hat{b}_1 - \hat{b}_2$ such that

$$\hat{b}_1 = \frac{\bar{r}_0}{\|\bar{r}_0\|} \tag{2.69}$$

$$\hat{b}_3 = \frac{\bar{r}_0 \times \bar{v}_0}{\|\bar{r}_0 \times \bar{v}_0\|} \tag{2.70}$$

$$\hat{b}_2 = \hat{b}_3 \times \hat{b}_1 \tag{2.71}$$

The states along the orbit that intersect the crossing plane define consecutive revolutions. An enlarged view of each crossing is illustrated in Figure 2.18. The initial state is denoted as "0" and defines the crossing plane. Figure 2.18 depicts a total of n crossings. Consider now the computation of the unstable direction at any point along a Lissajous trajectory with n revolutions. Let $\bar{v}_u(\bar{x}_0^*)$ represent a six-dimensional vector aligned with some arbitrary initial perturbation. Recall, from equation (2.18),

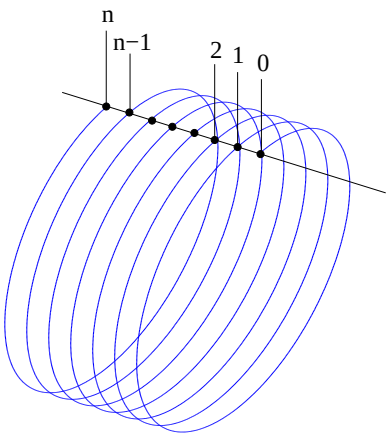

Figure 2.18. Revolutions Along a Lissajous Trajectory

that this vector can be mapped to $\bar{x}_n^*$ through the state transition matrix as follows

$$\begin{aligned} \bar{v}_u(\bar{x}_n^*) &= \Phi(t_n, t_0)\bar{v}_u(\bar{x}_0^*) \ , \\ &= \Phi(t_n, t_{n-1})\Phi(t_{n-1}, t_{n-2}) \cdots \Phi(t_2, t_1)\Phi(t_1, t_0)\bar{v}_u(\bar{x}_0^*) \ . \end{aligned} \tag{2.72}$$

Let $\bar{v}_u(\bar{x}_j^*) = \Phi(t_j, t_{j-1})\bar{v}_u(\bar{x}_{j-1}^*)$, such that equation (2.72) can be restated in terms of a set of n equations, one for each revolution along the orbit ($j = 1, \ldots, n$). To avoid numerical overflow, the state transition matrix, $\Phi(t_j, t_{j-1})$, is reinitialized to the identity matrix at the commencement of each revolution, during the numerical integration process. That is, $\Phi(t_j, t_j) = I_6$ ($j = 0, \ldots, n-1$). Furthermore, $\bar{v}_u(\bar{x}_j^*)$ is normalized for all j such that $\tilde{u}_u(\bar{x}_j^*) = \bar{v}_u(\bar{x}_j^*)/\|\bar{v}_u(\bar{x}_j^*)\|$ to yield to following set of equations,

$$\begin{aligned} \bar{v}_u^{(k)}(\bar{x}_1^*) &= \Phi(t_1, t_0)\tilde{u}_u^{(k)}(\bar{x}_0^*) \ , \\ \bar{v}_u^{(k)}(\bar{x}_2^*) &= \Phi(t_2, t_1)\tilde{u}_u^{(k)}(\bar{x}_1^*) \ , \\ &\vdots \\ \bar{v}_u^{(k)}(\bar{x}_n^*) &= \Phi(t_n, t_{n-1})\tilde{u}_u^{(k)}(\bar{x}_{n-1}^*) \ . \end{aligned} \tag{2.73}$$

Since the columns of the state transition matrix become aligned with the unstable direction within one revolution, the system of equations (2.73) can be solved iteratively to determine all the vectors $\bar{v}_u(\bar{x}_j^*)$. In equation (2.73), the superscript k denotes

the k^{th} iteration. This iteration is based on the assumption that $\bar{v}_u(\bar{x}_n^*) = \bar{v}_u(\bar{x}_0^*)$, hence $\bar{v}_u^{(k)}(\bar{x}_0^*) = \bar{v}_u^{(k-1)}(\bar{x}_n^*)$. Of course, a Lissajous orbit is not actually periodic. This equality is only enforced for the purpose of completing the necessary iterations. Thus, $\tilde{u}(\bar{x}_0^*)$ is not truly aligned with the unstable subspace of $\bar{x}_0^*$. Consequently, the unstable directions associated with the first revolution cannot be accurately determined based on the present iteration scheme. The condition for convergence is that $\|\tilde{u}_u^{(k)}(\bar{x}_n^*) - \tilde{u}_u^{(k-1)}(\bar{x}_n^*)\| < \epsilon$, where ϵ represents the desired tolerance. The converged directions, $\bar{v}_u(\bar{x}_j^*)$, are aligned with the unstable subspace associated with $\bar{x}_j^*$. To accurately determine the unstable directions at other locations, $\bar{x}_q^*$, along the Lissajous orbit, except those along the first revolution, the vector $\bar{v}_u(\bar{x}_j^*)$ is utilized to approximate the unstable directions associated with the j^{th} revolution. That is, for $t_{j-1} \leq t_q \leq t_j$, the unstable direction associated with $\bar{x}_q^*$ is defined as

$$\bar{v}_u(\bar{x}_q^*) = \Phi(t_q, t_{j-1})\Phi^{-1}(t_j, t_{j-1})\bar{v}_u(\bar{x}_j^*) \ . \tag{2.74}$$

Note that this propagation proceeds backwards from $\bar{x}_n^*$ towards $\bar{x}_1^*$ rather forward from $\bar{x}_1^*$ to $\bar{x}_n^*$ as might be expected. This is to further ensure that any errors introduced, due to the assumption that $\bar{v}_u(\bar{x}_n^*) = \bar{v}_u(\bar{x}_0^*)$, do not propagate beyond the first revolution.

To compute the stable directions, consider the inverse form of equation (2.68), for $T = -T$, that is,

$$\begin{aligned} \bar{y}(-nT) &= \Phi(-nT, 0)\bar{y}(0) \ , \\ &= \Phi^{-1}(nT, 0)\bar{y}(0) \ , \\ \Phi^{-1}(nT, 0)\bar{y}(0) &= \sum_{j=1}^{6} c_j \frac{1}{\lambda_j^{(n)}} \bar{v}^{(j)} \ . \end{aligned} \tag{2.75}$$

Hence, if any eigenvalues $\|\lambda_j\| < 1$, almost any initial perturbation, under the mapping in equation (2.75), becomes aligned with the stable subspace of $\Phi(T, 0)$. The

corresponding system of vector equations that must be solved is defined as follows,

$$\begin{aligned} \bar{v}_s^{(k)}(\bar{x}_{n-1}^*) &= \Phi^{-1}(t_n, t_{n-1})\tilde{u}_s^{(k)}(\bar{x}_n^*) \ , \\ &\vdots \\ \bar{v}_s^{(k)}(\bar{x}_1^*) &= \Phi^{-1}(t_2, t_1)\tilde{u}_s^{(k)}(\bar{x}_2^*) \ , \\ \bar{v}_s^{(k)}(\bar{x}_0^*) &= \Phi^{-1}(t_1, t_0)\tilde{u}_s^{(k)}(\bar{x}_1^*) \ . \end{aligned} \tag{2.76}$$

Note that, for the stable directions, the initial guess now applies to $\bar{v}_s(\bar{x}_n^*)$ and the iteration process relies on the assumption that $\bar{v}_s^{(k)}(\bar{x}_n^*) = \bar{v}_s^{(k-1)}(\bar{x}_0^*)$. Hence, the stable directions associated with the last revolution on the orbit cannot be accurately determined. Naturally, for periodic orbits and nearly periodic Lissajous trajectories, the power method yields accurate results for all revolutions. Either approach presented here, the power method or the approach using a two-revolution period (2REVP), is suitable for approximating the stable and unstable directions associated with quasi-periodic orbits in the ephemeris model. Aside from the discontinuity in the 2REVP approach, both methods yield almost identical results.

3. Numerical Analysis

The goal of this investigation is the identification of some arc along a particular trajectory, as computed in the R3BP, that resembles the path of a particular Jupiter family comet, such as Oterma (OTR) or Helin-Roman-Crockett (HRC), during TSC. Since no closed-form analytical solution exists in the R3BP, identifying such a trajectory segment requires a numerical search in the phase space. A particular trajectory arc is defined as a "match" if a segment along the trajectory exhibits the most notable features of the comet's TSC path. Before a search is initiated, it is necessary to observe the known dynamical evolution of the comet, as described by the available ephemeris information, and note the TSC features. For instance, consider the heliocentric inertial path of HRC as illustrated in Figure 3.1. The bold line highlights the time during which the comet was captured between 1966 and 1985.

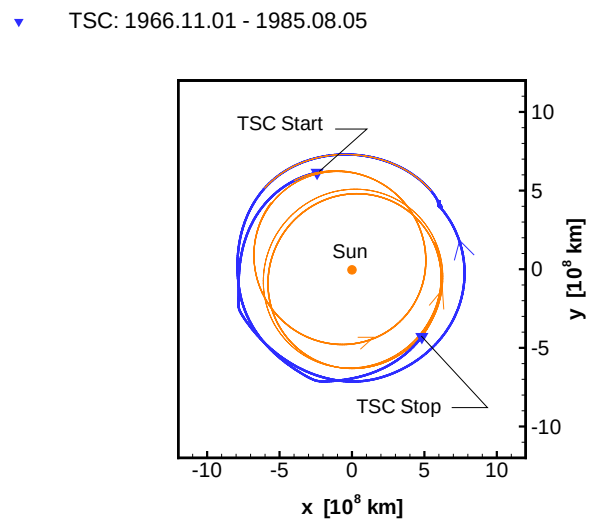

Figure 3.1. TSC of Helin-Roman-Crockett – Heliocentric Inertial Frame

Since solutions in the R3BP are typically represented in terms of the synodic rotating frame, as defined in Chapter 2, analysis of a particular comet's motion begins by transforming the available comet ephemeris information from the heliocentric inertial frame to the Sun-Jupiter synodic rotating frame (Wilson [41]). For HRC, the TSC path, as observed in the rotating frame, is illustrated in Figure 3.2. It is clear from Figure 3.2 that, during TSC, the comet completed several revolutions around Jupiter before it escaped. The path of HRC during capture is best described by *three*-dimensional chaotic motion in the vicinity of Jupiter. This is true of TSC in general.

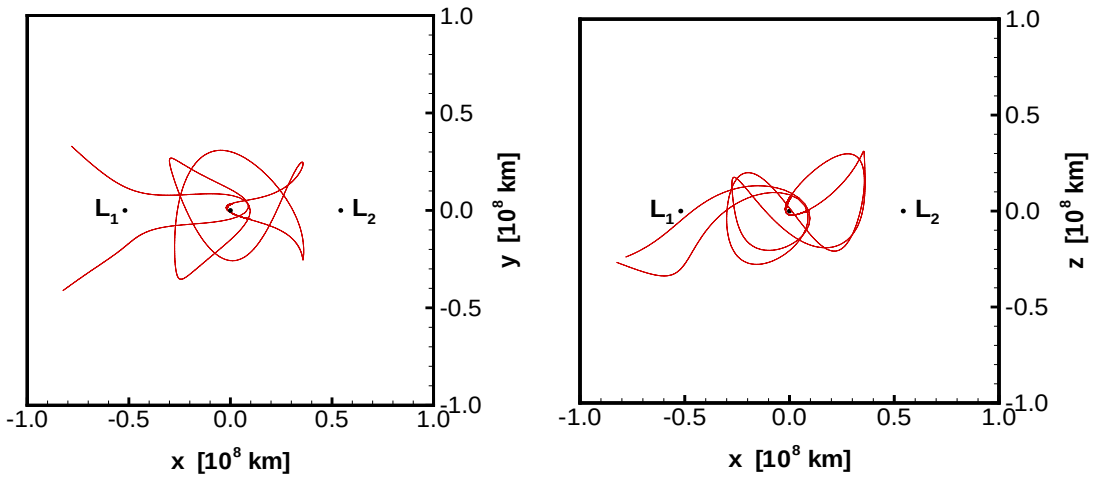

Figure 3.2. TSC of Helin-Roman-Crockett – Synodic Rotating Frame

In the CR3BP, *three*-dimensional chaotic motion is characteristic of trajectory arcs on the stable and unstable manifolds associated with *three*-dimensional periodic and quasi-periodic solutions in the vicinity of the collinear libration points L_1 and L_2. Hence, the search for a matching trajectory arc is initiated in the phase space of the CR3BP. The stable and unstable manifolds associated with the L_1 and L_2 halo families that are illustrated in Figure 2.3, serve as an initial basis for the numerical search. To optimize the search process, a priori knowledge of the geometry of the flow offers an advantage. Insight concerning the structure of the solution space, such as the general symmetry of solutions and the dynamical regions of exclusion, is applied to

minimize the volume of the phase space that must be searched. Further observations obtained through numerical explorations concerning the evolution of the flow along the stable and unstable manifolds associated with the L_1 and L_2 halo families also prove valuable. The following sections detail this additional investigation.

3.1 Temporary Satellite Capture and Regions of Exclusion

In astronomy, the more commonly accepted definition of TSC requires only that the Joviocentric energy become negative at some instance during the comet's orbital evolution. However, the Joviocentric energy of a comet can become negative near Jupiter without forcing the comet to transition between regions. Thus, a more specific definition of TSC is employed in this investigation.

For any temporary satellite capture, the comet must first enter the capture region as defined in terms of the zero-velocity surfaces. The comet will eventually exit the capture region, but its heliocentric orbit will be affected by its encounter with Jupiter. The extent of this effect depends on the type of encounter. There are two possible types of encounters. Suppose that the comet path originates in the interior region. The simplest type of capture (type 1) occurs when the comet crosses into the capture region and immediately exits to the exterior region. This type also applies to an immediate crossover from the exterior to the interior region. Thus, a type 1 capture is denoted as a "flythrough" of the capture region. The comet Oterma experienced two type 1 captures as illustrated in Figure 3.3. If, instead, the comet enters the capture region and experiences more than one close encounter with Jupiter before it exits the capture region, the encounter is defined as a type 2. A type 2 capture is apparent in Figure 3.4 which illustrates the evolution of the comet Helin-Roman-Crockett. The structure of the search for a match to represent the capture path of a particular comet depends on the type of capture that is reflected in the ephemeris data for the comet.

The first step in the search process is an examination of the phase space of the CR3BP to determine if it is possible for the type of motion associated with capture to exist. If so, it is then necessary to identify the subset of the phase space to commence

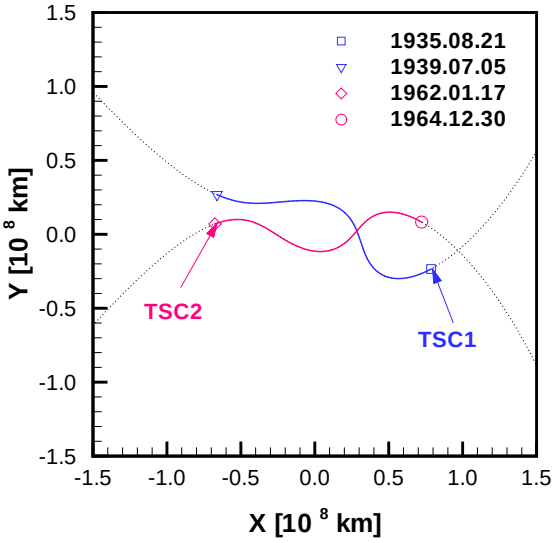

Figure 3.3. Type 1 Capture – Oterma

the search. These issues are addressed simultaneously by comparing the ephemeris path of the comet to the regions of exclusion in the CR3BP. As a reference, consider the zero-velocity contours associated with the libration points. From the discussion in Chapter 2, it is clear that, in the CR3BP, a type 1 capture can only exist for $C < C_2$, when the regions interior and exterior to Jupiter's orbit are bridged by the capture region. Furthermore, the paths of OTR and HRC seem to closely follow the bounds imposed by the "C"-shaped zero-velocity contours associated with $C_3 < C < C_2$, as illustrated in Figure 3.5. Thus, the search for a match to HRC and OTR is initiated by a focus on solutions within this range of values for the Jacobi constant. Near Jupiter, halo families in the vicinity of L_1 and L_2, as well as the associated stable and unstable manifolds, exist within this subset of the phase space. Since the overall path of these comets is characterized by three-dimensional chaotic motion, the search procedure is initiated by examining the stable and unstable manifolds associated with the SJL1 and SJL2 halo families.

3.2 Parameterizing the Search Space

To characterize the evolution of trajectories on the stable or unstable manifolds that are associated with a particular halo family, and to provide some structure to

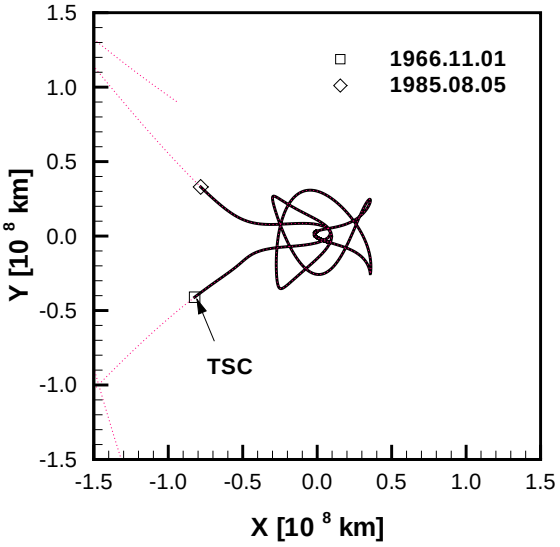

Figure 3.4. Type 2 Capture – Helin-Roman-Crockett

the search process, it is necessary to establish a set of parameters to identify: (a) the desired halo orbit along the family; (b) the desired fixed point, $\bar{x}^*$, along the orbit; and, (c) the local stable (W^s_{loc}) and unstable manifold (W^u_{loc}) associated with $\bar{x}^*$. Consider the subset of the SJL1 and SJL2 halo families presented in Figure 2.3. Each member of this subset is associated with a particular value of the Jacobi constant (C) as observed in Figure 3.6. In turn, a particular value of C defines a zero-velocity surface that bounds the regions of configuration space where solutions corresponding to this specified value of C can dynamically evolve. As discussed in Chapter 2, and across the range of C values that appear in Figure 3.6, the out-of-plane excursion along any solution within this C range is bounded by the closed, inner spheroid of the corresponding zero-velocity surface. Extensive numerical explorations of the flow representing the stable and unstable manifolds associated with this range of C, for both SJL1 and SJL2 families, indicate that any trajectory computed to evolve on the stable or unstable manifold, and associated with a specific halo orbit, is loosely bounded by the A_z amplitude of that same periodic orbit, Γ. Thus, the A_z amplitude is used to parameterize the halo orbits in a given family. This parameterization is only admissible for A_z amplitudes below a value of 60×10^6 km. Beyond this value

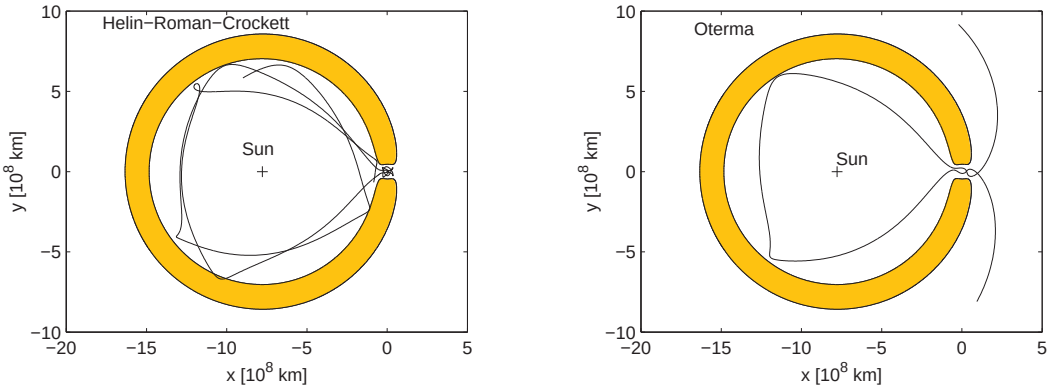

Figure 3.5. Ephemeris Path of Oterma and Helin-Roman-Crockett Compared to Zero-Velocity Contours in CR3BP

of A_z, more than two orbits can be determined with the same value of the Jacobi constant, as observed in Figure 3.6. For OTR and HRC, the maximum out-of-plane excursion is well below 60×10^6 km. Since the Jacobian and the A_z amplitude are in a one-to-one correspondence within this range, the A_z amplitude is an admissible parameter for this study.

For $A_z < 60 \times 10^6$ km, the eigenvalue structure of the monodromy matrix indicates that a fixed point, $\bar{x}^*$, that represents either an L_1 or an L_2 periodic halo orbit, Γ, has one-dimensional stable and unstable subspaces spanned by the corresponding eigenvectors. Since the computation of trajectories that represent motion on the surfaces $W^s(\Gamma)$ and $W^u(\Gamma)$ relies on these eigenvectors, the associated trajectories are parametrized in terms of the spatial orientation of the stable and unstable eigendirections and the corresponding fixed point. For example, consider the northern L_2 halo orbit, represented in Figure 3.7 in the form of a projection onto the yz-plane. Since halo orbits are symmetric about the xz-plane, let $(x,\ y,\ z)$ denote the position elements for every state along this orbit such that $(x_{max},\ 0,\ z_{max})$ corresponds to the maximum out-of-plane excursion, $(x_{min},\ 0,\ z_{min})$ corresponds to the minimum out-of-plane excursion, and $A_x = x_{max} - x_{min}$ is the maximum amplitude along the x-axis. For small A_x, it is reasonable to characterize a fixed point along the orbit by its (y, z) position elements. Halo orbits with large A_x amplitudes have small A_z

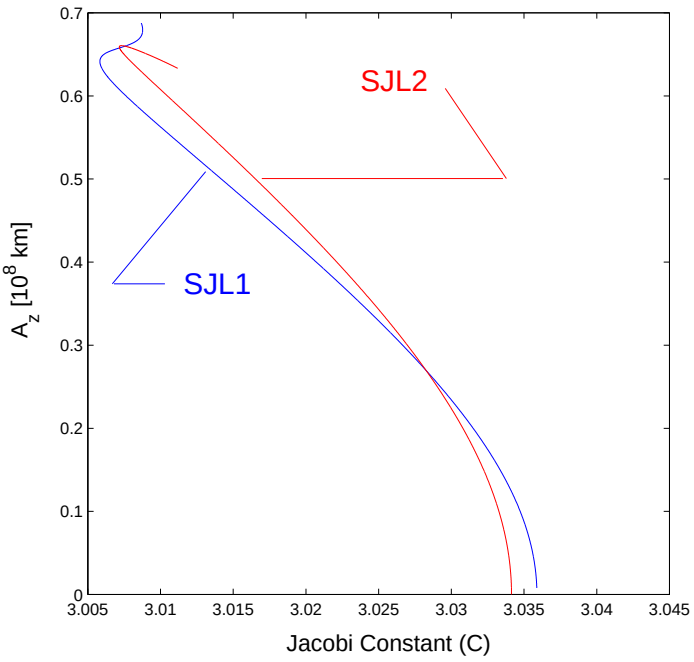

Figure 3.6. Halo Orbit Out-of-Plane Amplitude (A_z) as a Function of the Jacobi Constant Associated with the SJL1 and SJL2 Halo Families

amplitudes. Hence, this particular parameterization is not as effective for members of the halo family that are close to the xy-plane. However, the magnitude of the maximum out-of-plane component of the position vector corresponding to either HRC or OTR is not insignificant; thus, for this study, this parameterization is acceptable. To collapse the (y, z) pair into one parameter, let

$$\alpha = tan^{-1}(\sigma_1 y/\sigma_2 z) \ , \tag{3.1}$$

where σ_1 is defined as $+1$ for an L_1 halo and -1 for an L_2 halo orbit. The value of the integer σ_2 equals $+1$ for a northern halo and -1 for a southern orbit. This convention ensures that α always increases in the direction of motion along the orbit. Furthermore, α is constrained to a range between $0°$ and $360°$. This parameterization is convenient because it eliminates time as the independent variable and introduces a common element that relates each orbit in a given halo family. That is, at a given value of the Jacobi Constant, each state on the corresponding orbit can be represented as $\bar{x}(\alpha)$ for $0 \leq \alpha < 360°$.

Consider the fixed point characterized by the angle α on a specified halo orbit. In

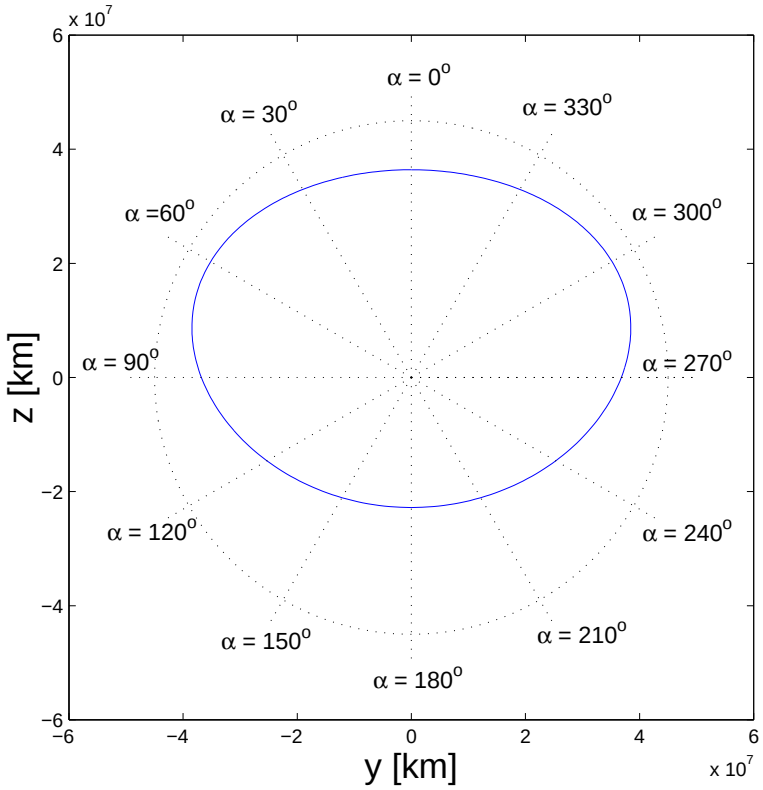

Figure 3.7. Characterization of Fixed Points on a Northern L_2 Halo Orbit

Chapter 2, it was established that the stable and unstable manifolds associated with a given halo orbit are mirrored about the xz-plane, as illustrated in Figure 2.15. Thus, to investigate the geometry of the flow on the stable and the unstable manifolds, it is only necessary to consider either the stable or unstable flow; the behavior of the alternate flow can be deduced. In addition, from the northern/southern symmetry of solutions, the geometry of the stable and unstable manifolds associated with the southern halo families is a mirror image, about the xy-plane, of the flow on the manifolds associated with the corresponding northern halo families. Thus, the analysis that follows is based on the stable manifold associated with the northern SJL1 and SJL2 halo families.

The stable eigenvector that is computed from the monodromy matrix, and associated with a fixed point $\bar{x}(\alpha)$, is six-dimensional with three position elements (x_s, y_s, z_s) and three velocity elements ($\dot{x}_s$, $\dot{y}_s$, $\dot{z}_s$). Thus, the six-dimensional unit sta-

ble eigenvector, $\hat{Y}^{W_s}(\alpha)$, can be expressed in terms of two *three*-dimensional vectors, $\bar{Y}_p^{W_s}(\alpha) = [x_s \; y_s \; z_s]^T$ and $\bar{Y}_v^{W_s}(\alpha) = [\dot{x}_s \; \dot{y}_s \; \dot{z}_s]^T$. Note that $\bar{Y}_p^{W_s}(\alpha)$ and $\bar{Y}_v^{W_s}(\alpha)$ are not unit vectors. Since $\bar{Y}_p^{W_s}(\alpha)$ and $\bar{Y}_v^{W_s}(\alpha)$ are *three*-dimensional vectors, each can be represented in configuration space in terms of an equivalent unit direction, relative to the Sun-Jupiter rotating frame, and associated with the fixed point $\bar{x}(\alpha)$ along the halo orbit. The stable manifold associated with $\bar{x}(\alpha)$ can be parameterized in terms of $\bar{Y}_p^{W_s}$ or $\bar{Y}_v^{W_s}$. For example, the unit vector along $\bar{Y}_v^{W_s}(\alpha)$ can be expressed in terms of azimuth relative to the rotating x-axis (α_d) and elevation relative to the xy-plane (β_d). These definitions are pictorially represented in Figure 3.8.

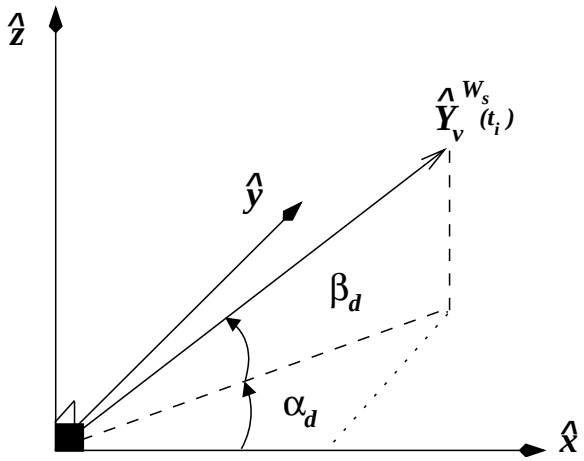

Figure 3.8. Characterization of Stable/Unstable Eigenvector Directions

The azimuth is measured in the positive sense when $\dot{y}_s > 0$; the elevation angle is measured as positive when $\dot{z}_s > 0$. The azimuth angle (α_d) is constrained to be evaluated between $\pm 180^\circ$ and the elevation angle (β_d), then, always possesses a value between $\pm 90^\circ$. For the range of A_z amplitudes considered in this study, numerical analysis demonstrates that every fixed point along an unstable L_1 or L_2 halo orbit corresponds to a unique (α_d, β_d) pair. This numerically observed trend is supported by Figure 3.9. Each curve in Figure 3.9 illustrates the relationship between α_d and β_d for a subset of the SJL2 northern halo family, for members of the halo family with out-of-plane amplitudes under 60×10^6 km. The dashed lines correspond to the (α_d, β_d) pairs for the stable manifold and the (α_d, β_d) pairs for the unstable manifold

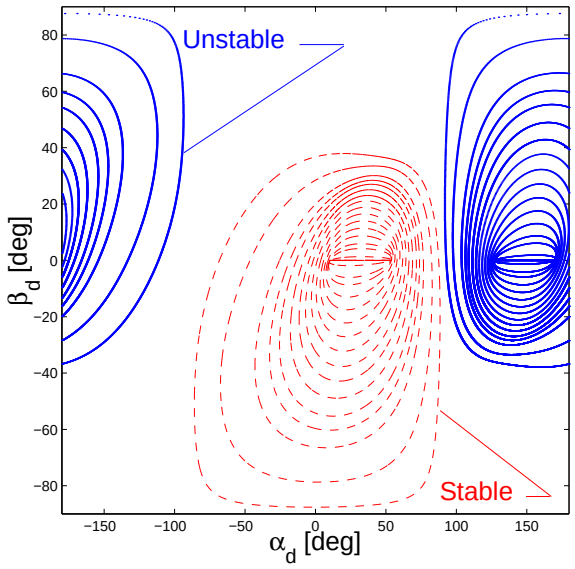

Figure 3.9. Evolution of $\bar{Y}_v^{W_s}$ Along SJL2 Northern Halo Family

appear as dotted curves. The size of each curve is proportional to the ratio of the A_y and A_z amplitudes of the corresponding halo orbit. Hence, halos close to the xy-plane are represented by an α_d-β_d curve that resembles a horizontal line; that is, over one revolution of the orbit, the eigenvectors essentially possess azimuth but no elevation. This is consistent with the expected result since, in the limiting case, the stable and unstable manifolds corresponding to a planar halo orbit are themselves planar. The numerically determined uniqueness of the $(\alpha_d,\ \beta_d)$ pair, as observed in Figure 3.9, over the range of A_z amplitudes useful here, supports the validity of the parameterization.

To better visualize the state, $\bar{x}(t_i)$, associated with a particular $(\alpha_d,\ \beta_d)$ pair, it is convenient to consider contours of α_d and β_d on a surface defined by the position elements along each halo orbit in a family. This is illustrated in Figure 3.10 for the SJL2 northern halo family. Contours of constant α_d and β_d appear as nonlinear, smooth, *three*-dimensional curves along the halo family, in contrast to contours of constant α which appear as *two*-dimensional rays originating from the central point, $(y, z) = (0, 0)$, in Figure 3.7.

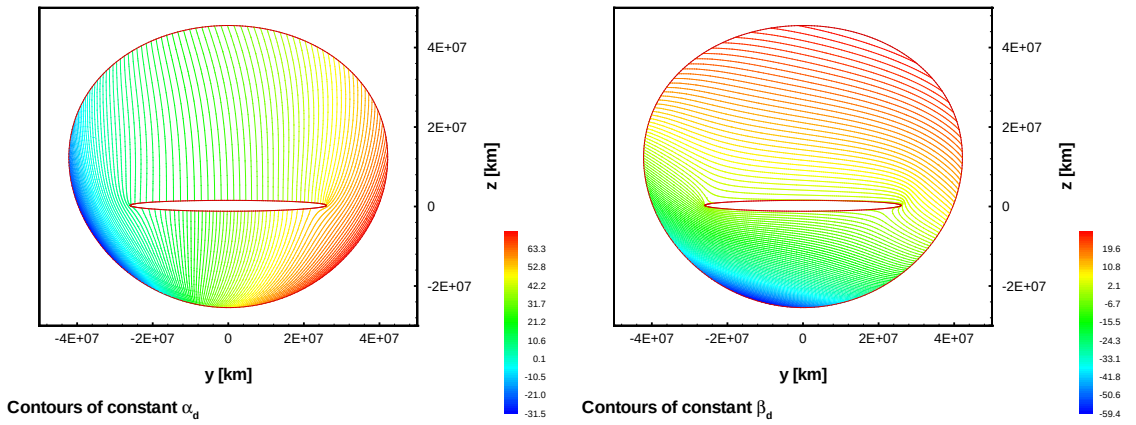

Figure 3.10. Evolution of Stable Eigenvector Along SJL2

3.2.1 Search Approach

Once the desired subset of the phase space is parameterized, the search for a match can be initiated. As previously stated, the goal is the identification of a trajectory arc along some stable or unstable manifold, one that is associated with a periodic or quasi-periodic solution and resembles the path of HRC and OTR during TSC. Determination of such an arc is defined as a "match". Initially, the search is focused on the phase space in the CR3BP; in particular, a match is sought by examining trajectories representing motion on the stable manifolds associated with *three*-dimensional halo orbits. A segment along a particular solution is considered a full "match" only if both the position and velocity states of the comet are comparable to those on the matching arc. For simplicity, the search initially proceeds to attain a match for the position elements. This can be accomplished visually by comparing projections of the comet path onto the xy- and xz-planes, to trajectory arcs along the stable manifold. Since a match in the xy-plane is necessary for a full state match, the initial search is further concentrated on the xy-plane.

The next step in the search process is the determination of an initial guess for the target halo orbit. The initial guess is based on a measurement of the comet's maximum out-of-plane excursion as it passes through either the interior or the capture

region. The A_z amplitude of the halo orbit is based on this measurement. Whether the measurement correlates to the maximum excursion in the interior or capture region is ultimately an arbitrary choice. It is important to note that this only results in an initial guess and does not necessarily yield the best match. However, extensive numerical explorations reveal that this is typically a good approximation and a match can usually be isolated amongst the stable and unstable manifolds associated with a periodic orbit that is near the initial halo orbit. Given an estimate for the A_z amplitude, it is not immediately apparent whether an L_1 or an L_2 halo is the best choice. However, numerical analysis reveals that the initial choice is not critical. Since either L_1 or L_2 orbits will ultimately produce a match, the following analysis is based on the northern SJL2 halo family.

The search proceeds by numerically propagating trajectories on the stable manifold that are associated with various states, $\bar{x}(\alpha)$, along the orbit, for α defined over the full range, $0^\circ \leq \alpha \leq 360^\circ$. From this set, it is likely that a trajectory can be isolated that exhibits *at least* some of the desired features that are observed in the projection of the comet's capture path onto the xy-plane. It is not necessary that the match be exact. Some of the features may appear inverted or mirrored about an axis or a plane. For example, consider a collection of trajectories on a surface that reflects the stable manifold associated with $\bar{x}(\alpha)$, for $0 \leq \alpha \leq 180^\circ$. Suppose that arcs along these trajectories resemble the comet path during capture, but, in the xy projection, the computed trajectories appear mirrored about the x-axis. From equations (2.62)-(2.63), it is deduced that the unstable manifold associated with $\bar{x}(360^\circ - \alpha)$ is a mirror image – about the xz-plane – of the stable manifold associated with $\bar{x}(\alpha)$. Hence, for a match, the xy projection is better represented by the unstable manifold associated with $\bar{x}(360^o - \alpha)$. Clearly, this is a geometric match and, thus, it is also necessary to ensure that the flow proceeds in the same direction for both the comet and the matching trajectory. Provided the direction of motion is consistent between the comet and the computed arc that renders a position match, consider the projection of the integrated arc onto the xz-plane. If the arc along the manifold also

matches the comet path in the xz projection, then a position match is achieved and the next step is a match of the velocity states as well. On the other hand, if the projection onto the xz-plane appears inverted about the xy-plane, it is then clear, from the northern/southern symmetry of solutions (SP1), that the position match is more accurately represented by the unstable manifold associated with the corresponding southern halo orbit. It is possible that, at this point, the position match is still not sufficiently close to the path of the comet. Nonetheless, a closer match might exist in a neighborhood of this solution. Thus, it is necessary to determine if it is possible to improve the match without loosing the overall character of the matching arc. Naturally, the geometry of the stable and unstable manifolds associated with neighboring periodic orbits share similar features. Recall that the stable and unstable manifolds associated with $\bar{x}(\alpha)$ are characterized by a particular $(\alpha_d,\ \beta_d)$ pair. The search for a match in the neighborhood of $\bar{x}(\alpha)$ is facilitated by this parameterization. That is, the search for a neighboring match can proceed along contours of constant α, α_d, or β_d.

Consider the sections of the surfaces $W^s(\Gamma)$ and $W^u(\Gamma)$ that exist in the vicinity of Jupiter, between L_1 and L_2. Each trajectory along these manifolds includes at least one close approach to the planet ($\bar{r}^{P_2P_3} \cdot \bar{V}^{P_2P_3} = 0$). Of particular interest is the first encounter. Since the global unstable manifold is numerically integrated with $\Delta t > 0$, the "first" encounter occurs after the trajectory departs the immediate vicinity of the halo orbit. The definition for the stable manifold is similar, except that $\Delta t < 0$. The subsequent features along each trajectory depend on the configuration of the first encounter: (a) distance to Jupiter ($|\bar{r}^{P_2P_3}|$); (b) azimuth (AZ) and elevation (EZ) angles relative to the rotating frame; and, (c) the inertial velocity relative to the planet, $\bar{V}^{P_2P_3}$, as illustrated in Figure 3.11. Examining the evolution of trajectories in the neighborhood of $\bar{x}(\alpha)$ and along contours of constant α, α_d, or β_d, is equivalent to varying the configuration of the first encounter, particularly the azimuth and elevation angles. The sensitivity of the trajectory to changes along any of these contours varies according to the location on the orbit (α) and the energy level

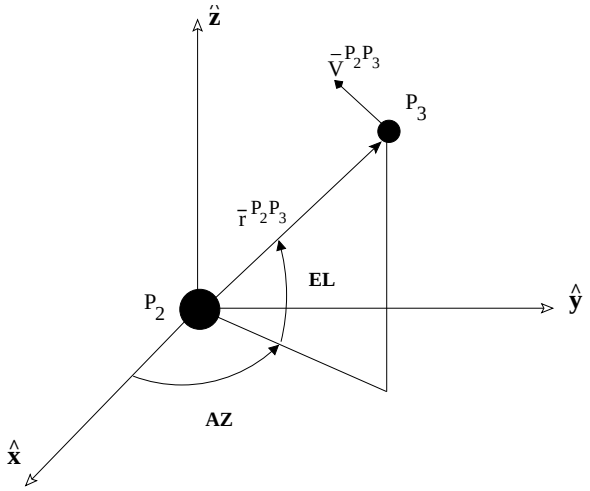

Figure 3.11. Configuration of Close Encounter

(C). For instance, consider a contour of $\alpha_d = 60°$ for 25×10^6 km $< A_z < 44 \times 10^6$ km. For a halo orbit with $A_z = 25.2 \times 10^6$ km, $\alpha_d = 60°$ is equivalent to $\alpha = 270°$. Then, the evolution of the azimuth of the first encounter, across other halo orbits in the family, along a contour of $\alpha_d = 60°$ appears in Figure 3.12. This curve is compared to

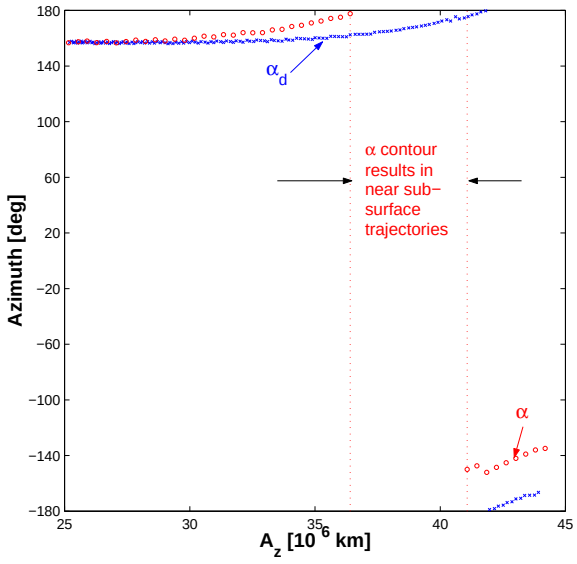

Figure 3.12. Evolution of First Close Encounter: $\alpha_d = 60°$ and $\alpha = 270°$

a second result in the same figure, that is, shifting across the family on a contour of $\alpha = 270°$. Note that, unlike the curve reflecting the α_d contour, moving along the α contour produces a range of values of A_z for which the azimuth of the first encounter

results in $|\bar{r}^{P_2P_3}| \leq 10R_J$ (the numerical stopping condition) where R_J represents the radius of Jupiter. In this region of the halo family, trajectories are more sensitive to changes in α than to changes in α_d. Hence, trajectory features are better preserved along the α_d contour. This observation is even more apparent in Figures 3.13 and 3.14. In these figures, trajectories representing arcs on the stable manifolds corre-

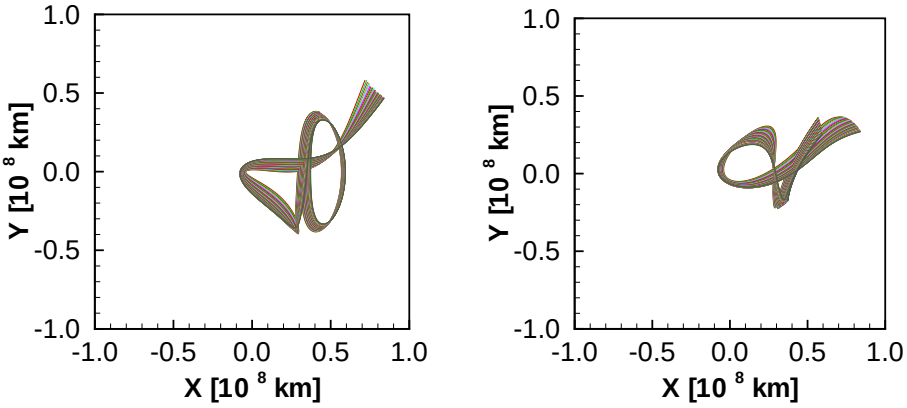

Figure 3.13. Evolution of Stable Manifold Along $\alpha_d = 60°$

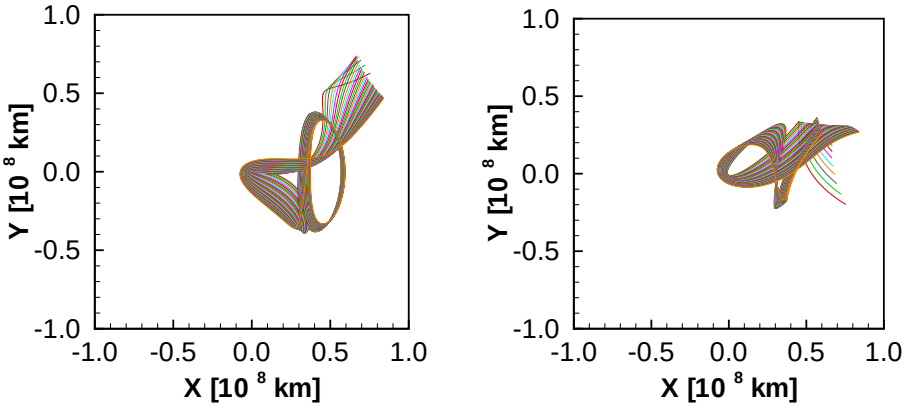

Figure 3.14. Evolution of Stable Manifold Along $\alpha = 270°$

sponding to different halo orbits are plotted over a range of out-of-plane amplitudes, A_z, such that 25×10^6 km $< A_z < 36.1 \times 10^6$ km. In Figure 3.13, the trajectories are selected along contours of constant α_d; in Figure 3.14, the trajectories result from a shift along constant α contours. The observation that characteristics are better

maintained along contours of constant α_d depends once again on C and α. In the previous example, for the results in Figures 3.13-3.14, the range of orbits identified in terms of A_z amplitudes, is relatively small. Consider instead a contour corresponding to $\alpha_d = 43°$, for the range 0.92×10^6 km $< A_z < 18.3 \times 10^6$ km; almost double the range of A_z amplitudes that are available in the previous example. For a halo orbit with $A_z = 18.3 \times 10^6$ km, $\alpha_d = 43°$ is equivalent to $\alpha = 305°$. Both curves are generated and appear in Figures 3.15 and 3.16. Once again, it is obvious that the

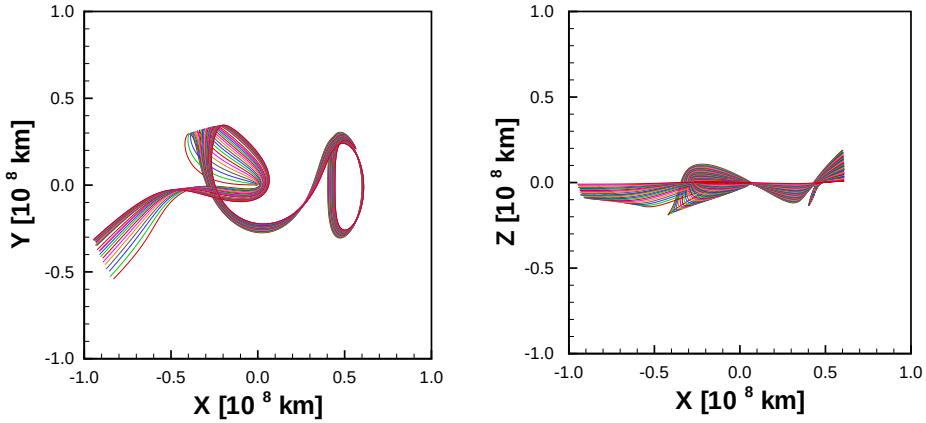

Figure 3.15. Evolution of Stable Manifold Along $\alpha_d = 43°$

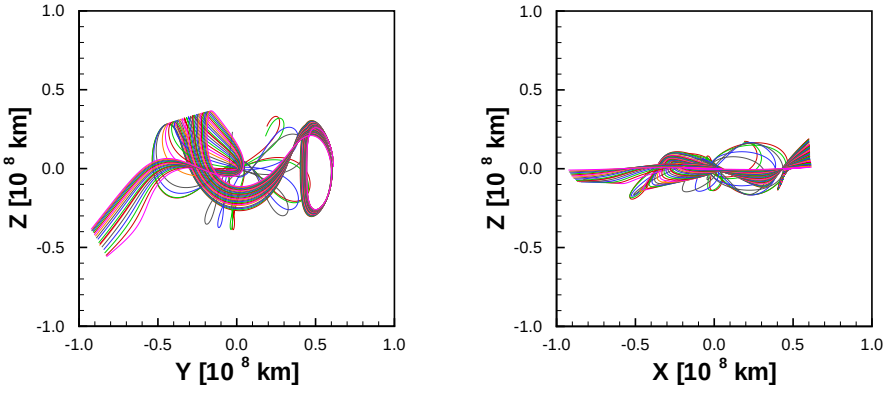

Figure 3.16. Evolution of Stable Manifold Along $\alpha = 305°$

features are better preserved along the α_d contour. The observation that contours of α_d better preserve the characteristics of a trajectory arc is most useful once a candidate match for a segment or arc along a particular comet path is identified. Suppose

a candidate match for the path of HRC in the capture region is identified among the trajectories representing the stable manifold associated with SJL2. The comet HRC experiences several close approaches to Jupiter during TSC. Examine the numerically generated trajectory. If the flyby altitude of the close approaches along the potential trajectory are too low, the match can be improved, without losing the essential features, by selecting a neighboring trajectory with the same α_d. Since the (α_d, β_d) pairs are unique along a family, the new computed trajectory – one that constitutes an improved match – is associated with a different member of SJL2.

3.2.2 Numerical Near-Symmetry Across Halo Families

Numerical observations on the evolution of the stable/unstable manifolds associated with orbits that belong to the SJL1 halo family, compared to the manifold surfaces associated with the SJL2 family of orbits, reveal some qualitative similarities across the halo families. For instance, consider the stable manifold associated with the state $\bar{x}_1(\alpha_1) = [x_1 \;\; y_1 \;\; z_1 \;\; \dot{x}_1 \;\; \dot{y}_1 \;\; \dot{z}_1]^T$ on a northern L_1 halo orbit and compare it to the unstable manifold corresponding to a state $\bar{x}_2(\alpha_2) = [x_2 \;\; y_2 \;\; z_2 \;\; \dot{x}_2 \;\; \dot{y}_2 \;\; \dot{z}_2]^T$ along a southern L_2 halo orbit. Choose these orbits such that $y_1 \approx y_2$ and $z_1 \approx -z_2$ as illustrated in Figure 3.17 for an L_1 halo of $A_z \approx 26 \times 10^6$ km and L_2 orbit with $A_z \approx 24 \times 10^6$ km. Note that this selection is not arbitrary since, as previously

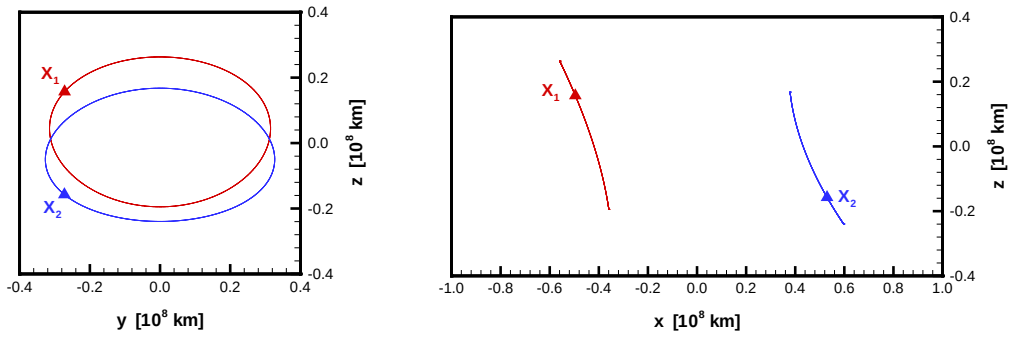

Figure 3.17. Similar L_1 and L_2 Orbits

discussed, the evolution of the (α_d, β_d) pair is proportional to the ratio of $y : z$. Comparison of the corresponding α_d-β_d diagrams reveals some numerical near-symmetries.

These symmetries are easily observed from the α-α_d-β_d diagram in Figure 3.18. Note that the β_d curve representing the elevation of the stable eigenvector along the northern L_1 halo orbit (dashed red line) appears mirrored about $\alpha = 180°$ when compared to the elevation of the unstable direction along the southern L_2 halo orbit (dashed blue line). Also, the α_d curve representing the azimuth of the stable eigenvector along the L_1 halo orbit (solid red line), appears mirrored about both $\alpha_d = 0°$ and $\alpha = 180°$ relative to the azimuth of the unstable direction along the L_2 halo orbit. That is, the (α_d, β_d) pair associated with the stable eigenvector along the northern L_1 halo orbit exhibits some inverse near-symmetry properties compared to the (α_d, β_d) pair associated with the evolving unstable eigenvector along the southern L_2 halo orbit. Since the geometrical features of a trajectory depend on the (α_d, β_d) pair, this

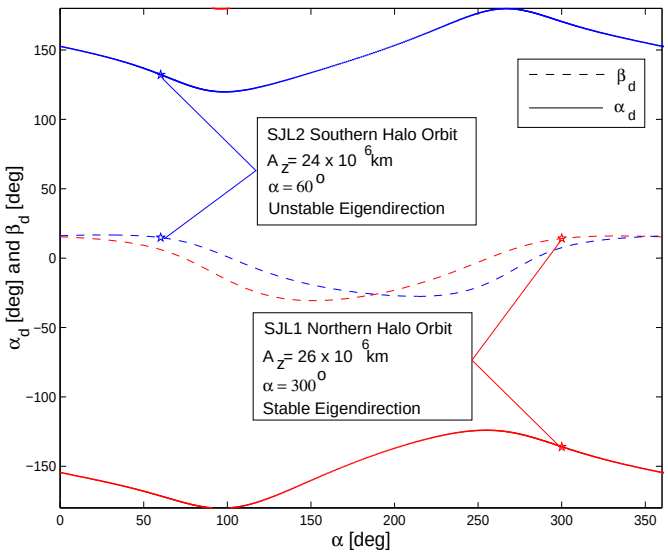

Figure 3.18. Similarities Between (α_d, β_d) Pair Across Halo Families

suggests some similarities between the geometry of the flow along the stable and unstable manifolds across the halo families, at least in the capture region. This trend is confirmed by globalizing the stable manifold associated with $\bar{x}_1(\alpha_1)$ as well as the unstable manifold associated with the state $\bar{x}_2(\alpha_2)$, as identified in Figure 3.17. The resulting trajectories appear in Figure 3.19. These trajectories, corresponding to the stable and unstable manifolds, appear as near mirror images on the xy-plane and

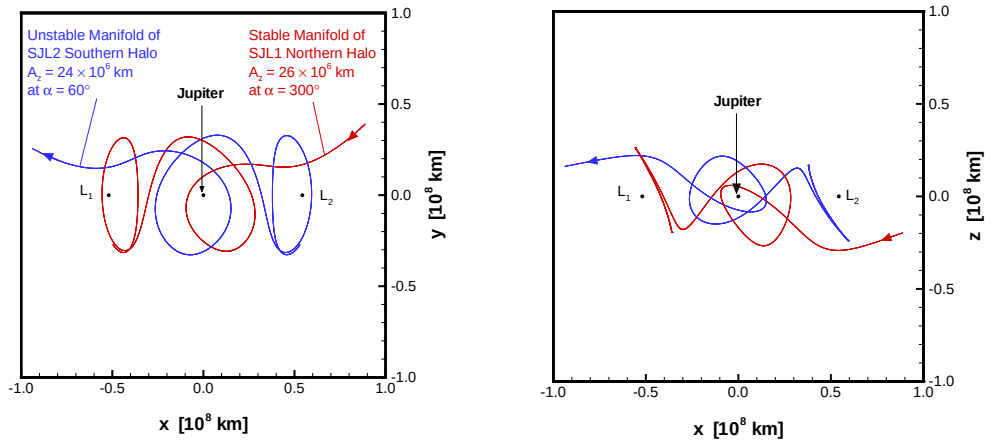

Figure 3.19. Stable/Unstable Manifolds: Example of Numerical Near-Symmetry

their out-of-plane components are apparently inverted. The converse also appears valid for a southern L_1 halo and a northern L_2 halo, due to the natural symmetry across the xy-plane in the CR3BP (SP1). This observation, based on numerical analysis, suggests that the initial choice of an L_1 or an L_2 halo orbit is arbitrary when initiating the search process. Once a match is identified or isolated, one that exhibits the most notable features of the known comet trajectory in the capture region, then the most appropriate halo family, that is, L_1 or L_2, for the best match to the comet trajectory can be determined.

3.2.3 Critical Energy Level for TSC

Recall that the goal of the search process is the identification of an arc along a stable or unstable manifold that resembles the path of the comet during capture. The search is then structured to seek the segment along the manifold that is most likely to yield trajectories with the desired characteristics. The evolution of the global stable and unstable manifolds, as $|t| \rightarrow \infty$, associated with a particular halo orbit, is bounded by the corresponding *zero*-velocity surface. Since the available interior and exterior regions that are bounded by the *zero*-velocity surfaces are joined by capture region between L_1 and L_2, all trajectories on either the stable or unstable manifolds can move across these regions an infinite number of times, as $|t| \rightarrow \infty$. For example,

consider a trajectory representing motion on the stable manifold associated with $\bar{x}(\alpha)$ along an L_1 northern halo orbit. The local stable manifold, W^s_{loc}, associated with $\bar{x}(\alpha)$ is formed as the union of two half-manifolds, W^{s+}_{loc} and W^{s-}_{loc}, as previously defined in Figure 2.9. For an SJL1 halo orbit, let W^{s+}_{loc} be the half-manifold that approaches $\bar{x}(\alpha)$ from Jupiter and W^{s-}_{loc} the half-manifold that approaches $\bar{x}(\alpha)$ from the general direction of the Sun. If W^{s+}_{loc} is globalized such that $\Delta t < 0$, the resulting trajectory eventually either escapes the vicinity of Jupiter, after one or more close encounters with the planet, or collides with Jupiter. Of particular interest are the trajectories that escape the vicinity of the planet. Note that trajectories on W^{s-}_{loc} escape the vicinity of Jupiter faster than those on W^{s+}_{loc} because they do not encounter Jupiter after they depart the immediate neighborhood of the halo orbit. In both cases, as $t \to -\infty$ these trajectories can return through the opening of the *zero*-velocity surface and move across regions an infinite number of times. In theory, as the trajectory is numerically propagated, each return represents a potential match for the TSC path of a particular comet. However, in practice, the range of possibilities is limited by the numerical error associated with the required length of the integration. This error is compounded by the chaotic nature of the dynamics in the CR3BP. That is, "*given two initial conditions, arbitrarily close to one another, the trajectories emanating from these initial conditions diverge at a rate characteristic of the system, until for all practical purposes, they become uncorrelated.*"[1] For trajectories associated with W^{s+}_{loc}, the onset of this sensitivity is advanced by close encounters with Jupiter. Trajectories associated with W^{s-}_{loc} are more sensitive to the integration time. In either case, it is desirable to keep the integration time as short as possible to maintain the reliability and accuracy of the match. A reliable match can be reproduced in the presence of perturbations. In this study, reliability is essential when transitioning the match from the CR3BP to the ephemeris model.

To maintain the reliability of a given match, the search process is structured according to the type of capture that is observed along the path of the comet of

[1] Parker and Chua [20]

interest. For a type 2 capture, where multiple close encounters are incorporated, the integration time is reduced by searching for heteroclinic connections among the trajectories that represent the stable and unstable manifolds corresponding to the SJL1 and SJL2 halo families. Thus far, identifying these connections in the *three*-dimensional R3BP is based on numerical techniques that combine Poincaré maps with differential correction schemes, such as that proposed by G. Goméz and J. Masdemont [43]. In the planar CR3BP, Koon, Lo, Marsden and Ross [17] developed a semi-analytical process to establish the existence of heteroclinic connections in the planar model, but the actual identification and computation of these connections still relies on numerical techniques similar to those employed by Goméz and Masdemont. Since the goal is restricted to the identification of arcs along a stable or unstable manifold that incompass the most notable features of the capture path of the comet, precise heteroclinic connections are not necessary. It is sufficient to identify a combination of trajectory arcs that exhibit the desired features.

For a type 1 capture, isolation of a match is simpler. The significant features of a type 1 capture are best represented by trajectories that return to the capture region after their first escape. To maintain the reliability of the match, only first return trajectories, associated with W_{loc}^{s-}, are considered. That is, for the SJL1 halo family, the particle (with motion represented by the simulated trajectory) must be re-captured by Jupiter after one revolution in the interior region. For the SJL2 halo family, trajectories on W_{loc}^{s-} move beyond the *zero*-velocity surface. Since the time required to complete one revolution in this region is much longer, first returns are rare and very sensitive to changes in initial conditions. Hence, only the stable and unstable manifolds associated with the SJL1 halo family are considered when searching for a match to incorporate a type 1 capture.

The results of extensive numerical studies suggest that, for a type 1 capture, a specific energy level, that is, one less than or equal to -2.5 km^2/sec^2, is apparently required (in the CR3BP) for trajectories associated with the SJL1 halo family to experience a TSC, as defined here. Along the SJL1 family of periodic halo orbits,

trajectories are generated to approximate the stable manifold, and those that also experience a crossover after one revolution in the interior region, are identified in Figure 3.20. Each orbit is represented by its out-of-plane A_z amplitude; orbits that satisfy the crossover condition are noted as a function of the critical angular location (α). The shaded regions in the figure indicate the range over α for which a trajectory

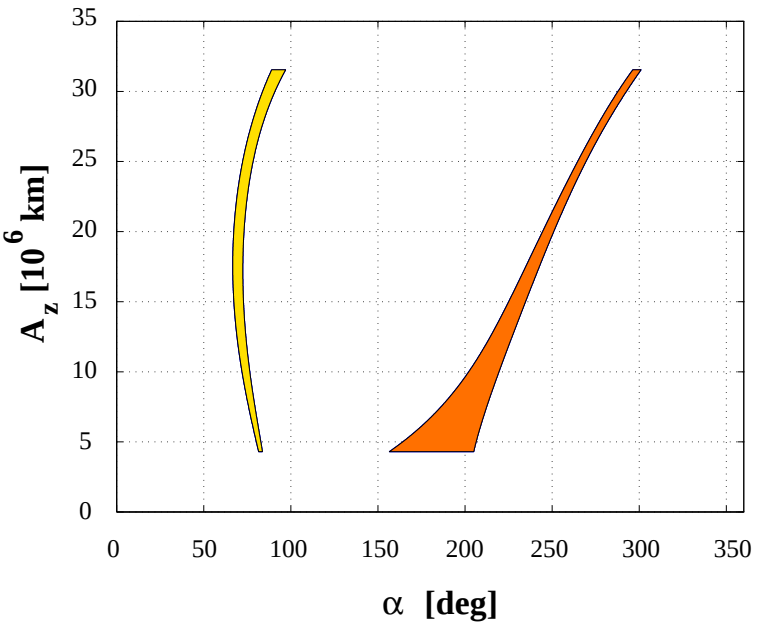

Figure 3.20. Capture Condition for SJL1 Stable Manifold Trajectories After One Revolution in the Interior Region

defined along the stable manifold crosses into the capture region from the interior region. This critical angle α is crucial in identifying a match for OTR in the CR3BP. As illustrated in Figure 3.20, if the trajectories representing the stable/unstable manifolds, and associated with orbits in the SJL1 halo family, are propagated towards the interior region, only a handful will return through the capture region after one revolution.

3.3 Transfer of Solutions to the Ephemeris Model

The ultimate goal of this investigation is to match the *six*-dimensional state of the comet during capture. Initially, the search is focused on matching the position elements in the CR3BP. Once a position match is isolated among the stable or unstable

manifolds associated with the SJL1 and SJL2 halo families in the CR3BP, it is not unusual to observe that the velocity states are not sufficiently close to justify a complete match. This problem is corrected by transferring the solution to the ephemeris model. In the ephemeris model, the differential equations are numerically integrated using actual ephemeris information for Jupiter. That is, no assumptions are imposed about the motion of the primaries. Since the trajectory is not periodic, neither are the stable/unstable directions or, consequently, the α_d-β_d diagrams. However, for a Lissajous trajectory that resembles a halo orbit, the relationship between α_d, β_d, and α does not change significantly as observed in Figure 3.21. Although the trajectory

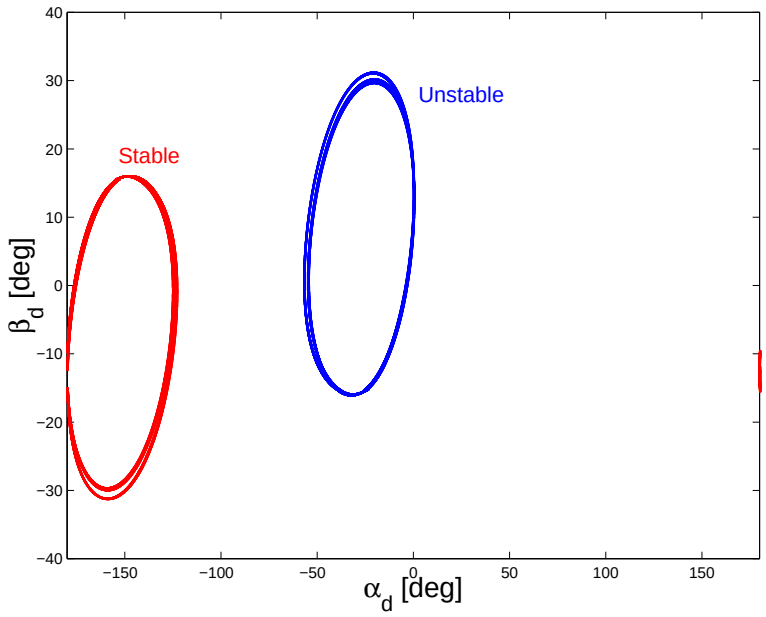

Figure 3.21. α_d-β_d Diagram for Northern SJL1 Lissajous Trajectory over Seven Revolutions

(or trajectory arc) that is generated as a match in the ephemeris model does not originate from the same angular location (α_C) as in the CR3BP, typically the match can be reacquired by considering trajectories associated with $\|\alpha - \alpha_C\| < \delta$, for δ small. As the Lissajous orbit expands around the halo orbit, so do the α_d-β_d diagrams. Furthermore, the small changes in α_d and β_d across each revolution on the Lissajous trajectory introduce new opportunities for identifying a match to a comet's TSC path. That is, in some cases a small change in α_d or β_d can result in significant

changes to the trajectory, particularly in the case of a type 1 capture where the stable and unstable manifolds are propagated towards the Sun and the integration time is longer.

3.4 Identification of a Match for Oterma

In the past, OTR was captured by Jupiter on two separate occasions; once from 1935 to 1939, and, later, from 1962 to 1964. Both encounters with Jupiter resulted in a type 1 TSC. The search for a match to reflect these flythroughs begins by measuring the maximum out-of-plane excursion along the path of the comet while it orbits the Sun in the interior region or Jupiter in the capture region. Based on the distance corresponding to this maximum out-of-plane excursion, an initial guess for the A_z amplitude of the halo orbit can be obtained. From the plot in Figure 3.20, states along this halo orbit that result in a trajectory which shadows the stable manifold and returns through the opening of the zero-velocity surface after one revolution in the interior region can be determined. If a candidate match is identified, but the direction is inverted, or the trajectory itself appears inverted, the symmetry properties (SP1 and SP2) can be applied to improve the match for a given A_z amplitude. If, for the initial A_z amplitude, a candidate match exists but is not sufficiently close to the path of the comet, the features of the trajectory can be adjusted by examining nearby trajectories along lines of constant α_d. Thus, the essential characteristics of the trajectory will be preserved by changing the A_z amplitude of the halo orbit, while maintaining a constant direction for the azimuth angle of the stable (or unstable) eigenvector.

In the CR3BP, one available arc that matches the first capture of Oterma is illustrated in Figure 3.22. Since the two captures experienced by Oterma are roughly mirrored about the xz-plane, once a segment is identified, one that resembles the first capture, an arc that resembles the second capture of Oterma is easily isolated by making use of the stable/unstable manifold symmetry (SP2). A possible matching arc for the second capture is illustrated in Figure 3.23. The best match obtained in the CR3BP can be further improved by transferring the solution into the ephemeris

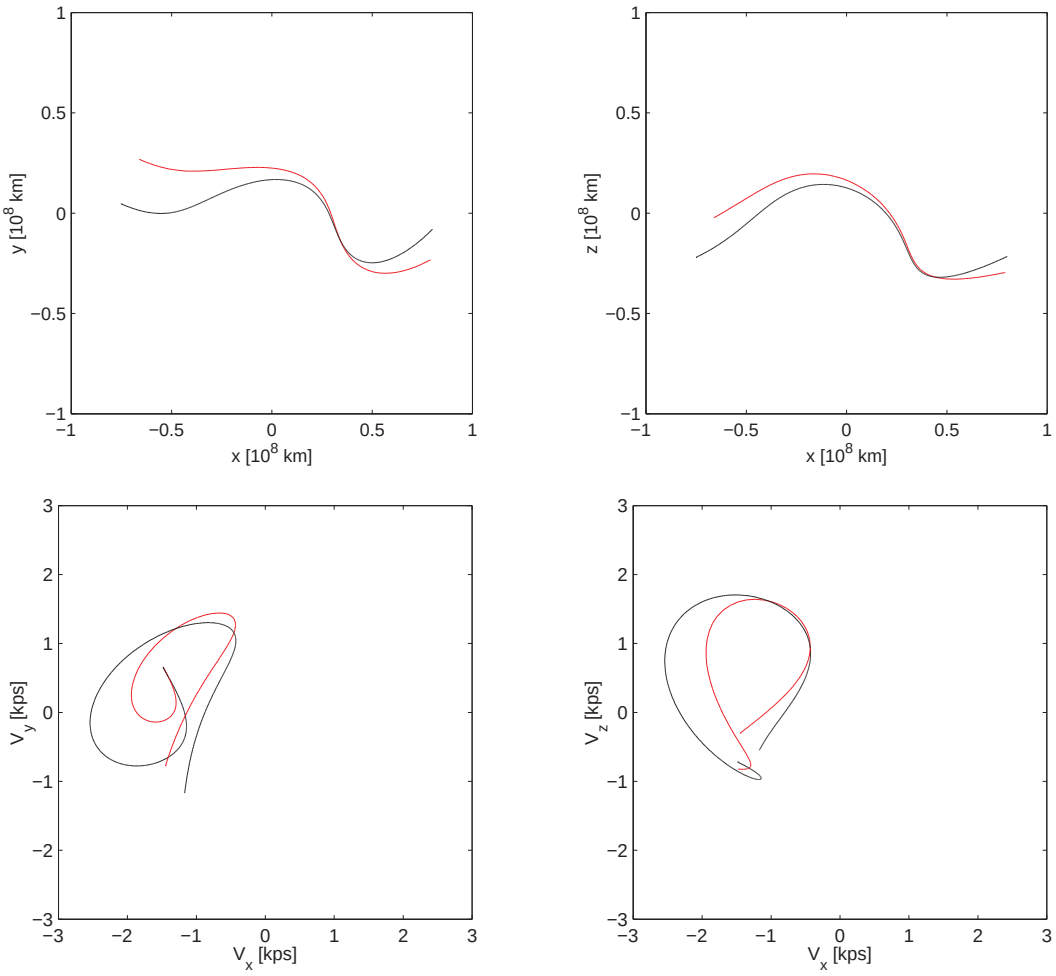

Figure 3.22. Position and Velocity Match for Oterma
in the CR3BP (1935-1939)

model. The match for the first capture of OTR, as it is developed and computed in the ephemeris model, is plotted in Figure 3.24. The red curve in this figure represents the stable manifold that is associated with a northern SJL1 quasi-periodic Lissajous trajectory, computed in the ephemeris model. The blue curve represents an arc along the unstable manifold of the same Lissajous trajectory. The black curve represents a segment along the comet's orbital path available directly from comet ephemeris data.

3.5 Identification of a Match for Helin-Roman-Crockett

HRC experienced a type 2 capture by Jupiter from 1966 until 1985. Since HRC remained in the vicinity of Jupiter for an extended period of time, the search for

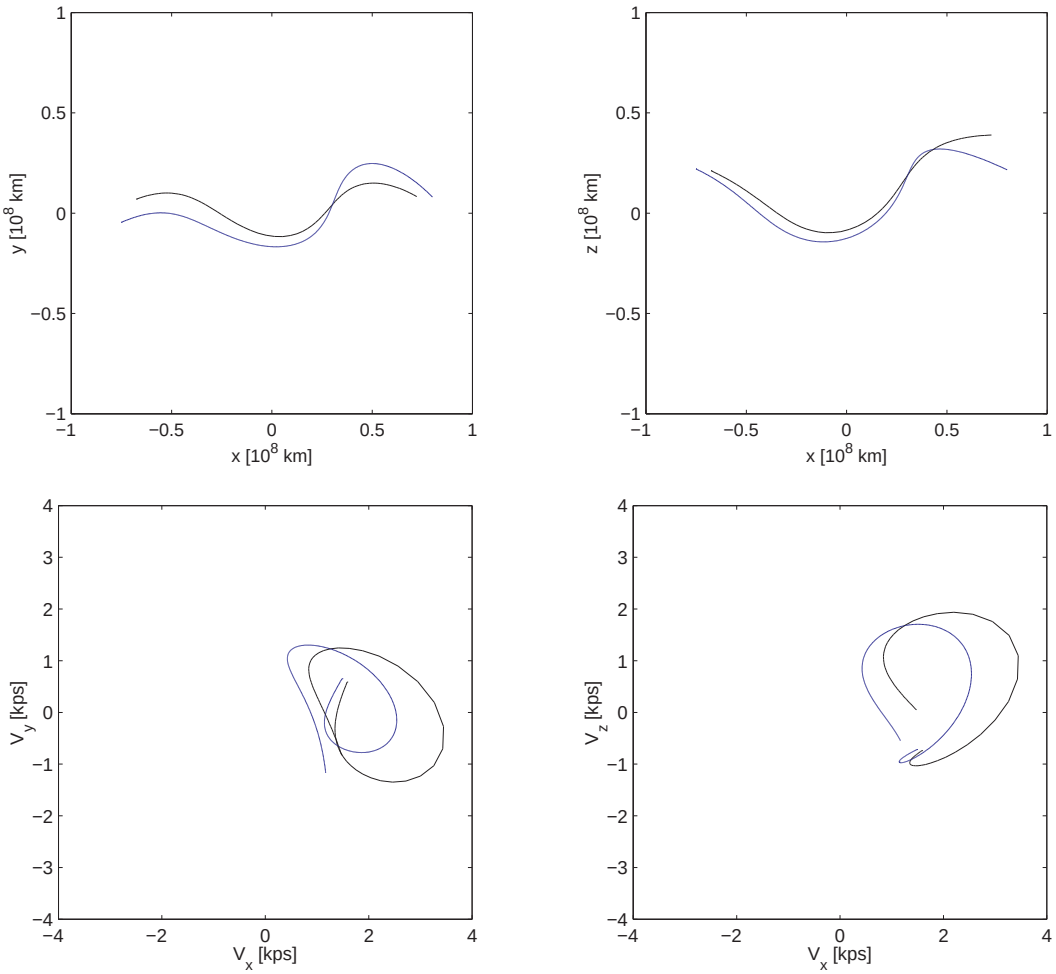

Figure 3.23. Position and Velocity Match for Oterma
in the CR3BP (1962-1964)

a match is simplified by considering possible heteroclinic connections between the stable and unstable manifolds associated with the SJL1 and SJL2 halo families [17]. The search process is similar to that implemented for OTR, except that, in this case, the near symmetry across halo families offers a significant advantage in establishing a match. A possible match is illustrated in Figure 3.25 as a combination of the stable and unstable manifolds associated with a southern SJL1 halo orbit. The trajectories corresponding to the stable and unstable manifolds originate from the same halo orbit, and hence, both arcs share the same Jacobi constant. Once again, to improve the accuracy of the match, the trajectories are transferred from the CR3BP into the

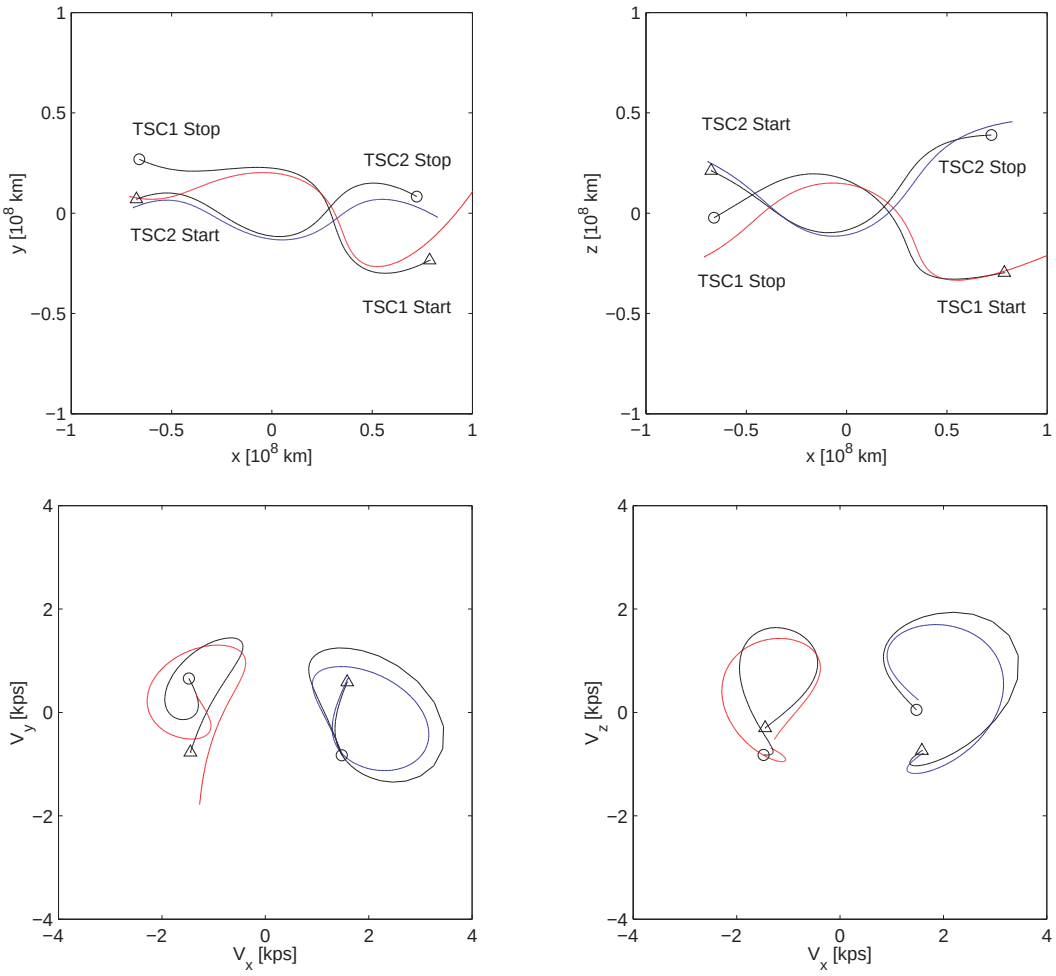

Figure 3.24. Position and Velocity Match for Oterma
in the Ephemeris Model (1935-1939 and 1962-1964)

ephemeris model. The match, as computed in the ephemeris model, is plotted in Figure 3.26. The red curve represents an arc along the stable manifold for a southern SJL1 quasi-periodic Lissajous trajectory. The unstable manifold appears as a blue curve corresponding to the same SJL1 Lissajous trajectory. The orbital path of the comet HRC is directly plotted from ephemeris data as a black curve.

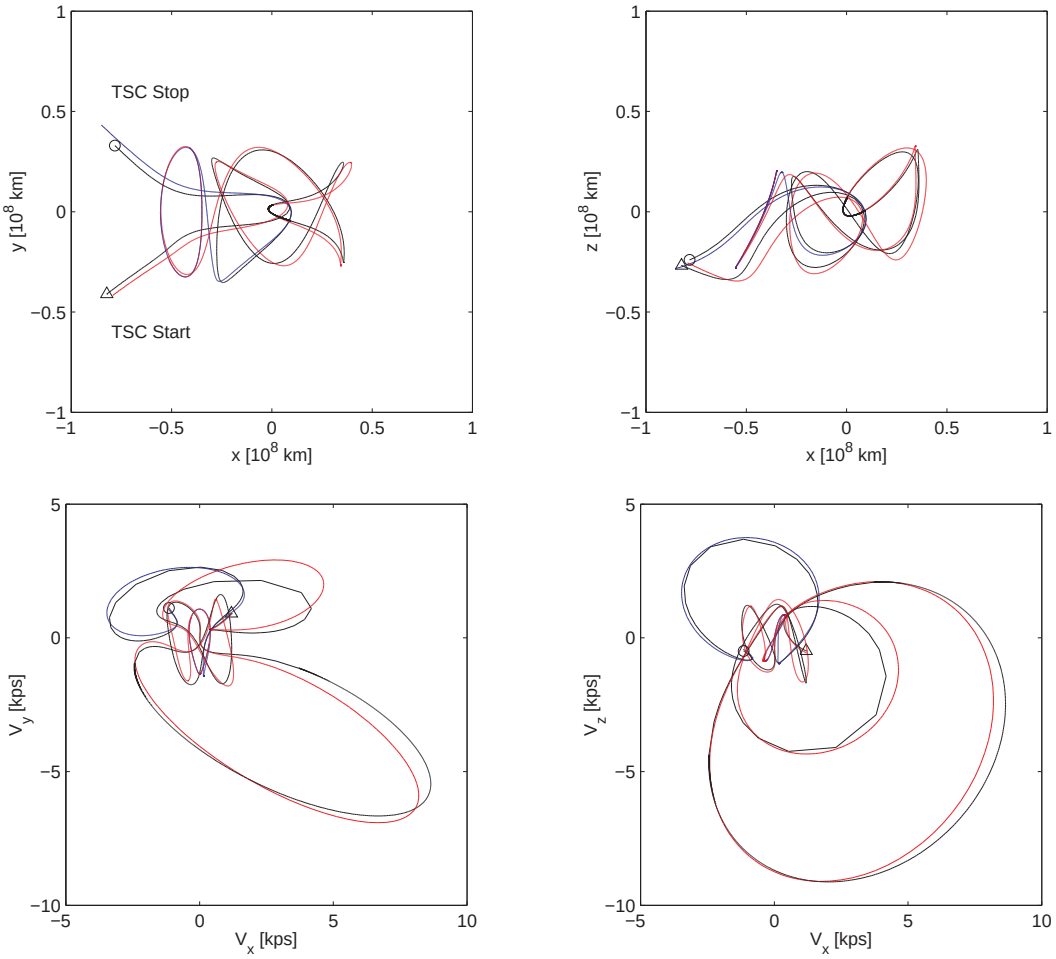

Figure 3.25. Position and Velocity Match for Helin-Roman-Crockett in the CR3BP (1966-1985)

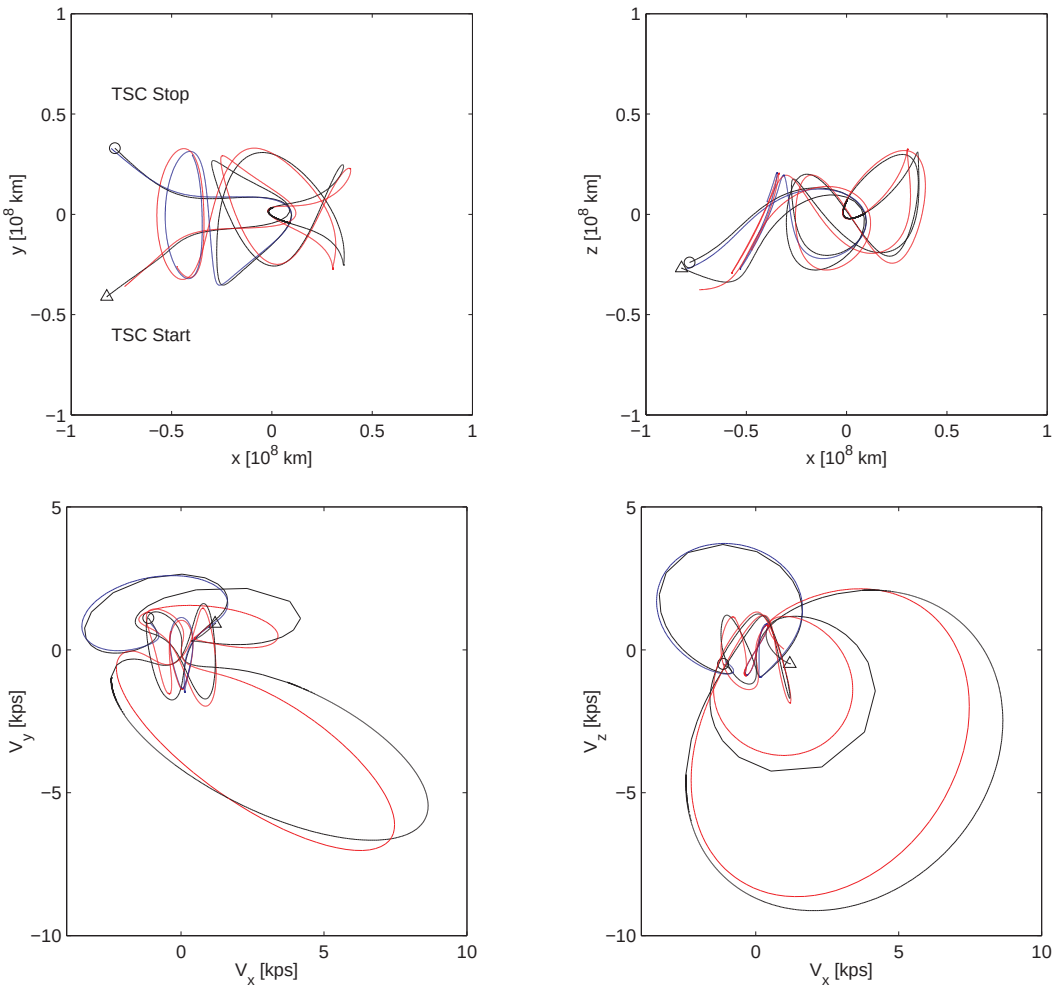

Figure 3.26. Position and Velocity Match for Helin-Roman-Crockett in the Ephemeris Model (1966-1985)

4. Conclusion

The natural symmetries in the CR3BP and the observed near-symmetries between the L1 and L2 halo families – based on numerical analysis – provide the basic understanding necessary to begin the search process and ultimately identify a match in the CR3BP, for a particular Jupiter family short-period comet. A dynamical systems perspective has provided significant insight into the geometry of solutions in the Sun-Jupiter system and offered a simple model to account for the most notable features of the TSC phenomena observed in Jupiter family short-period comets. Furthermore, the fact that the observed motion of these comets can be explained in the context of dynamical systems suggests further applications to the motion of natural bodies in the solar system. This dynamical insight also extends to potential applications in support of interplanetary mission design for spacecraft. The next step in this investigation is the application of this modeling approach to the capture of other short-period Jupiter family comets, such as Gehrels 3. Although the search strategy discussed here is successfully applied to the capture motion of HRC and OTR, a slightly different approach might be necessary in modeling other Jupiter family comets. Since the three-dimensional, chaotic nature of TSC results in distinct types of motion during capture, modeling other comets might require consideration of the stable and unstable manifold solutions associated with other types of periodic and quasi-periodic orbits in the Sun-Jupiter system, aside from the SJL1 and SJL2 halo solutions. Since the dimensions of the orbits of interest in this study lie outside the range of validity of the available analytical approximations, it might also be necessary to consider alternative approaches to generate the necessary initial guess for the trajectory if other types of reference solutions are to be considered. Furthermore, comets such as Gehrels 3,

that experience low altitude approaches to Jupiter might also require a more complex model that incorporates additional perturbing forces. Nevertheless, the modeling of the TSC phenomena has generated additional understanding of the natural dynamics in this R3BP regime.

List of References

[1] G. W. Kronk, "http:// www.comets.amsmeteors.org/ comets/ pcomets/ 039p.html," Historical Notes for 39P/Oterma, 1995.

[2] E. I. Kazimirchak-Polonskaya, "The Major Planets as Powerful Transformers of Cometary Orbits," *The Motion, Evolution, and Origin of Comets*, pp. 373–397, International Astronomical Union: Symposium No. 45, 1972.

[3] A. Carusi and F. Pozzi, "Planetary Close Encounters Between Jupiter and About 3000 Fictitious Minor Bodies," *The Moon and the Planets*, Vol. 19, 1978, pp. 71–87.

[4] A. Carusi and G. B. Valsecci, "Numerical Simulations of Close Encounters Between Jupiter and Minor Bodies," *Asteroids* (T. Gehrels, ed.), pp. 391–415, Arizona: The University of Arizona Press, 1979.

[5] A. Carusi and G. B. Valsecci, "Planetary Close Encounters: Importance of Nearly Tangent Orbits," *The Moon and the Planets*, Vol. 22, 1980, pp. 113–124.

[6] A. Carusi and G. B. Valsecci, "Temporary Satellite Capture of Comets by Jupiter," *Astronomy and Astrophysics*, Vol. 94, 1981, pp. 226–228.

[7] A. Carusi, L. Krésak, and G. B. Valsecci, "Perturbations by Jupiter of a Chain of Objects Moving in the Orbit of Comet Oterma," *Astronomy and Astrophysics*, Vol. 99, 1981, pp. 262–269.

[8] A. Carusi, E. Perozzi, and G. B. Valsecci, "Low Velocity Encounters of Minor Bodies with the Outer Planets," *Dynamical Trapping and Evolution in the Solar System*, pp. 377–395, Holland: D. Reidel Publishing, 1983.

[9] A. Carusi, L. Krésak, E. Perozzi, and G. B. Valsecci, "First Results of the Integration of Motion of Short-Period Comets Over 800 Years," *Dynamics of Comets: Their Origin and Evolution* (A. Carusi and G. B. Valsecchi, eds.), pp. 319–340, Holland: D. Reidel Publishing, 1983.

[10] A. Carusi and G. B. Valsecci, "Dynamics of Comets," *Chaos, Resonance, and Collective Dynamical Phenomena in the Solar System*, pp. 255–268, International Astronomical Union: Symposium No. 152, July 1991.

[11] G. P. Horedt, "Capture of Planetary Satellites," *The Astronomical Journal*, Vol. 81, August 1976, pp. 675–678.

[12] T. A. Heppenheimer, "On the Presumed Capture Origin of Jupiter's Outer Satellites," *Icarus*, Vol. 24, 1975, pp. 172–180.

[13] T. A. Heppenheimer and C. Porco, "New Contributions to the Problem of Capture," *Icarus*, Vol. 30, 1977, pp. 385–401.

[14] M. A. Murison, *Satellite Capture and the Restricted Three-Body Problem*. Ph.D. Dissertation, University of Wisconsin-Madison, Madison, Wisconsin, August 1988.

[15] M. A. Murison, "The Fractal Dynamics of Capture in the Circular Restricted Three-Body Problem," *The Astronomical Journal*, Vol. 98, December 1989, pp. 2346–2386.

[16] M. W. Lo and S. D. Ross, "Surfing the Solar System: Invariant Manifolds and the Dynamics of the Solar System," Jet Propulsion Laboratory, Technical Report JPLIOM 312/97,2-4, Pasadena, California, 1997.

[17] W. S. Koon, M. W. Lo, J. E. Marsden, and S. D. Ross, "Heteroclinic Connections Between Periodic Orbits and Resonance Transitions in Celestial Mechanics," *Society for Industrial and Applied Mathematics*, May 1999. Conference Paper.

[18] K. C. Howell, B. G. Marchand, and M. W. Lo, "Temporary Satellite Capture of Short-Period Jupiter Family Comets from the Perspective of Dynamical Systems," *AAS/AIAA Astrodynamics Specialists Conference*, Clearwater, Florida, January 23-26 2000. AAS Paper 00-155.

[19] J. J. O'Connor and E. F. Robertson, "http:// www-history.mcs.st-and.ac.uk/ history/ HistTopics/ Orbits.html," History Notes on Orbits and Gravitation, 1996.

[20] T. S. Parker and L. O. Chua, *Practical Numerical Algorithms for Chaotic Systems*. New York: Springer-Verlag, 1989.

[21] S. Wiggins, *Introduction to Applied Nonlinear Dynamical Systems and Chaos*. New York: Springer-Verlag, 1990.

[22] J. J. O'Connor and E. F. Robertson, "http:// www-history.mcs.st-and.ac.uk/ history/ Mathematicians/ Lagrange.html," Biography of Joseph-Louis Lagrange, 1999.

[23] R. W. Farquhar and A. A. Kamel, "Quasi-Periodic Orbits About the Translunar Libration Point," *Celestial Mechanics*, Vol. 7, 1973, pp. 458–473.

[24] D. L. Richardson, "Analytic Construction of Periodic Orbits About the Collinear Points," *Celestial Mechanics*, Vol. 22, 1980, pp. 241–253.

[25] D. L. Richardson and N. D. Cary, "A Uniformly Valid Solution for Motion About the Interior Libration Point of the Perturbed Elliptic-Restricted Problem," *AIAA/AAS Astrodynamics Specialists Conference*, Nassau, Bahamas, July 1975. AAS Paper 75-021.

[26] C. Marchal, "Study on the Analytic Representation of Halo Orbits," ESA Contractor Final Report, Contract Report No. 5647/83/D/JS(SC), Technical Report, Châtillon, France, July 1985.

[27] G. Gómez, A. Jorba, J. Masdemont, and C. Simó, "Final Report: Study Refinement of Semi-Analytical Halo Orbit Theory," ESOC Contract Report, Technical Report 8625/89/D/MD(SC), Barcelona, Spain, April 1991.

[28] M. Hénon, "Vertical Stability of Periodic Orbits in the Restricted Problem, I. Equal Masses," *Astronomy and Astrophysics*, Vol. 28, 1973, pp. 415–426.

[29] M. Michalodimitrakis, "A New Type of Connection Between the Families of Periodic Orbits of the Restricted Problem," *Astronomy and Astrophysics*, Vol. 64, 1978, pp. 83–86.

[30] S. S. Ichtiaroglou and M. Michalodimitrakis, "Three Body Problem: The Existence of Families of Three-Dimensional Periodic Orbits which Bifurcate from Planar Periodic Orbits," *Astronomy and Astrophysics*, Vol. 81, 1980, pp. 30–32.

[31] I. A. Robin and V. V. Markellos, "Numerical Determination of Three-Dimensional Periodic Orbits Generated from Vertical Self-Resonant Satellite Orbits," *Celestial Mechanics*, Vol. 21, 1980, pp. 395–434.

[32] K. C. Howell and B. T. Barden, "Fundamental Motions Near the Collinear Libration Points and their Transitions," *Journal of the Astronautical Sciences*, Vol. 46, No. 4, 1998, pp. 361–378.

[33] J. Guckenheimer and P. Holmes, *NonLinear Oscillations, Dynamical Systems, and Bifucartions of Vector Fields*. New York: Springer-Verlag, 1983.

[34] A. H. Nayfeh and D. T. Mook, *NonLinear Oscillations*. New York: John Wiley and Sons, 1995.

[35] L. Perko, *Differential Equations and Dynamical Systems*. New York: Springer-Verlag, second ed., 1996.

[36] J. K. Hale and H. Kǫcak, *Dynamics and Bifurcations*. New York: Springer-Verlag, 1991.

[37] A. H. Nayfeh and B. Balachandran, *Applied Nonlinear Dynamics*. New York: John Wiley and Sons, 1995.

[38] H. K. Khalil, *Nonlinear Systems*. New Jersey: Prentice Hall, 1996.

[39] V. A. Yakubovich and V. M. Starzhinskii, *Linear Differential Equations with Periodic Coefficients*. New York: John Wiley and Sons, 1975.

[40] A. E. Roy, *Orbital Motion*. London: Institute of Physics Publishing, third ed., 1988.

[41] R. S. Wilson, "A Design Tool for Constructing Multiple Lunar Swingby Trajectories," M.S. Thesis, Purdue University, West Lafayette, Indiana, December 1993.

[42] K. C. Howell and H. J. Pernicka, "Numerical Determination of Lissajous Trajectories in the Restricted Three-Body Problem," *Celestial Mechanics*, Vol. 41, 1988, pp. 107–124.

[43] G. Gómez and J. Masdemont, "Some Zero Cost Transfers Between Libration Point Orbits," *AAS/AIAA Spaceflight Mechanics Meeting*, Clearwater, Florida, January 23-26 2000. AAS Paper 00-177.